TU Delft

Delft University of Technology

Electrochemical CO2 Reduction to Multicarbon Products on MoS2 Catalysts

Engineering sulfur-vacant MoS2 and Co-Catalyst Interfaces for Selective Electrochemical CO2 Reduction to Multicarbon Products

Mádai, E.

Publication date
2026

Document Version
Final published version

Citation (APA)
Mádai, E. (2026). *Electrochemical CO2 Reduction to Multicarbon Products on MoS2 Catalysts: Engineering sulfur-vacant MoS2 and Co-Catalyst Interfaces for Selective Electrochemical CO2 Reduction to Multicarbon Products*. [Dissertation (TU Delft), Delft University of Technology].

Important note
To cite this publication, please use the final published version (if applicable).
Please check the document version above.

Copyright
Other than for strictly personal use, it is not permitted to download, forward or distribute the text or part of it, without the consent of the author(s) and/or copyright holder(s), unless the work is under an open content license such as Creative Commons.

Takedown policy
Please contact us and provide details if you believe this document breaches copyrights.
We will remove access to the work immediately and investigate your claim.

This work is downloaded from Delft University of Technology.
For technical reasons the number of authors shown on this cover page is limited to a maximum of 10.

Electrochemical CO_2 reduction to multicarbon products on MoS_2 catalysts

Eszter Mádai

Electrochemical CO_2 reduction to multicarbon products on MoS_2 catalysts

Engineering sulfur-vacant MoS_2 and Co-Catalyst Interfaces for Selective Electrochemical CO_2 Reduction to Multicarbon Products

Electrochemical CO_2 reduction to multicarbon products on MoS_2 catalysts

Engineering sulfur-vacant MoS_2 and Co-Catalyst Interfaces for Selective Electrochemical CO_2 Reduction to Multicarbon Products

Dissertation

for the purpose of obtaining the degree of doctor
at Delft University of Technology
by the authority of the Rector Magnificus, Prof. dr. ir. H. Bijl,
chair of the Board for Doctorates
to be defended publicly on
Wednesday 21, January 2026 at 10:00 o'clock

by

Eszter MÁDAI

Master of Science in Materials Science
Technical University of Darmstadt, Germany
born in Miskolc, Hungary

This dissertation has been approved by the promotors.

Composition of the doctoral committee:

Rector Magnificus,	chairperson
Dr. ir. R.M. Hartkamp,	Delft University of Technology, *promotor*
Prof. dr. ir. J.M.C. Mol,	Delft University of Technology, *promotor*
Dr. P. Taheri,	Delft University of Technology, *copromotor*
Independent members:	
Prof. dr. ir. A. Urakawa	Delft University of Technology
Dr. ir. A.J. Houtepen	Delft University of Technology
Prof. dr. D. Boda	University of Pannonia, Hungary
Prof. dr. ir. B.J. Kooi	University of Groningen
Dr. R. Kortlever,	Delft University of Technology, reserve member

Keywords: Molybdenum disulfide, Electrochemical CO_2 reduction, Intercalation, Sulfur vacancy, Selectivity, Ionic liquid co-catalysts

Printed by: Ridderprint | ridderprint.nl

Cover by: Eszter Mádai

Copyright © 2025 by E. Mádai

ISBN 978-94-6522-991-1

An electronic copy of this dissertation is available at https://repository.tudelft.nl/.

To the ghost of the XPS room.

Contents

Summary ix

Samenvatting xi

1. Introduction 1
   1.1. Global warming . . . 1
   1.2. Electrochemical CO_2 reduction . . . 3

2. Literature review on CO_2 reduction with MoS_2 9
   2.1. Catalysts for CO_2 reduction . . . 10
   2.2. Structural and Electronic properties of TMDCs . . . 12
   2.3. MoS_2 forcefields in Molecular Dynamics simulations . . . 17
   2.4. Catalytic properties of TMDCs . . . 23

3. Intercalation of alkali metal ions in MoS_2 37
   3.1. Introduction . . . 38
   3.2. Methods and Materials . . . 40
      3.2.1. Molecular dynamics simulations . . . 40
      3.2.2. Electrode preparation . . . 40
      3.2.3. Electrochemical techniques . . . 41
      3.2.4. Scanning Electron Microscopy . . . 41
      3.2.5. XRD . . . 41
      3.2.6. Raman Spectroscopy . . . 41
      3.2.7. X-ray Photoelectron Spectroscopy . . . 42
   3.3. Results and discussions . . . 42
      3.3.1. Electrochemical intercalation . . . 42
      3.3.2. MD Simulations . . . 43
      3.3.3. Structure analysis . . . 45
      3.3.4. XPS analysis . . . 47
      3.3.5. Electrochemical CO_2 reduction . . . 50
   3.4. Conclusions . . . 51

4. CO_2 reduction with sulfur-vacant MoS_2 63
   4.1. Introduction & Background . . . 64
   4.2. Results & Discussion . . . 66
   4.3. Conclusions . . . 71

5. Anion effect on CO_2 reduction selectivity 77
   5.1. Introduction . . . 78

5.2. Methods and Materials 80
5.2.1. Experimental 80
5.2.2. Computational details 82
5.3. Results and discussion 83
5.3.1. CO_2 with different imidazolium acetates 83
5.3.2. DFT Analysis 86
5.3.3. Surface analysis of exposed electrodes 89
5.4. Conclusions 92

6. Conclusion and recommendations 99

A. Appendix to Chapter 3 103

B. Appendix to Chapter 4 123

C. Appendix to Chapter 5 129

Acknowledgements 137

Curriculum Vitæ 141

List of Publications 143

Summary

Electrochemical CO_2 (CO_2RR) reduction reaction presents a potential path to create the carbon cycle and achieve a net 0 carbon emission. To this, however, novel catalysts have to be investigated to find the balance between production efficiency, feasibility, earth-abundancy and cost-efficiency. Molybdenum disulfide (MoS_2) is a potential candidate for this role, however, its production efficiency for the CO_2RR has to be investigated deeper and optimized further in the sense of engineering its environment through the presence of co-catalysts and tuning its structural and electronic properties through induced vacancies and intercalants. Hence, this thesis explores strategies for utilizing MoS2 as a catalyst for the electrochemical CO2 reduction reaction, focusing on enhancing its conductivity through alkali ion intercalation and tuning its selectivity via the introduction of various co-catalysts.

The thesis is structured in the following way, **Chapter 1** gives a brief introduction to the electrochemical CO_2RR and its potential challenges. Then, **Chapter 2** presents a literature review on the nature of MoS_2, the literature about the electrochemical CO_2RR with MoS_2 as a catalyst, its unique catalytic properties and possible challenges for the CO_2RR. The chapter also presents a background for the intercalation of alkali metal ions in MoS_2 and the consequently induced phase transition. Furthermore, as molecular dynamics (MD) simulations are also used and presented in the thesis, the possible force fields and challenges relating to MD simulations are also described in the chapter.

In **Chapter 3**, a study about the tunability of the electronic properties of MoS_2 is presented and their effect on the electrochemical CO_2RR. Here, we present a comprehensive investigation into the atomic-scale intercalation mechanism using MD simulations, complemented by experimental analysis of structural and electronic properties at the macro scale through various characterization techniques. It is demonstrated that the hydration shell of ions serves as an energy barrier to intercalation as it undergoes a structural change during the intercalation. When alkali metal ions are intercalated into MoS_2, they introduce more defects and enhance electronic conductivity. Notably, these effects are more pronounced for potassium than for sodium. Furthermore, it is shown that the improved conductivity through the alkali metal ion intercalation has an unfavorable effect on the efficiency of the CO_2RR.

Chapter 4 investigates the role of sulfur vacancies, identified in Chapter 3, in the MoS_2 structure and their effect on the product distribution of the elec-

trochemical CO_2RR in the presence of different co-catalysts. It is shown that due to the presence of sulfur vacancies, the product distribution is shifted from C_1 products to higher hydrocarbons. Furthermore, the effect of the used co-catalyst on the product distribution is studied, as while using [EMIM]-[BF_4] as co-catalyst results in a wide range of hydrocarbon products, using [EMIM][Otf] as co-catalyst renders the catalyst inactive towards the CO_2RR.

Building on the results of Chapter 4, tuning the selectivity of the electrochemical CO_2RR on sulfur-vacant MoS_2 is presented in **Chapter 5**. Here, two imidazolium-based ionic liquids, [EMIM][OAc] and [EMIM][TFA], are used as co-catalysts and it is shown that while the cation of the co-catalyst plays an important role in the transport of the CO_2 molecule to the catalyst surface, the anion of the co-catalyst plays a similarly important role during the chain building in the CO_2RR. Hence, the selectivity of the CO_2RR in the case of the two co-catalysts differs significantly: with the [EMIM][OAc] as co-catalyst a wide range of hydrocarbon products are measured, however, with the [EMIM][TFA] as co-catalyst, the CO_2RR is highly selective towards one product.

Samenvatting

Elektrochemische CO_2-reductie (CO_2RR) biedt een mogelijke route om de koolstofkringloop te sluiten en netto 0-uitstoot te bereiken. Hiervoor moeten echter nieuwe katalysatoren worden onderzocht om een balans te vinden tussen opbrengstefficiëntie, uitvoerbaarheid, natuurlijke beschikbaarheid en kostenefficiëntie.

Molybdeendisulfide (MoS_2) is een potentiële kandidaat hiervoor, maar de opbrengstefficiëntie bij de CO_2RR moet verder worden onderzocht en geoptimaliseerd door de lokale omstandigheden te beïnvloeden met co- katalysatoren en door structurele en elektronische eigenschappen te tunen via geïnduceerde defecten en intercalanten.

Deze thesis onderzoekt daarom de potentie van MoS_2 als katalysator voor de CO_2RR, zowel door de geleidbaarheid ervan te beïnvloeden via intercalatie van verschillende alkalimetalen, als door de selectiviteit van de CO_2RR te sturen met verschillende co-katalysatoren.

De thesis is als volgt opgebouwd: **Hoofdstuk 1** geeft een beknopte introductie in de elektrochemische CO_2RR en de bijbehorende uitdagingen. Daarna presenteert **Hoofdstuk 2** een literatuuroverzicht over de aard van MoS_2, onderzoek naar de elektrochemische CO_2RR met MoS_2 als katalysator, de unieke katalytische eigenschappen en mogelijke knelpunten. Bovendien presenteert het hoofdstuk de achtergrond voor de intercalatie van alkalimetalen in MoS_2 en de daaruit voortvloeiende faseovergang. Aangezien moleculaire dynamica (MD)-simulaties ook worden toegepast, worden de uitdagingen van MD-simulaties eveneens beschreven.

In **Hoofdstuk 3** wordt de beïnvloedbaarheid van de elektronische eigenschappen van MoS_2 bestudeerd en hun effect op de elektrochemische CO_2RR. We presenteren een grondig onderzoek naar het atomistische intercalatiemechanisme met MD-simulaties, aangevuld met experimentele analyse van structurele en elektronische eigenschappen op macroschaal via diverse karakterisatietechnieken. Er wordt aangetoond dat de hydratatie-schil van ionen als energiedrempel fungeert tijdens intercalatie, doordat deze van structuur verandert. Wanneer alkalimetalen in MoS_2 worden geïntercaleerd, ontstaan er meer defecten en neemt de elektrische geleidbaarheid toe. Opvallend is dat deze effecten sterker zijn voor kalium dan voor natrium. Verder wordt aangetoond dat de verbeterde geleidbaarheid door alkalimetalen een nadelig effect heeft op de efficiëntie van de CO_2RR.

Hoofdstuk 4 behandelt de onderzoeksvraag naar zwavelvacaturen in de MoS_2-structuur (geïdentificeerd in Hoofdstuk 3) en hun effect op de productverdeling van de elektrochemische CO_2RR in aanwezigheid van ver-

schillende co-katalysatoren. Het blijkt dat door zwavelvacaturen de productverdeling verschuift van C_1-producten naar hogere koolwaterstoffen. Daarnaast wordt het effect van de co-katalysator op de productverdeling onderzocht: met [EMIM][BF_4] ontstaat een breed spectrum aan koolwaterstoffen, terwijl [EIMI][Otf] de katalysator inert maakt voor de CO_2RR.

Voortbouwend op de resultaten van Hoofdstuk 4, wordt in **Hoofdstuk 5** de selectiviteit van de elektrochemische CO_2RR op zwavelvacant MoS_2 getuned. Hierbij zijn twee imidazolium-gebaseerde ionische vloeistoffen, [EMIM]-[OAc] en [EMIM][TFA], als co-katalysatoren gebruikt. Er wordt aangetoond dat zowel de kation als de anion van de co-katalysator een cruciale rol spelen: de kation beïnvloedt het transport van CO_2 naar het katalysatoroppervlak, terwijl de anion belangrijk is voor de ketenopbouw tijdens de CO_2RR. Hierdoor verschillen de selectiviteiten sterk: met [EMIM][OAc] wordt een breed scala aan koolwaterstoffen geproduceerd, terwijl [EMIM][TFA] leidt tot hoge selectiviteit voor één product.

Vain effort! As an individual.
You will accomplish naught against the age:
'Tis a stream, which bears along, or sinks:
Wherein each one must swim, and none control.
Those whom the chronicler calls great, are those
Who comprehend their time, but give not birth
To new ideas.
For never comes the dawn at crowing of the cock.
But when the dawn approaches, then the cock doth crow.

The Tragedy of Man - Imre Madách

1

Introduction

1.1. Global warming

Until the mid-eighteenth century the global CO_2 emission was kept on a constant level. However, through the invention of the steam engine the First Industrial Revolution (1760-1840) began in Great Britain and then spread across Europe and the United States. Hand-production was overtaken by machines and new iron manufacturing processes were invented, which lead to heavy urbanization and sharply increasing levels of smoke pollution [1]. The newly established factories increased the coal consumption and industrial centers quickly became also the centers of air pollution. Due to this increased level of air pollution the until then constant CO_2 levels also started rising. Figure 1.1 (a) and (b) show the atmospheric CO_2 concentration of the last 350 years.

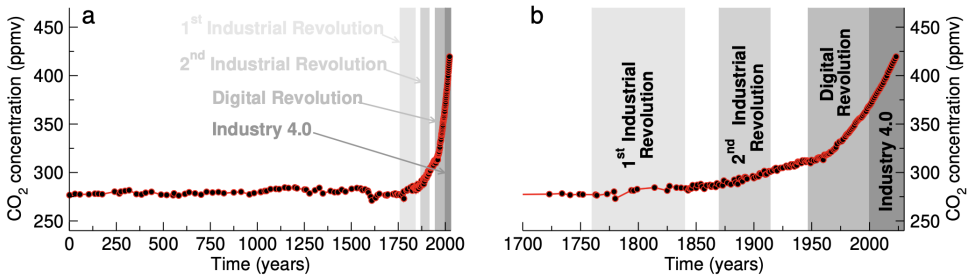

Figure 1.1. **(a)** & **(b)** Atmospheric CO_2 concentration in the last 350 years. The four major industrial revolutions highlighted in the background. Data adapted from [2].

During the Second Industrial Revolution (1870-1914), which brought rapid scientific discoveries, industrialization, mass production and electrification to the world, the atmospheric CO_2 concentration increased above 300

1

ppmv and kept increasing further in a steady slope. However, this slope was changed to a steeper one once the transistor and its mass production was discovered during the Digital Revolution (1947-present), where the economy started centering around information technology. With the development of artificial intelligence (AI) and gene editing we arrived to our present which many call as Industry 4.0 [3] and currently we are at an atmospheric CO_2 concentration of 419 ppmv.

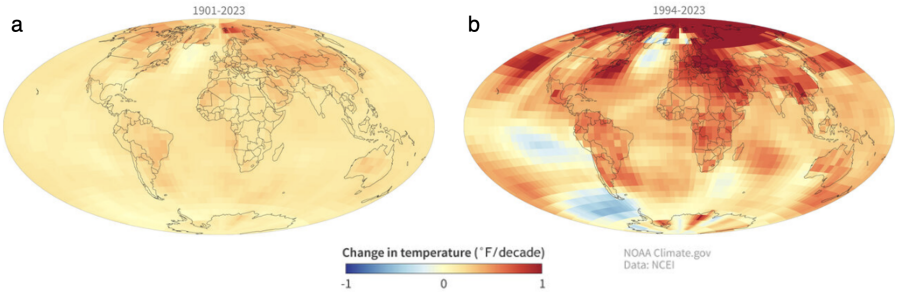

Figure 1.2. World maps for comparison in trends of surface temperature between the 20th century **(a)** and the last few decades **(b)**. Image adapted from [4].

As a consequence of the emission of greenhouse gases, the average temperature of the Earth has started rising since after the First Industrial Revolution by 0.06 °C per decade [4]. Figure 1.2 (a) and (b) show the Earth's surface temperature in the last century and the last three decades. By comparing the two maps, the trends show that the rate of warming in the last few decades is much faster than what the long-term average would show. The worst region based on the maps is the Arctic, where the rate of warming is amplified due to the loss of reflective snow and ice. Based on the data collected by the National Centers for Environmental Information, the year 2023 was the warmest recorded year: it was 1.18 °C warmer than the average temperature of the 20 th century and it was also 1.35 °C warmer than the pre-industrial temperature average [5]. The global emission of CO_2 by 2022 reached the amount of 37.15 Gt [6] and as fossil fuels are still the main source of energy and the global energy consumption is expected to double by 2050 [7]. This also leads to a sharp increase in the emission of CO_2 and other greenhouse gases. According to calculations, the cumulative CO_2 emission can reach the 500 Gt in average by 2060[8].

Hence, to prevent further damaging of our environment and to restate the emitted amount of CO_2 for the levels of at least 1990, among the reduced and conscious emission, the development of new routes for CO_2 utilization is needed. Carbon dioxide mitigation strategies

generally fall into two categories: capture and conversion. CO_2 capture can be achieved from both point sources (e.g., industrial exhaust) and ambient air using techniques such as amine scrubbing, pressure swing adsorption, or absorption into ionic liquids and solid sorbents [9, 10]. These methods enable selective separation of CO_2 from mixed gas streams but require further action to manage or utilize the captured gas. In terms of conversion, thermochemical and photochemical routes have been explored to transform CO_2 into value-added products such as methanol, methane, or syngas, often requiring high temperatures or specialized reactor configurations [11, 12]. Among these, electrochemical CO_2 reduction (CO_2RR) is especially attractive, as it allows for direct transformation of CO_2 into fuels and chemicals under ambient conditions using renewable electricity. This technology, when paired with effective catalyst design and green energy input, offers a promising route toward carbon-neutral fuel cycles.

1.2. Electrochemical CO_2 reduction

With a proper selection of electrocatalysts or photocatalysts and using green energy, CO_2 can be reduced to ethanol or other organic compounds that can be directly used as fuels or fuel additives. Carbon-monoxide (CO) - another prominent product of electrochemical CO_2 reduction - mixed with hydrogen (H_2) (resulting syngas) used in the Fischer-Tropsch synthesis to produce liquid hydrocarbons [13]. Thus, by replacing fossil fuels and petrol-based additives with recycled ones, the carbon-neutral cycle can be achieved as a potential and promising route for CO_2 recycling. As mentioned earlier, in the carbon-neutral cycle the emitted CO_2 is captured and converted into green fuels or fuel additives by using green energy, hence net emission is indeed reduced to zero for the entire process. Furthermore, this cycle is not only useful from a CO_2-reduction point of view, but also from a green energy-conversion point of view: the energy produced in excess by natural sources can be used or stored in the conversion of green fuels.

Figure 1.3 shows the schematics of a three-electrode electrochemical cell. The anode compartment is separated from the cathode compartment by an anion exchange membrane. During the CO_2 conversion, there are three main reactions occurring in the electrochemical cell: CO_2 reduction reaction (CO_2RR) and the competing hydrogen evolution reaction (HER) in the cathode compartment, and oxygen evolution reaction (OER) on the anode. As HER is a constantly present and competing reaction to CO_2RR, either the catalyst has to be selective towards the latter one or the environment of the electrode has to be engineered in a way to promote it and suppress the HER. Furthermore, even if the HER is as low as possible, the CO_2RR can have multiple products. Based on the interactions between the CO_2 molecule on the

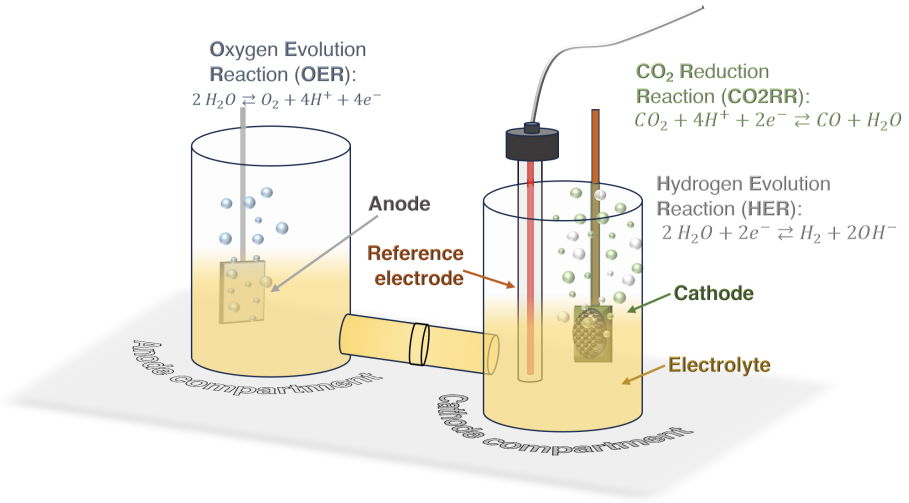

Figure 1.3. Schematics of a three-electrode electrochemical cell with separated anode and cathode compartments. The three main reactions taking place during the electrochemical CO_2 reduction are shown close to their respective compartments.

catalyst surface (which atoms it binds to on the surface, the strength of the binding, the conformation of the molecule, the local pH at the catalyst surface) the reaction pathway differs and results in different products (e.g. carbon-monoxide, formate, methanol, ethanol, other C_2- or C_3 products). Also, relating to the selectivity, catalyst poisoning can be caused by volatile species in the cell or can originate from the formed product itself, if it cannot desorb from the surface of the catalyst. If the catalyst is selective and the surface is engineered as such that the poisoning is avoidable, the durability of the catalyst is also an important parameter. The development of cost-efficient catalysts with a long lifetime is crucial from engineering and economic point of view.

Choosing the right catalyst for the electrochemical conversion of CO_2 is a challenge in itself. Researchers nowadays study many different potential catalyst materials for CO_2RR. The most common and widely studied material is copper, as it can convert CO_2 into over 15 different products, including ethylene, which is a very rare product of CO_2RR. Other than copper, silver and gold are also studied extensively, however, the cost-efficiency of using noble metals as catalysts is questionable. Furthermore, using these catalyst materials also raises the question of efficiency regarding their dimensions, as their volume compared to the exposed surface is large. Thus, for these materials, the surface/bulk ratio

is small, which means that the active surface area that can be efficiently used for catalysis is relatively small compared to the volume of the catalyst.

Catalyst Design: from Conventional Metals to Two-Dimensional Platforms

In conventional heterogeneous catalysis, bulk transition-metal electrodes (e.g., Cu, Ag, Au) offer well-defined active sites but suffer from a low surface-to-volume ratio and rigid electronic structures that limit activity and selectivity in the CO_2 reduction reaction (CO_2RR) [14]. Reducing the catalyst dimensions—from bulk to nanostructured and ultimately to atomically thin layers—dramatically increases the fraction of surface atoms and unlocks new ways to tailor the electronic landscape.

Graphene and nitrogen/metal-doped graphene.
Pristine graphene is a zero-band-gap semimetal and therefore catalytically inert toward CO_2RR. Introducing heteroatoms (N, B) or isolated metal centers into the lattice opens a tunable band gap and creates well-defined adsorption sites for key intermediates [15, 16]. The gap width and catalytic behavior correlate with dopant type, concentration, and local configuration, enabling rational optimisation.

Two-dimensional metal–organic frameworks (2D-MOFs).
Single-layer MOFs combine an extended π-conjugated backbone with periodically spaced metal nodes. By judiciously selecting the organic linker and the metal centre, researchers can modulate both the band gap and the binding strength for CO_2-derived intermediates, achieving high Faradaic efficiencies for formate and CO [17].

Transition-metal dichalcogenides (TMDCs).
Layered TMDCs such as MoS_2 bridge the gap between metallic catalysts and molecularly defined active sites. Bulk 2H-MoS_2 possesses an indirect band gap (1.2 eV), which hampers photogenerated charge separation; exfoliation to a monolayer converts it to a direct gap (1.8 eV) and enhances carrier mobility [18]. Beyond thickness control, the electronic structure can be tuned (i) *in-plane* by heteroatom substitution or vacancy engineering and (ii) *out-of-plane* by intercalating alkali or organic ions between S–Mo–S layers, thereby modifying orbital alignment and catalytic pathways [19, 20].

In summary, two-dimensional catalysts combine a maximised active surface with band-gap tunability unavailable in their three-dimensional counterparts. Among these, defect- and intercalation-engineered MoS_2 stands out as a versatile model system for fundamental and applied CO_2RR studies.

As intercalation provides a possibility to engineer the properties of the TMDCs, a part of this thesis is set to explore the intercalation mechanisms of light and heavy alkali metal ions in MoS_2 and its effect on the product

distribution of the CO_2RR and on the structural and electronic properties of MoS_2, such as defect formation, phase transition and conductivity increase/decrease. The intercalation of different alkali metal ions in MoS_2 was studied by researchers previously, however, a comparison on the effect of light and heavy alkali metal intercalation on the MoS_2 structure, the electronic properties and the CO_2RR efficiency is still lacking. This comparison is crucially needed, as the light and heavy alkali metal ions possess different electronic structures, hence, the effect of their intercalation on the electronic properties of MoS_2 should also be different. However, tuning the electronic properties of the catalyst is only one path to promote the CO_2RR on MoS_2, engineering the catalyst environment also affects the product distribution. Therefore, other parts of the thesis are aiming to explore the effect of the co-catalyst on the product distribution and selectivity of the CO_2RR, specifically, the synergistic or counteractive role of anions of different ionic liquids.

references

[1] B. Clapp. *An Environmental History of Britain since the Industrial Revolution*. Taylor & Francis, 2014. ISBN: 9781317893035. URL: https://books.google.nl/books?id=29QFBAAAQBAJ.

[2] P. R. Hannah Ritchie and U. S. E. P. A. Veronika Samborska (2024) - "Climate Change". Data adapted from NOAA Global Monitoring Laboratory. *Carbon dioxide concentrations in the atmosphere*. https://ourworldindata.org/grapher/co2-long-term-concentration?time=1307..latest. 2024.

[3] W. W. Henning Kagermann Wolf-Dieter Lukas. *Industry 4.0: On the way to the 4th industrial revolution with the Internet of Things*. https://www.ingenieur.de/technik/fachbereiche/produktion/industrie-40-mit-internet-dinge-weg-4-industriellen-revolution/. 2011.

[4] R. Lindsey and L. Dahlman. *Climate Change: Global Temperature*. https://www.climate.gov/news-features/understanding-climate/climate-change-global-temperature. 2024.

[5] N. N. C. for Environmental Information. *Monthly Global Climate Report for Annual 2023, published online January 2024, retrieved on July 8, 2024*. https://www.ncei.noaa.gov/access/monitoring/monthly-report/global/202313. 2024.

[6] H. Ritchie and M. Roser. "CO2 emissions". In: *Our World in Data* (2020). https://ourworldindata.org/co2-emissions.

[7] D. McCollum, N. Bauer, K. Calvin, A. Kitous, and K. Riahi. "Fossil resource and energy security dynamics in conventional and carbon-constrained worlds". In: *Climatic Change* 123.3-4 (2013), pp. 413–426. DOI: 10.1007/s10584-013-0939-5. URL: https://doi.org/10.1007%2Fs10584-013-0939-5.

[8] S. J. Davis, K. Caldeira, and H. D. Matthews. "Future CO_2 Emissions and Climate Change from Existing Energy Infrastructure". In: *Science* 329.5997 (2010), pp. 1330–1333. DOI: 10.1126/science.1188566. URL: https://doi.org/10.1126%2Fscience.1188566.

[9] M. Boot-Handford and et al. "Carbon capture and storage update". In: *Energy & Environmental Science* 13 (2020), pp. 4071–4096. DOI: 10.1039/D0EE01257E.

[10] W. Wang, S. Wang, X. Ma, and J. Gong. "Recent advances in catalytically active solid sorbents for CO_2 capture and conversion". In: *Advanced Materials* 32.18 (2020), p. 1905214. DOI: 10.1002/adma.201905214.

[11] M. Aresta, A. Dibenedetto, and A. Angelini. "Catalysis for the valorization of exhaust carbon: from CO_2 to chemicals, materials, and fuels. Technological use of CO_2". In: *Chemical Reviews* 114 (2013), pp. 1709–1742. DOI: 10.1021/cr4002758.

[12] X. Li, L. Li, H. Wang, and X. Sun. "Conversion of CO_2 to fuels and chemicals by electro-, photo-, and photoelectrocatalysis". In: *Chemical Society Reviews* 50 (2021), pp. 1215–1245. DOI: 10.1039/D0CS00821A.

[13] G. Henrici-Olivé and S. Olivé. "Fischer-Tropsch Synthesis". In: *The Chemistry of the Catalyzed Hydrogenation of Carbon Monoxide*. Springer Berlin Heidelberg, 1984, pp. 143–196. DOI: 10.1007/978-3-642-69662-6_9. URL: https://doi.org/10.1007%2F978-3-642-69662-6_9.

[14] Y. Hori. "Electrochemical CO reduction on metal electrodes". In: *Chem. Soc. Rev.* 37 (2008), pp. 109–117.

[15] S. Guo, J. Qiu, and S. Zhang. "Nitrogen-doped graphene for CO electroreduction: mechanistic insights and catalytic design". In: *Energy Environ. Sci.* 12 (2019), pp. 684–700.

[16] Y. Lin and et al. "Single-atom Fe sites in graphene achieve selective CO electroreduction to CO". In: *Nat. Catal.* 5 (2022), pp. 1015–1023.

[17] N. Zhang and et al. "Two-dimensional metal–organic frameworks for electrochemical CO reduction". In: *Chem. Soc. Rev.* 49 (2020), pp. 875–910.

[18] M. Amani, P. Taheri, R. Addou, G. H. Ahn, D. Kiriya, D.-H. Lien, J. W. Ager, R. M. Wallace, and A. Javey. "Recombination Kinetics and Effects of Superacid Treatment in Sulfur- and Selenium-Based Transition Metal Dichalcogenides". In: *Nano Letters* 16.4 (2016), pp. 2786–2791. DOI: 10.1021/acs.nanolett.6b00536. URL: https://doi.org/10.1021%2Facs.nanolett.6b00536.

[19] D. Voiry and et al. "Phase engineering of transition metal dichalcogenides". In: *Chem. Soc. Rev.* 44 (2015), pp. 2702–2712.

[20] M. Chhowalla, H. S. Shin, G. Eda, H. Zhang, Z. Liu, and L. Zhang. "The chemistry of two-dimensional layered transition metal dichalcogenide nanosheets". In: *Nat. Chem.* 5 (2013), pp. 263–275.

2

Review of state-of-the-art literature on CO_2 reduction with MoS_2 as a catalyst

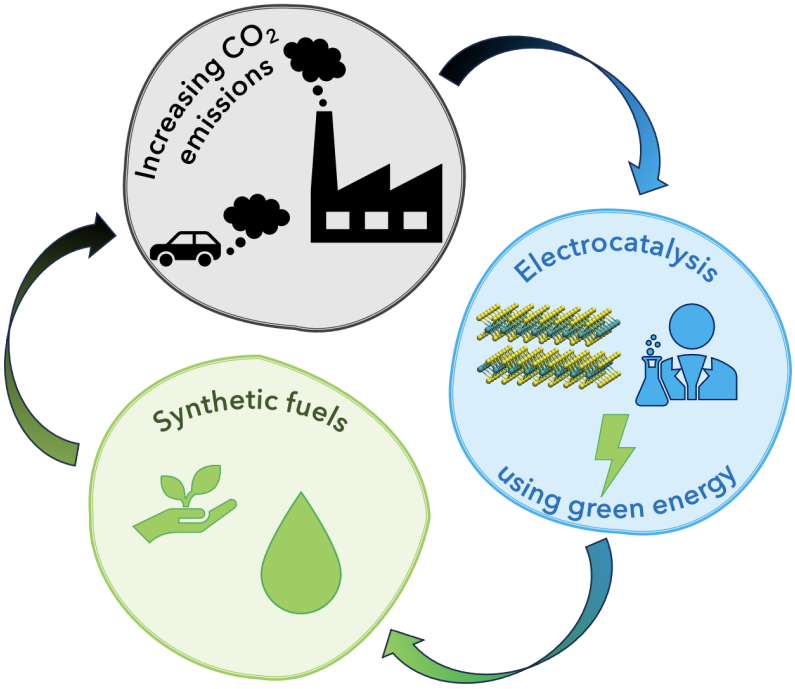

2.1. Catalysts for CO_2 reduction

As defossilization is becoming a more and more pressing matter, the reduction of CO_2 is also more and more widely researched. Many different potential catalysts are tried at the same time, such as different bulk metals (gold, copper, silver, platinum, etc.) and their nanoparticle forms, carbonaceous materials (doped graphene, MOFs) and Transition Metal Dichalcogenides (TMDCs, MoS_2, WS_2, $MoSe_2$, WSe_2).

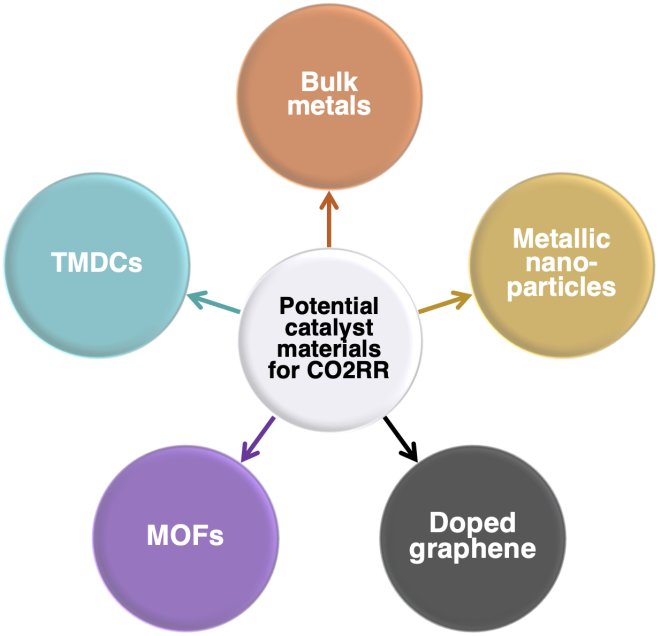

Figure 2.1. The five main different catalyst materials for CO_2RR.

Using metals, specifically copper, for electrochemical conversion of CO_2 was investigated already in the 1980s and continued in the 1990s by Hori and co-workers [1–3]. Other precious metals, such as gold, silver and platinum are also suitable catalysts for CO_2RR with various products, however cost efficiency and selectivity raise a question in their case. Still, copper is the most popular candidate for CO_2RR in the case of metals, as it is capable for the catalysis of multi-electron products with high energy (e.g. methane, ethanol) at reasonably low overpotentials.

The product distribution of CO_2RR on copper is highly affected by the orientation of the crystal. Hori and co-workers studied CO_2RR on copper single crystals at different crystal orientations ((100), (110) and (111)) [4]. The two main products of CO_2RR in the case of copper, methane and ethylene, are formed in different product ratios at different crystal

orientations. For (100) ethylene is dominant, which is a very rare and desirable product, while for the orientation (110), methane is formed in a more significant amount. The highest product ratio favoring ethylene belongs to (111), however, also the highest current efficiency for HER was observed for this crystal orientation. Furthermore, the probability of CO formation is the highest in the case of (111), as this crystal orientation has the lowest density of dangling bonds, thus, the surface of the crystal is relatively stable [5]. This enables the intermediate CO to desorp from the surface of the catalyst.

Even though the product distribution can be engineered with the crystal orientation of copper, the one of the challenges for Cu-based catalysts for CO_2RR is still the formation of products with more than 2 carbon atoms ($>C_2$ products, multicarbons). This challenge is usually resolved with the application of bimetallic catalysts, Kim and co-workers used Cu-Au bimetallic nanoparticles to engineer the production of multicarbons [6].

Since the discovery of graphene, 2D materials attracted more and more attention for general applications, and as mentioned above, the large surface-to-bulk ratio makes them especially attractive for catalysis applications. Graphene itself is the leading 2D material, due to its superior electronic, thermal and mechanical properties [7]. Graphene can be synthesized with chemical vapour deposition (CVD) and also can be produced through the reduction of graphene oxide (GO) [8]. For CO_2RR, nitrogen doping of the graphene sheets is essential to create active reduction centres [9] and with additional metal doping the Faradaic efficiency (FE) of CO_2RR to CO can be further increased, such metals can be Ni, Fe, Mn, Cu or Co [10–12]. Wu and co-workers focused on the functionality effects of the N-dopant [9] and they discovered that the FE of CO_2RR into CO increases if the N-dopant is in a pyridinic bond, rather than in a pyrrolic or graphitic bond. By doping graphene further with different metals, the bandgap and these active centers can be changed. According to Ju and co-workers, the best co-dopants with nitrogen are nickel and iron, as the FE of CO production is increased up to 90%, while if the co-dopant is cobalt or copper, the FE of CO reaches only 10% and the FE of HER is around 90% [11].

Metal-organic frameworks (MOFs) also hold a lot of potential in CO_2RR, as the metal centers can be easily varied and through that, the their band gap can be tuned. MOFs can be ordered in different subgroups based on the organic linkers, such as HAB for Hexa-Amino-Benzene or ZIF for zeolitic-imidazolite-based framework. Depending on the synthesis method and the reagents 2D MOFs also can be produced, establishing again the highly advantageous surface-to-bilk ratio for catalysts. The efficiency CO_2RR to methanol with Fe-HAB MOF was already studied by Tang and co-workers with DFT calculations [13], through the calculation of adsorption energies of COOH* (which is the intermediate of the CO_2RR) and H*, the authors selected the Fe-based candidate out of Fe, Ni, Co

and Cu-HABs. However, as there are many theoretical studies in the literature, the main challenge for 2D MOFs is the synthesis method itself. As the main synthesis methods work only for multilayers, but not for less than 10 layers thickness and large lateral dimensions in the case of coordination polymers. Lahiri and co-workers however overcame this challenge and synthetized 10-15 nm thick nanosheets for M-HAB (M = Ni, Co, Cu) with a gas-liquid interfacial reaction [14], however, the publication did not report catalytic activities. Carbonaceous materials hold a lot of potential for CO_2RR, as with the different dopants/metallic centers, the selectivity of the catalyst can be easily engineered. However, as the synthesis of these materials is not fully developed yet, the cost-efficiency factor still cannot be maximized.

2.2. Structural and Electronic properties of TMDCs

As the cost- and energy-efficiency of traditional metal catalysts show some insufficiency, transition-metal dichalcogenides are gaining a lot of attention as potential alternatives also. TMDCs are semiconducting materials, consisting of MX_2 layers, where a transition metal plane is in-between of two chalcogen planes. Each individual layer, which comprises these three distinct atomic planes, are positioned laterally. The top and bottom chalcogen layers can exhibit either similarity or dissimilarity depending on the phase of the material. The atoms (metal atom with the oxidation state of +4 and chalcogen atom with the oxidation state of -4) in every monolayer (X-M-X) are connected via covalent bonds, whilst each monolayer is connected to the other with Van der Waals forces.

There are different polymorphs of TMDCs distinguished: the H-phase and the T-phase. The H-phase represents a hexagonal structural arrangement, while the T-phase forms an octahedral structure. In figure 2.2 these two phases are presented in side view and top view to show the differences in the structures. The numerical prefix indicates the number of monolayers in the unit cell.

In the 2H-phase, the chalcogen atoms in the different atomic planes of the monolayer are horizontally aligned in the same position but vertically shifted on top of each other, following an 'AbA – BaB' stacking configuration. Here, 'A' and 'B' represent chalcogen atoms, while 'b' and 'a' represent transition metal atoms. This stacking pattern results in a 2D honeycomb lattice with hexagonal symmetry when viewed from the top. In the T-phase, the chalcogen atoms in the monolayer occupy different positions across atomic planes, leading to an 'AbC' stacking configuration. In this structure, the metal atom coordinates with six chalcogen atoms, forming an octahedral structure. This arrangement results in a hexagonal arrangement of chalcogen atoms when viewed from the top. As in

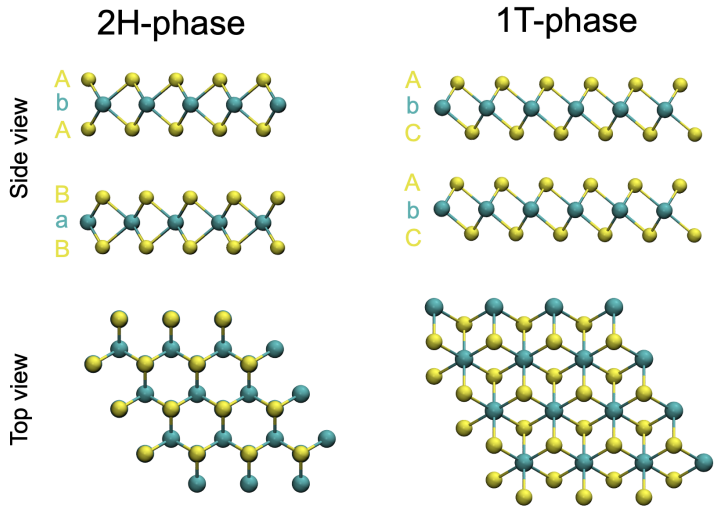

Figure 2.2. Two main phases of MoS_2: 2H-phase (left panel) and 1T-phase (right panel). The top row shows the side view of the different phases, while the bottom row shows the top view of the two phases.

both phases the monolayers are bound by weak interlayer interactions (VdW forces), they can be readily exfoliated through numerous top-down methods, resulting in the synthesis of TMDC monolayers. Furthermore, these different polymorphs exhibiting distinct stacking configurations and metal coordination contributes to the diverse structural and electronic properties observed within TMDCs.

Regarding the electronic properties of TMDCs, the free pair of d-electrons within group 6 transition metals occupies the $a_1^{'}$ (d2 orbital) bands completely. These bands are below the Fermi level, hence, leading to semiconducting behavior in 2H-MoS_2. From this phase, the redistribution of d-orbitals prompts a shift towards the T-phase crystal structure, consequently leading to partial occupancy of the t2g orbital, as illustrated in figure 2.3.

The transition from the stable 2H-phase of group 6-based TMDCs to the metastable T-phase can be induced through various methods, such as intercalation with alkali metals (e.g. Lithium, Sodium and Potassium) or by exposure to a substantial electron beam dosage. During this transformation, from 2H to 1T, the intra-layer atomic planes are gliding on each other ending up in an 'AbC' configuration from the 'AbA - BaB' stacking order.

Ion intercalation represents a conventional and common approach in

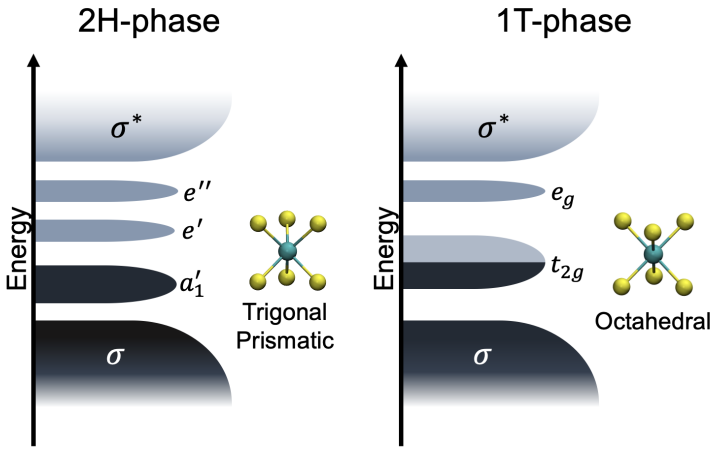

Figure 2.3. Electronic structure of the 2H-phase (left side) and the 1T-phase (right side) for group 6 TMDCs and the belonging unit cells: for the 2H-phase trigonal prismatic, while for the 1T-phase an octahedral coordination.

TMDCs for phase manipulation. In this technique, the initial stable phase undergoes destabilization through a significant alteration in the d-electron count. This alteration occurs via the transfer of an electron from the valence s-orbital of an alkali metal to the d-orbital of the transition metal. Consequently, phase transformation through ion intercalation in Group 6 TMDs results in electronic properties exhibiting metallic behavior.

Due to the various possibilities of intercalants and control of their concentration, many potential applications have been investigated recently, such as the fabrication of supercapacitors [15, 16], solar cells [17] or batteries [18]. In all these cases the main focus is on the intercalation of alkali metal ions (Li^+, Na^+, K^+ and Cs^+).

This intercalation was already studied by Woollam and co-workers in 1977 [19]. The study focused on the superconductivity which is induced by intercalation, they also proposed the possible mechanism that happens during the intercalation and accounts for the phase transformation. Here, the alkali metal ion diffuses into the gap between the MoS_2 layers, which are connected with Van der Waals forces, and donates electrons to the conduction band of the MoS_2. They measured that the superconductivity happens between 3 and 7 K depending on the different alkali metal ions.

In more recent publications, authors mainly focus on the intercalation of Na^+ or Li^+ ion and deciphering the intercalation process itself. Wang and co-workers studied the intercalation-induced phase transition of MoS_2 with Na^+ ions [20]. In their publication, the semiconducting 2H-phase of

MoS_2 goes through a phase transition to 1T-MoS_2 by intercalating Na^+ ions into the interlayer spacing. The 1T-phase shows metallic properties, however, it is also metastable and in air at room temperature can easily transform back to the 2H-MoS_2. The intercalation mechanism and the

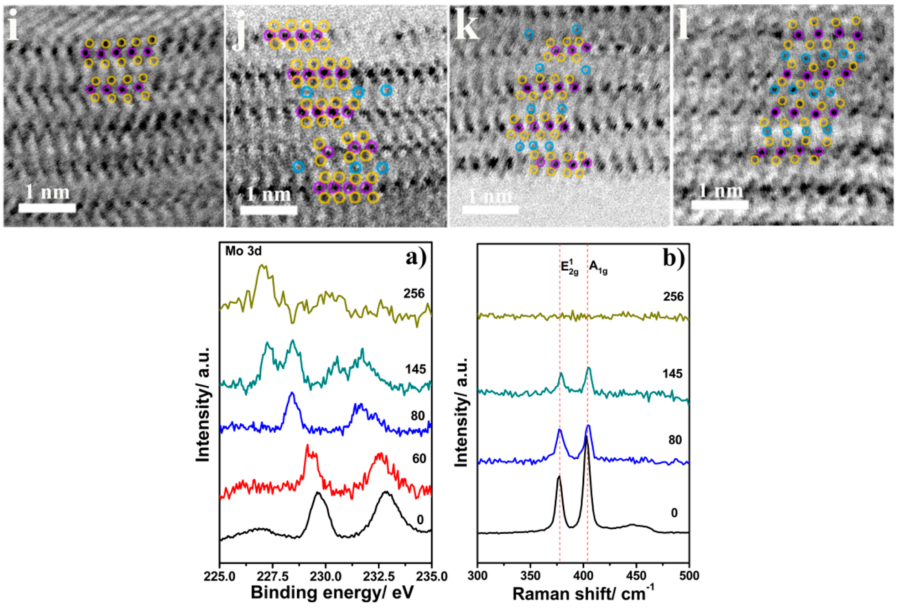

Figure 2.4. Upper: Intercalation process of Na^+ ions into bulk MoS_2. S is yellow, Mo is purple and Na is blue. Lower: XPS **(a)** and Raman **(b)** spectra of the Mo 3d band, which shows the shift in both techniques upon intercalation induced phase transformation. Adapted from [20].

induced phase transition was observed with Scanning Transmission Electron Microscopy (STEM) and is presented in figure 2.4 A. The process consists of three steps:

1. figure 2.4 panel i shows the STEM image of MoS_2 before intercalation,
2. then the Na^+ ions occupy every other layer of the MoS_2 while the other layers stay empty (figure 2.4 panel j),
3. these empty layers starts to get filled up with Na^+ ions before the every other layers are fully occupied (figure 2.4 panel k),
4. During the intercalation process, the sulfur planes start to glide and transforms into the 1T-phase (figure 2.4 panel l).

The authors furthermore showed that the concentration of the intercalants also heavily affects the phase transformation via X-ray photoelectron spectroscopy (XPS) and Raman spectroscopy, see figure 2.4. A down-shift in the XPS spectra indicates the presence of the donated electrons from the intercalants and the same is indicated also by the up-shift of the A_{1g} band in the Raman spectra. The authors further deduce that below 1.5 Na^+ ions per formula MoS_2, the intercalation-induced phase transition happens from 2H to 1T, while above 1.5 Na^+ ions per formula MoS_2, the S-Mo-S bonds break down and well-dispersed metallic Mo clusters can be detected and Na_xS.

The same phenomenon was observed by Wu and co-workers by intercalating Li^+ ions into MoS_2 [21]. Here, the main focus was on the amount of the intercalated Li^+ ions and how it affects the HER. A low concentration of intercalated Li^+ ions absorb on the surface of the MoS_2 and changes the electronic properties, thus, promotes the HER through changing ΔG_{H^*}. At lower Li^+ ion concentrations, the 2H- to 1T-phase transition can be observed, while the decomposition of the S-Mo-S bonds starts at higher Li^+ ion concentrations, same phenomenon as for the intercalation of Na^+ ions.

Attanayake and co-workers compared the effect of intercalation of Na^+, Ca^{2+}, Co^{2+} and Ni^{2+} ions into MoS_2 on the efficiency of HER [22]. The intercalation of Na^+ ions were proved to be the best one based on the reduction of overpotential, charge transfer resistance, double layer capacitance and calculated free energy for HER established with DFT. The analysis of the XPS data obtained on the S 2p bands that the intercalation-induced phase transition created the presence together the 2H- and the 1T-phase, and thus, the coexistence of the two phases created a super lattice structure.

Zheng et al were studying the Li-adsorption induced 2H to 1T phase transition with DFT calculations [23]. The results of the structure optimization showed, that the Li atoms prefer to adsorb at first on the upper side of the MoS_2 layer, and then on the bottom side of the layer, which agrees with the findings of Wang and co-workers [20]. Furthermore, they showed that the electrons of the lithium transfer to the d-orbital of the Mo atoms, which is the essence of the 2H- to 1T-phase transition (see figure 2.3). They showed furthermore, that the phase transition barrier (*"a physical quantity to evaluate the difficulty degree of the phase transition"*) also decreases gradually with the increasing concentration of Li atoms when this amount is less than 100%. Once 100% is reached, the decomposition of MoS_2 begins and with the formation of Mo clusters and the Li_xS.

The intercalation of K atoms and K^+ ions was studied by Andersen and co-workers with first-principle calculations [24]. Simulations were performed for simple intercalations of atoms and ions, and also, the intercalation of ions with their hydration shells. Calculations showed that the ions with the hydration shell can be intercalated into the bulk MoS_2 structure, if the shell

consists of one or two water molecules.

Furthermore, they were investigating the role of the intercalated K^+ ions with regards to the growth of higher linear alcohols based on the potassium's 4s electron donation to the MoS_2's metal core. The heavy alkali metal (K, Cs and Rb) promoted MoS_2 structure is a good catalyst for the production of mixed higher alcohols. The K^+ ions adsorbed on the surface of the MoS_2 influences the alcohol selectivity: **(1)** promotes the adsorption of CO and **(2)** blocks the responsible sites for CO dissociation. However, according to Andersen and co-workers *"The migration mechanism for how these sulfate surface species allow substantial migration of K^+ into the subsurface is not understood."* [24].

The catalytic properties of MoS_2 promoted with potassium in the Fischer-Trops synthesis were studied by Youchang and co-workers [25]. MoS_2 is good catalyst for CO and H_2, however the production yield of liquid hydrocarbons is below 5% when the catalyst is not promoted with any alkali metal ion. When the K_2CO_3 was added to the system as the source of the K^+ ions, the total production yield of alcohols went up to 65%, the reaction conditions were 250 °C and 1000 psi. The authors also examined the promotion with Na_2CO_3, however, the production yield for alcohols were only 29.7%.

The intercalation-induced phase transition of MoS_2 from the semiconducting 2H-phase to the metallic 1T-phase creates potential to tune the electronic and structural properties of the material. Consequently, it opens the door for new applications of the modified material, such as catalysts in electrochemical reactions.

2.3. MoS_2 forcefields in Molecular Dynamics simulations

Molecular dynamics (MD) is a computational simulation technique used to study the trajectory and movements of systems consisting of atoms and molecules over time. Through solving Newton's equations of motion for systems of the interacting particles, MD enables researchers to study the behavior of materials at the atomic scale, providing insights into the structure, dynamics and thermodynamics of molecular systems. The technique has broad applications across different disciplines such as materials science, biophysics, and chemistry, allowing the investigation of processes such as protein folding, ligand binding, and phase transitions in materials [26]. One of the primary strengths of MD lies in its ability to offer atomic-level detail that is often inaccessible through experimental methods, making it an essential tool for hypothesis testing, drug design, and the development of new materials [27]. As computational power and algorithmic efficiency continue to advance, MD simulations are becoming increasingly accurate and capable of capturing longer timescales and

larger systems.

As MoS_2 is a widely used material, researchers were also investigating its mechanical properties with theoretical methods for years now. Molecular Dynamics (MD), among DFT, is a prominent tool to study different material properties, such as diffusion, thermal conductivity, shear force, etc. Regarding the mechanical properties of MoS_2, it is very important to distinguish between simulations studying monolayer MoS_2 and multilayer MoS_2. For monolayer MoS_2, there is only the intra-layer potential which has to be selected properly, meaning the interactions between the S-Mo-S atoms. While for multilayers the among the intra-layer interactions, the

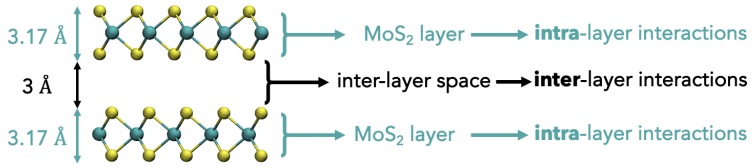

Figure 2.5. Schematics showing the intra-layer interactions and the inter-layer interactions in 2H-MoS_2.

inter-layer interactions have to be considered as well, which represent the Van der Waals forces between the MoS_2 monolayers. In figure 2.5 these interactions are shown.

Starting with the intra-layer potentials, Xiong and co-workers compared different intra-layer potentials (1) to optimize the equilibrium structure of MoS_2 and (2) to optimize the deformed structure under in-plane tension [28]. The potentials were:

- Consistent Valence Forcefield (CVFF)

$$U = \sum U_{bond} + \sum U_{angle} + \sum U_{LJ} + \sum U_C \tag{2.1}$$

  where U_{bond} is the bonding potential, which can be expressed as a Harmonic potential (CVFF1) or as a Morse potential (CVFF2), U_{angle} is the Harmonic angle potential, U_{LJ} is the Lennard-Jones (LJ) non-bonding potential and U_C is the Coulombic potential.

- Stillinger-Weber (SW) potential, where the interaction is described by a two-body and a three-body interaction.

- Reactive Empirical Bond Order (REBO) potential, where the bond interaction is described with a many-body function.

The authors compared the results from the four different empirical potentials with DFT calculations, and CVFF2 and REBO turned out to give the best agreements.

The above-mentioned publication studied only a monolayer MoS_2, where the main question of parametrization is the intra-layer potential. However, for multilayers the force field parameters for the inter-layer interactions also have to be found. Using the Morse or the Harmonic potential equations as the intra-layer potential was also confirmed by Varshney and co-workers [29] for multi-layer MoS_2, where the parameters of Eq. 2.1 were collected from four previous literature data [30–33]. For the inter-layer interactions Lennard-Jones (LJ) potential was used. The authors created nine different parameter sets out of the literature data and studied the agreement with experimental data (crystal structure data and vibration spectra). Figure 2.6 shows the inter-layer distance, the X- and Z-dimensional scaling of the different sets compared to experimental data (dashed line). Two sets show the best agreement: 8 & 9, which also used CVFF1 and CVFF2 potentials as U_{bond}.

Yi and co-workers studied the compression and stretching properties of a multilayer (5 layers) MoS_2, they used the SW potential as intra-layer potential and LJ potential for the inter-layer potential [34]. The authors state that for mechanical properties the parametrization of the inter-layer potential is crucial to obtain the initial structure of the multilayer MoS_2. These parameters were collected from [30, 35] and the simulation results showed the best agreement with experimental data when the LJ parameters from [35] were used. In publication [35], Ding and co-workers

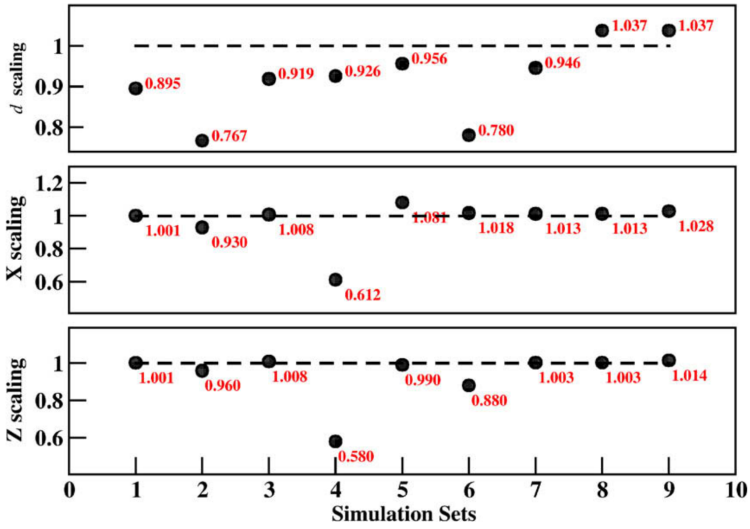

Figure 2.6. Accuracy of different simulation sets reproducing the inter-layer distance and the X- and Z-dimensional scaling. Adapted from [29].

verified their LJ parameters with the argument and calculations, that the inter-layer potential is negligible beyond two layers, as it is already bigger than the cut-off distance.

As, it was shown, for the simulation of monolayer MoS_2, CVFF intra-layer potentials are more preferred, however, to study the properties of multilayer MoS_2, SW potential seems more appropriate to use for the reproduction of the mechanical properties, as it treats the bending the bond as a two-body interaction, while the bending of the angle is described as a three-body interaction. For the intra-layer potential, LJ potential can be used with an optimized cut-off distance in each publication.

The above-listed theoretical studies are mostly focusing on the mechanical [37] and thermal properties [30] of monolayers or multilayers. These handful of force fields became the most popular force fields in the literature (1) by Morita and co-workers [30], (2) by Becker and co-workers [31], (3) by Varshney and co-workers [38], (4) by Jiang and co-workers [37], (5) by Sresht and co-workers [36] and (6) by Liang and co-workers [39, 40] and therefore they are majorly used also by other researchers for studying multilayers (parameters of these force fields are collected in Table 2.1). Most of the above-mentioned studies are using the Harmonic potential to describe the bond between the Mo atom and the S atom. There are two exceptions: Morita and co-workers used the Morse potential [30] and Liang and co-workers, where a reactive empirical bond order (REBO) specifically for MoS_2 (REBOMOS) potential was developed [39, 40]. However, while one developed force field is correctly representing one specific property, it might lack accuracy with other properties, such as the interaction with water. Sresht and co-workers even proved that though these potentials describe the given mechanical and/or thermal property

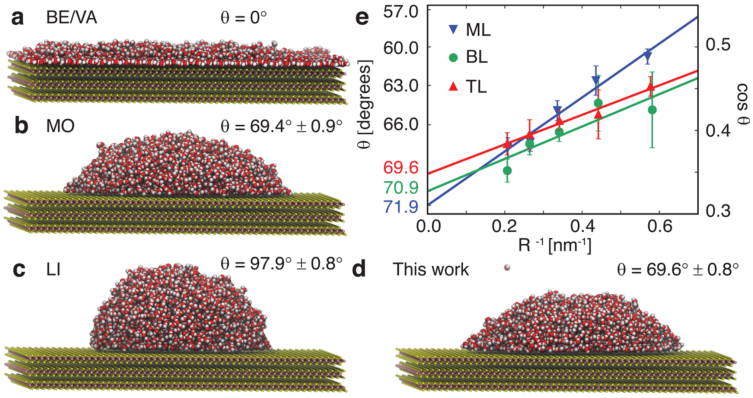

Figure 2.7. Snapshots of water droplet simulations and the calculated WCA based on different water droplet sizes. Adapted from [36].

they are developed for, they fail to reproduce the experimental water contact angle (WCA) when they are brought in contact with water [36].

Therefore, F. Leroy derived new LJ parameters for MoS_2, based on three of these popular force fields [38–41], which represent the WCA and adhesion parameters correctly [42] for various water models. The study is using the work of adhesion (W_{ad}) as a basis for the WCA calculation through the Young-Dupré equation, and thus, eliminating the dependency of the WCA on the size of the water droplet. The same method was used

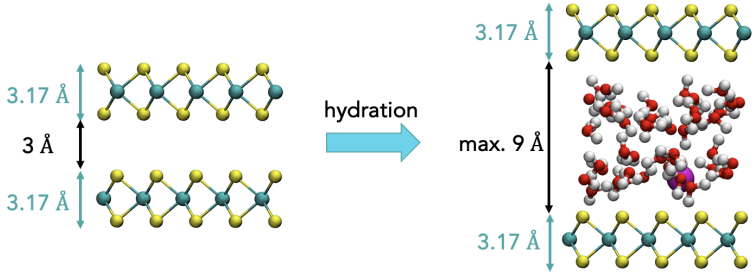

Figure 2.8. Schematics of hydration effect on MoS_2: the inter-layer distance increases from 3 Å to max. 9 Å.

by Zhang and co-workers, where a water droplet was placed on a trilayer MoS_2 sheet and with the scaling of the energy parameter for the sulfur atoms in the LJ potential, the W_{ad} was estimated [43]. Another approach was done by Luan and co-workers, where they proposed optimized LJ parameters for MoS_2 interacting with water molecules (TIP3P water model) based on the OPLS-AA force field [41], while Sose and co-workers derived new parameters sets for SPC, SPC/E, SPC/Fw water models while using the Stillinger-Weber potential for the MoS_2 [44]. In both studies, different water droplet sizes were simulated and then, a linear extrapolation was made to the macroscopic WCA. All these studies show however, that the interaction between water molecules and MoS_2 cannot be randomly enforced and the cross-interaction parameters have to be tuned for the chosen MoS_2 force field and water model.

Another important factor which should be taken into account regarding the interactions between water and MoS_2 sheets is the hydration and "swelling" of the bulk. Wang et al. studied and showed that when a bulk MoS_2 is brought in contact with water, the interlayer distance increases from 3 Å to a maximum of 9 Å [45]. Figure 2.8 shows this hydration effect in schematics. This swelling due to the hydration makes the intercalation of ions possible, as the insertion of an ion with its hydration shell fits in the hydrated interlayer distance.

Parameters		Morita et al. [30]	Becker et al. [31]	Varshney et al. [29]	Jiang et al. [37]	Sresht et al. [36]	Liang et al. [39]
Mo-S bond	Morse^1 (D, α, r_0)		19.94, 0.858, 2.54				
	Morse^2 (D, α, r_0)	0.398, 1.98, 2.39					
	Harmonic (K, r_0)			4.3213, 2.41		4.45975, 2.41	
	Other				SW		REBOMOS
Non-bonded in LJ	Mo-Mo (ϵ, σ)	0.8382, 2.5510	1.5549, 2.2310	0.8382, 2.5510	0.00243, 2.7190	0.005027, 4.43	0.0005859, 3.20
	S-S (intra-plane) (ϵ, σ)	0.0019, 3.3695	0.2981, 3.0023	0.0606, 3.3695	0.01187, 3.5950	0.029538, 3.34	0.020, 3.13
	S-S (inter-plane) (ϵ, σ)	0.0019, 3.3695	0.1656, 3.0138	0.0606, 3.3695	0.01187, 3.5950	0.029538, 3.34	0.020, 3.13
	Mo-S (ϵ, σ)	0.0399, 2.9318	1.3802, 2.9028	0.0339, 2.9318	0.02489, 3.1570		0.0028, 3.665
Angle coefficients	Mo-S-Mo (K, Θ)	2.5163, 82.00	0.8968, 81.67	3.4297, 81.67		21.247, 83.8	
	S-Mo-S (K, Θ)	2.5163, 82.00	0.6356, 81.78	2.7227, 81.78		12.309, 83.8	
Pratial charges (e)	Mo	0.76	0.734	0.76	0	0.5	0
	S	-0.38	-0.367	-0.38	0	-0.25	0

Table 2.1. Often used force fields collected, the distance, energy and angle values are in Å, eV and degrees, respectively. Morse^1 potential: $D \times ((1 - e^{-\alpha(r-r_0)})^2 - 1)$, Morse^2 potential: $D \times (1 - e^{-2\alpha(r-r_0)} - 2e^{-\alpha(r-r_0)})$, Harmonic potential: $K \times (r - r_0)^2$, LJ potential: $4\epsilon[(\frac{\sigma}{r})^{12} - (\frac{\sigma}{r})^6]$

2.4. Catalytic properties of TMDCs

Out of all TMDCs, catalytic properties of molybdenium-sulfide (MoS_2) and tungsten-sulfide (WS_2) are the most well-known and more broadly studied catalyst materials [46–48]. Asadi and co-workers studied the ability of bulk MoS_2 to reduce CO_2 and emphasized the importance of the edges in the material during the catalysis process [46]. MoS_2 is a layered material, hence, there is a large number of edges present on the surface. In figure 2.9 (a), the line scans of STEM are presented, which shows that the edges of the bulk MoS_2 are mainly Mo-terminated (red and blue lines), as this type of termination has the lowest formation energy in the case of a free-standing single-layer MoS_2 [49].

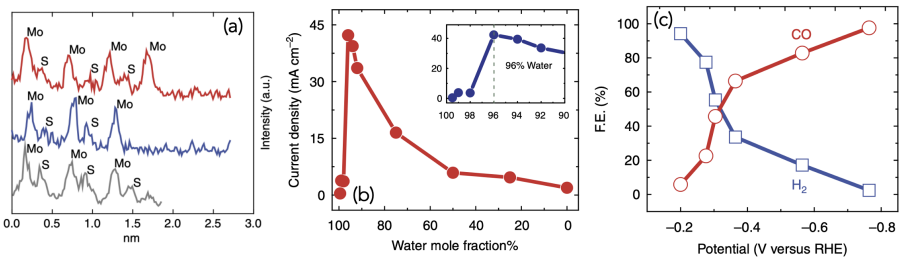

Figure 2.9. **(a)** STEM line scans for the identification of the edge-terminating atoms (blue and red lines are towards the edges, grey line shows the presence of a substitutional defect atom, most probably carbon, **(b)** CO_2 reduction current density at different [EMIM][BF_4] concentrations, **(c)** Faradaic efficiency of CO_2RR and HER at different potentials. Adapted from [46].

The evaluation of the catalytic activity of the bulk MoS_2 was carried out in ionic liquid, specifically 1-ethyl-3-methylimidazolium tetrafluoroborate ([EMIM]-[BF_4]), diluted with water. As MoS_2 is very much prone to HER, the CO_2RR is suppressed in a competing situation, hence, the ionic liquid is used as co-catalyst in the CO_2RR. In the research, results of quantum Molecular Dynamics (MD) simulations are also presented, which show that the cation of the ionic liquid ($[EMIM]^+$) forms a complex with the CO_2^+ ([EMIM]-CO_2^+) and this complex physisorbes on the catalyst surface. The physisorbed complex hinders the access of the water molecules to the surface of the catalyst, hence blocking the HER and promoting the CO_2RR. Furthermore, the physisorbed [EMIM]-CO_2 complex also reduces the reaction barrier for the CO_2RR on the MoS_2 surface. Thus, a high FE of the CO_2RR can be attributed to the synergy of the MoS_2 catalyst and the co-catalyst [EMIM][BF_4].

In figure 2.9 (b) the current density of CO_2 reduction is monitored at different concentrations of CO_2-saturated [EMIM]-[BF_4]. As pH value of

the electrolyte changes with the addition of water, hence the rate of the electrochemical reduction is also affected. The highest current density was measured at 4 mol% [EMIM]-[BF_4] and 96 mol% water.

Figure 2.9 (c) shows the FE of CO_2 reduction at different potentials in an electrolyte composed of 4 mol% [EMIM]-[BF_4] and 96 mol% water. At lower potentials, the HER is the preferred reduction reaction and as the potential is increased, the CO_2RR towards CO becomes the dominant reaction. However, it has to be emphasized that the ionic liquid co-catalyst plays a crucial role in this behavior.

In a later publication, Abbasi and co-workers studied the effect of doping MoS_2 with Nb and Ta atoms on the efficiency of CO_2RR [47]. In this study, vertically-aligned MoS_2 was synthesized with CVD and its electrochemical activity was tested based on the dopant quality and quantity. The reason behind the doping is the metallic behavior of TaS_2 and NbS_2, which could enhance the activity of the Mo edge-atoms for CO_2RR.

In figure 2.10 (a) the current density belonging to different dopant concentrations is presented in an electrolyte of 50 mol% [EMIM]-[BF_4] and 50 mol% water. The Nb-doped MoS_2 exhibits high current densities at low doping percentages, while Ta-doped MoS_2 shows relatively low and even decreasing current densities compared to the pristine MoS_2. This underperformance is attributed to the deviation from an optimal electronic structure of Ta-doped MoS_2. This difference between the Ta-

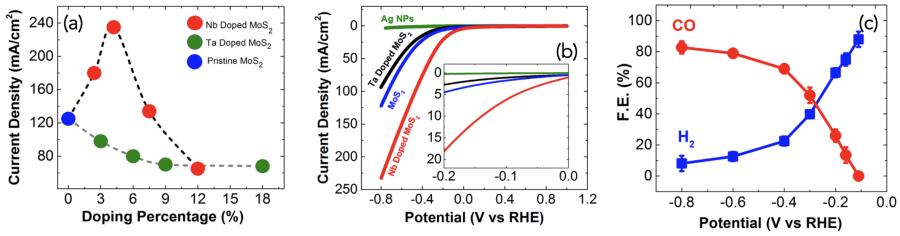

Figure 2.10. **(a)** Change in current density with the dopant concentration, **(b)** CV curves of Ag nanoparticles, VA-MoS_2 and Ta- and Nb-doped MoS_2, **(c)** Faradaic efficiency of HER and CO_2RR of Nb-doped MoS_2. Adapted from [47].

and Nb-doped MoS_2 can also be clearly seen on the cyclic voltammetry (CV) curves in figure 2.10 (b) (still in 50 mol% [EMIM]-[BF_4] solution). The catalytic performance is presented in figure 2.10 (c) of the Nb-doped MoS_2, where the same trend is shown as for the pristine MoS_2: at -0.8 V vs RHE the FE for CO_2RR is the highest and as the potential is decreased, the HER becomes dominant.

In another publication, the same research group studied and compared the electrocatalytic behavior of different TMDCs: MoS_2, $MoSe_2$, WS_2 and WSe_2 [48]. The different TMDC nanoflakes were synthesized via Chemical Vapor Transport technique, the average size of the nanoflakes was 100 nm. Unlike, for the bulk MoS_2 (figure 2.9), for the nanoflakes a different composition of electrolyte was found to be optimal: 50 mol% [EMIM]-[BF_4] and 50 mol% water due to the increased amount of exposed Mo-terminated edges. This optimization can be seen in figure 2.11 (a), where the current density and the pH is measured at different electrolyte compositions. At 50 mol% [EMIM]-[BF_4], where the pH shows the highest acidity, the WSe_2 catalyst shows also the highest current density, as there are also protons needed for the CO_2RR as well as electrons. Hence, the low pH value is crucial for the electrocatalysis, as DFT calculations showed [46] that the rate of the CO_2RR depends on the concentration of protons. The maximum rate for the CO_2RR can be reached with a low pH (high

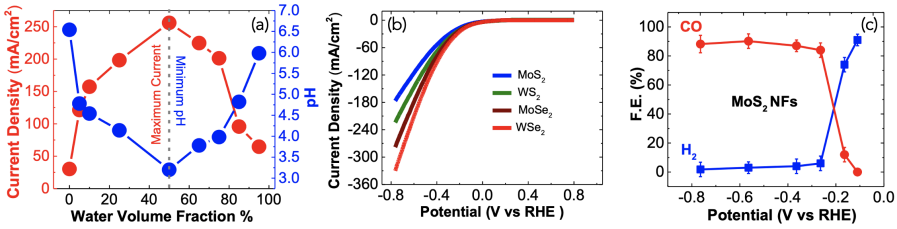

Figure 2.11. **(a)** Current density and pH at different concentrations of EMIM-BF_4, **(b)** CV curves of the different catalyst materials, **(c)** Faradaic efficiency of HER and CO_2RR using MoS_2 as catalyst. Adapted from [48].

concentration of protons) and the low viscosity of the media. In figure 2.11 (b), the linear sweep voltammetry (LSV) curves are presented, belonging to the different catalyst materials. MoS_2 shows the lowest current density in the scanned potential range, while the highest current density belongs to WSe_2. The FEs of HER and CO_2RR of the MoS_2 nanoflakes are shown in figure 2.11 (c), where the behavior is similar to the previously shown bulk MoS_2 and CVD-grown doped MoS_2. The CO_2RR becomes the dominant -0.2 V vs RHE, and then it shows a 90% FE towards CO production.

As mentioned previously, the complex formation of the $[EMIM]^+$ cation in the ionic liquid with the CO_2 molecule and the physisorption of this complex on the surface of the MoS_2 catalyst plays a crucial role in achieving the high FE for CO_2RR. Francis and co-workers proved this by studying the CO_2RR on single-crystal-terrace MoS_2 electrodes (mechanically exfoliated MoS_2) in 0.1 M Na_2CO_3 aqueous solution, where

they showed that the HER reaction suppressed the CO_2RR drastically [50]. However, they also showed that with the high amount of exposed edges the primary products of the CO_2RR in aqueous media were 1-propanol and formate, furthermore, ethylene glycol, methanol and t-butanol were also detectable in trace amounts.

Based on the available experimental information, Xie and co-workers used DFT calculations to show why CO is the main product of the CO_2RR on MoS_2 and how the reaction path goes [51]. As the reaction takes place on the exposed Mo edges, they showed that the d-band center of the Mo atom is much closer to the Fermi level than for metallic catalysts, such as copper or titanium, therefore, the adsorbed species are interacting much stronger with the Mo atoms also. Furthermore, assuming that the intermediates are COOH* and CO*, their free energy are smaller than of CO_2 and CO (the primary product), thus the Mo atoms on the edges also exhibit a strong binding of the intermediates. In the whole reaction path of converting CO_2 to products, the authors distinguished five main steps, see figure 2.12.

The first step is the activation of the CO_2 molecule. The authors calculated that the most stable configuration of the adsorbed CO_2 is in a bridging position between two Mo atoms, where the two oxygen atoms connect to the Mo atoms (see figure 2.12 step 1). Here, the lone pair of p electrons of the oxygen atom and the carbon atom and the d electron of the Mo atom ends up forming p-d hybridized orbitals. Thus, this new bonding breaks the C-O bond in the CO_2 molecule resulting in the activated CO_2^*.

After the activation, the first hydrogenation step happens, where the reaction can follow path 2^a or path 2^b producing two different intermediates. Path 2^b has a higher free energy than 2^a, hence, it is less likely to happen. Furthermore, to achieve the CO* intermediate through path 2^b an extra hydrogenation reaction needs to happen through path 3^a which also has an additional reaction barrier (0.40 eV). Additionally, path 3^b has an even higher activation energy, about 1.47 eV, hence the product formation is less likely to happen through paths 2^b, 3^a and 3^b, meaning that the products are more likely formed from the hydrogenation of CO* than COOH*.

From the CO* intermediate the next hydrogenation step can result in the CO product (path 4^a) or in COH* intermediate (path 4^b). However, the activation energy for path 4^b is 2.1 eV, thus is makes the hydrocarbon production less likely (as path 5 still needs an extra hydrogenation step) and the formation of CO as the main possible product. In figure 2.12 the more likely reactions are highlighted with a green line, which confirms the findings of the Asadi group [46–48] and strongly differs from the findings of Francis and co-workers [50]. However, the circumstances of the two CO_2RR are also different as Asadi and co-workers used CVD-grown MoS_2 monolayers in ionic liquid, while Francis and co-workers used exfoliated

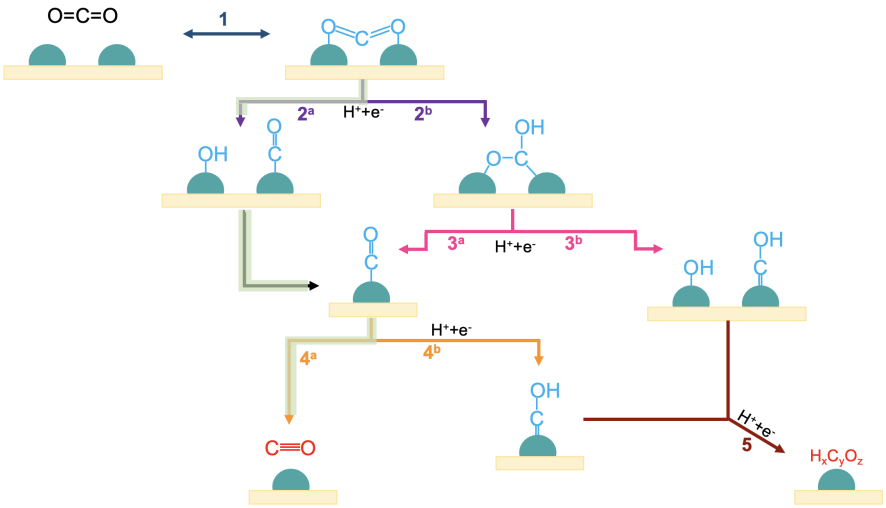

Figure 2.12. Reaction pathway of CO_2RR on MoS_2 with 5 main steps, the green highlight shows the most probable path based on DFT calculations. The adsorbed species on the Mo atoms are indicated with an asterisk in the text.

single-crystal-terrace MoS_2 electrodes in aqueous solutions.

Another very important feature of MoS_2 and TMDCs in general is the deviation from the linear scaling relations between the intermediates of the CO_2RR, see figure 2.13 [52]. The main potential-dependent steps are:

$$CO_{2(g)} + H^+ + e^- \rightarrow COOH* \tag{2.2}$$

$$COOH^+ + H^+ + e^- \rightarrow CO* + H_2O \tag{2.3}$$

$$CO* + H^+ + e^- \rightarrow CHO* \tag{2.4}$$

which are shown in figure 2.12 as paths 2^b, 3^a and 4^b, respectively (energetically not favorable reactions according to Xie and co-workers [51]). The linear scaling shows that for the different transition-metal catalysts that the adsorption energies of the COOH* and the CHO* are strongly correlated with the adsorption energy of the CO* [53]. Hence, these linear scaling relations between the reaction intermediates of the CO_2RR and they strongly affect the reduction activity of the transition-metal catalysts (including Au, Ag, Pt, Ni, etc.). These relations also suggest that the stability of COOH* and CHO* are strongly dependent on CO*, whereas a criteria for the catalyst would be to stabilize COOH* and CHO* better than CO*. However, as it is shown in figure 2.13, MoS_2 and $MoSe_2$ (both pristine and doped) break these scaling relations by binding the COOH* and CHO*

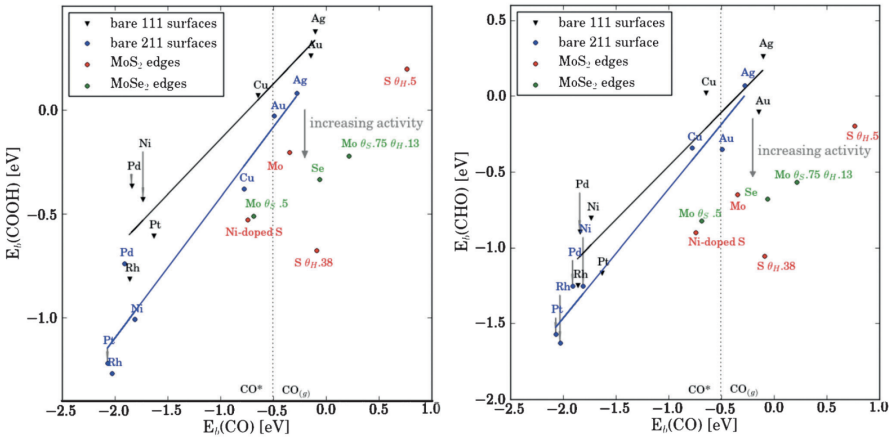

Figure 2.13. Linear scaling relations for different transition-metals and the breaking of these relations by TMDCs. Adapted from [52].

more strongly than the CO*/CO. This phenomenon is attributed to the presence of S and Se atoms on the edges of the MoS_2 and $MoSe_2$, which have a higher binding affinity towards the intermediates and not to CO. This shows that MoS_2 can not only be an efficient catalyst for CO_2RR under the right circumstances but also that the edge structure can be tuned towards higher selectivity of products.

In conclusion, TMDCs are potential alternatives to the classical metal electrodes for CO_2RR. They fulfill the criterion of cost-efficiency, they can reach a high FE towards CO production and possibly opening new reaction paths towards higher hydrocarbons and alcohols. Due to their special layered structure, their dimensions can be reduced to 2D from 3D, thus increasing the surface-to-bulk ratio, which is the most important feature of novel catalyst materials. The intercalation-induced phase change can affect and improve the electronic properties of the TMDCs and also gives the opportunity to engineer their band gaps. The only drawback of using TMDCs as catalyst materials is the requirement of the organic co-catalysts. However, this feature can also be substituted with the growth of monolayers that act as hydrophobic barriers for the HER and thus promote CO_2RR.

references

[1] Y. Hori, K. Kikuchi, and S. Suzuki. "PRODUCTION OF CO AND CH4IN ELECTROCHEMICAL REDUCTION OF CO_2 AT METAL ELECTRODES IN AQUEOUS HYDROGENCARBONATE SOLUTION". In: *Chemistry Letters* 14.11 (1985), pp. 1695–1698. DOI: 10.1246/cl.1985.1695. URL: https://doi.org/10.1246%2Fcl.1985.1695.

[2] A. Murata and Y. Hori. "Product Selectivity Affected by Cationic Species in Electrochemical Reduction of CO_2 and CO at a Cu Electrode". In: *Bulletin of the Chemical Society of Japan* 64.1 (1991), pp. 123–127. DOI: 10.1246/bcsj.64.123. URL: https://doi.org/10.1246%2Fbcsj.64.123.

[3] Y. Hori, H. Wakebe, T. Tsukamoto, and O. Koga. "Electrocatalytic process of CO selectivity in electrochemical reduction of CO_2 at metal electrodes in aqueous media". In: *Electrochimica Acta* 39.11-12 (1994), pp. 1833–1839. DOI: 10.1016/0013-4686(94)85172-7. URL: https://doi.org/10.1016%2F0013-4686%2894%2985172-7.

[4] Y. Hori, H. Wakebe, T. Tsukamoto, and O. Koga. "Adsorption of CO accompanied with simultaneous charge transfer on copper single crystal electrodes related with electrochemical reduction of CO_2 to hydrocarbons". In: *Surface Science* 335 (1995), pp. 258–263. DOI: 10.1016/0039-6028(95)00441-6. URL: https://doi.org/10.1016%2F0039-6028%2895%2900441-6.

[5] Y. Hori, I. Takahashi, O. Koga, and N. Hoshi. "Selective Formation of C2 Compounds from Electrochemical Reduction of CO_2 at a Series of Copper Single Crystal Electrodes". In: *The Journal of Physical Chemistry B* 106.1 (2001), pp. 15–17. DOI: 10.1021/jp013478d. URL: https://doi.org/10.1021%2Fjp013478d.

[6] D. Kim, J. Resasco, Y. Yu, A. M. Asiri, and P. Yang. "Synergistic geometric and electronic effects for electrochemical reduction of carbon dioxide using gold–copper bimetallic nanoparticles". In: *Nature Communications* 5.1 (2014). DOI: 10.1038/ncomms5948. URL: https://doi.org/10.1038%2Fncomms5948.

[7] A. H. Castro Neto, F. Guinea, N. M. R. Peres, K. S. Novoselov, and A. K. Geim. "The electronic properties of graphene". In: *Reviews of Modern Physics* 81.1 (Jan. 2009), pp. 109–162. ISSN: 1539-0756. DOI: 10.1103/revmodphys.81.109. URL: http://dx.doi.org/10.1103/revmodphys.81.109.

[8] C. Soldano, A. Mahmood, and E. Dujardin. "Production, properties and potential of graphene". In: *Carbon* 48.8 (2010), pp. 2127–2150. ISSN: 0008-6223. DOI: 10.1016/j.carbon.2010.01.058. URL: http://dx.doi.org/10.1016/j.carbon.2010.01.058.

[9] J. Wu, M. Liu, P. P. Sharma, R. M. Yadav, L. Ma, Y. Yang, X. Zou, X.-D. Zhou, R. Vajtai, B. I. Yakobson, J. Lou, and P. M. Ajayan. "Incorporation of Nitrogen Defects for Efficient Reduction of CO_2 via Two-Electron Pathway on Three-Dimensional Graphene Foam". In: *Nano Letters* 16.1 (2015), pp. 466–470. DOI: 10.1021/acs.nanolett.5b04123. URL: https://doi.org/10.1021%2Facs.nanolett.5b04123.

[10] P. Su, K. Iwase, S. Nakanishi, K. Hashimoto, and K. Kamiya. "Nickel-Nitrogen-Modified Graphene: An Efficient Electrocatalyst for the Reduction of Carbon Dioxide to Carbon Monoxide". In: *Small* 12.44 (2016), pp. 6083–6089. DOI: 10.1002/smll.201602158. URL: https://doi.org/10.1002%2Fsmll.201602158.

[11] W. Ju, A. Bagger, G.-P. Hao, A. S. Varela, I. Sinev, V. Bon, B. R. Cuenya, S. Kaskel, J. Rossmeisl, and P. Strasser. "Understanding activity and selectivity of metal-nitrogen-doped carbon catalysts for electrochemical reduction of CO_2". In: *Nature Communications* 8.1 (2017). DOI: 10.1038/s41467-017-01035-z. URL: https://doi.org/10.1038%2Fs41467-017-01035-z.

[12] L. Zhao, Y. Zhang, L.-B. Huang, X.-Z. Liu, Q.-H. Zhang, C. He, Z.-Y. Wu, L.-J. Zhang, J. Wu, W. Yang, L. Gu, J.-S. Hu, and L.-J. Wan. "Cascade anchoring strategy for general mass production of high-loading single-atomic metal-nitrogen catalysts". In: *Nature Communications* 10.1 (2019). DOI: 10.1038/s41467-019-09290-y. URL: https://doi.org/10.1038%2Fs41467-019-09290-y.

[13] M. Tang, H. Shen, and Q. Sun. "Two-Dimensional Fe-Hexaaminobenzene Metal–Organic Frameworks as Promising CO_2 Catalysts with High Activity and Selectivity". In: *The Journal of Physical Chemistry C* 123.43 (2019), pp. 26460–26466. DOI: 10.1021/acs.jpcc.9b08359. URL: https://doi.org/10.1021%2Facs.jpcc.9b08359.

[14] N. Lahiri, N. Lotfizadeh, R. Tsuchikawa, V. V. Deshpande, and J. Louie. "Hexaaminobenzene as a building block for a Family of 2D Coordination Polymers". In: *Journal of the American Chemical Society* 139.1 (2016), pp. 19–22. DOI: 10.1021/jacs.6b09889. URL: https://doi.org/10.1021%2Fjacs.6b09889.

[15] S. Mukherjee, Z. Ren, and G. Singh. "Beyond Graphene Anode Materials for Emerging Metal Ion Batteries and Supercapacitors". In: *Nano-Micro Letters* 10.4 (Oct. 2018). DOI: 10.1007/s40820-018-0224-2. URL: https://doi.org/10.1007%2Fs40820-018-0224-2.

[16] M. A. Bissett, S. D. Worrall, I. A. Kinloch, and R. A. Dryfe. "Comparison of Two-Dimensional Transition Metal Dichalcogenides for Electrochemical Supercapacitors". In: *Electrochimica Acta* 201 (May 2016), pp. 30–37. DOI: 10.1016/j.electacta.2016.03.190. URL: https://doi.org/10.1016%2Fj.electacta.2016.03.190.

[17] P. Huang, Z. Wang, Y. Liu, K. Zhang, L. Yuan, Y. Zhou, B. Song, and Y. Li. "Water-Soluble 2D Transition Metal Dichalcogenides as the Hole-Transport Layer for Highly Efficient and Stable p–i–n Perovskite Solar Cells". In: *ACS Applied Materials & Interfaces* 9.30 (2017), pp. 25323–25331. DOI: 10.1021/acsami.7b06403. URL: https://doi.org/10.1021%2Facsami.7b06403.

[18] M. Pumera, Z. Sofer, and A. Ambrosi. "Layered transition metal dichalcogenides for electrochemical energy generation and storage". In: *J. Mater. Chem. A* 2.24 (2014), pp. 8981–8987. DOI: 10.1039/c4ta00652f. URL: https://doi.org/10.1039%2Fc4ta00652f.

[19] J. A. Woollam and R. B. Somoano. "Physics and chemistry of MoS_2 intercalation compounds". In: *Materials Science and Engineering* 31 (1977), pp. 289–295. DOI: 10.1016/0025-5416(77)90048-9. URL: https://doi.org/10.1016%2F0025-5416%2877%2990048-9.

[20] X. Wang, X. Shen, Z. Wang, R. Yu, and L. Chen. "Atomic-Scale Clarification of Structural Transition of MoS_2 upon Sodium Intercalation". In: *ACS Nano* 8.11 (2014), pp. 11394–11400. DOI: 10.1021/nn505501v. URL: https://doi.org/10.1021%2Fnn505501v.

[21] L. Wu, N. Y. Dzade, M. Yu, B. Mezari, A. J. F. van Hoof, H. Friedrich, N. H. de Leeuw, E. J. M. Hensen, and J. P. Hofmann. "Unraveling the Role of Lithium in Enhancing the Hydrogen Evolution Activity of MoS_2: Intercalation versus Adsorption". In: *ACS Energy Letters* 4.7 (2019), pp. 1733–1740. DOI: 10.1021/acsenergylett.9b00945. URL: https://doi.org/10.1021%2Facsenergylett.9b00945.

[22] N. H. Attanayake, A. C. Thenuwara, A. Patra, Y. V. Aulin, T. M. Tran, H. Chakraborty, E. Borguet, M. L. Klein, J. P. Perdew, and D. R. Strongin. "Effect of Intercalated Metals on the Electrocatalytic Activity of 1T-MoS_2 for the Hydrogen Evolution Reaction". In: *ACS Energy Letters* 3.1 (2017), pp. 7–13. DOI: 10.1021/acsenergylett.7b00865. URL: https://doi.org/10.1021%2Facsenergylett.7b00865.

[23] Y. Zheng, Y. Huang, H. Shu, X. Zhou, J. Ding, X. Chen, and W. Lu. "The effect of lithium adsorption on the formation of 1T-MoS_2 phase based on first-principles calculation". In: *Physics Letters A* 380.20 (2016), pp. 1767–1771. DOI: 10.1016/j.physleta.2016.03.009. URL: https://doi.org/10.1016%2Fj.physleta.2016.03.009.

[24] A. Andersen, S. M. Kathmann, M. A. Lilga, K. O. Albrecht, R. T. Hallen, and D. Mei. "First-Principles Characterization of Potassium Intercalation in Hexagonal 2H-MoS_2". In: *The Journal of Physical Chemistry C* 116.2 (2012), pp. 1826–1832. DOI: 10.1021/jp206555b. URL: https://doi.org/10.1021%2Fjp206555b.

[25] X. Youchang, B. Naasz, and G. Somorjai. "Alcohol synthesis from Co and H2 over molybdenum sulfide. The effect of pressure and promotion by potassium carbonate". In: *Applied Catalysis* 27.2 (1986), pp. 233–241. DOI: 10.1016/s0166-9834(00)82920-6. URL: https://doi.org/10.1016%2Fs0166-9834%2800%2982920-6.

[26] D. C. Rapaport. *The art of molecular dynamics simulation*. Cambridge university press, 2004.

[27] R. O. Dror, R. M. Dirks, J. Grossman, H. Xu, and D. E. Shaw. "Biomolecular simulation: a computational microscope for molecular biology". In: *Annual review of biophysics* 41 (2012), pp. 429–452.

[28] S. Xiong and G. Cao. "Molecular dynamics simulations of mechanical properties of monolayer MoS2". In: *Nanotechnology* 26.18 (2015), p. 185705. DOI: 10.1088/0957-4484/26/18/185705. URL: https://doi.org/10.1088%2F0957-4484%2F26%2F18%2F185705.

[29] V. Varshney, S. S. Patnaik, C. Muratore, A. K. Roy, A. A. Voevodin, and B. L. Farmer. "MD simulations of molybdenum disulphide (MoS2): Force-field parameterization and thermal transport behavior". In: *Computational Materials Science* 48.1 (2010), pp. 101–108. DOI: 10.1016/j.commatsci.2009.12.009. URL: https://doi.org/10.1016%2Fj.commatsci.2009.12.009.

[30] Y. Morita, T. Onodera, A. Suzuki, R. Sahnoun, M. Koyama, H. Tsuboi, N. Hatakeyama, A. Endou, H. Takaba, M. Kubo, C. A. D. Carpio, T. Shin-yoshi, N. Nishino, A. Suzuki, and A. Miyamoto. "Development of a new molecular dynamics method for tribochemical reaction and its application to formation dynamics of MoS2 tribofilm". In: *Applied Surface Science* 254.23 (2008), pp. 7618–7621. DOI: 10.1016/j.apsusc.2008.01.123. URL: https://doi.org/10.1016%2Fj.apsusc.2008.01.123.

[31] U. Becker, K. M. Rosso, R. Weaver, M. Warren, and M. F. Hochella. "Metal island growth and dynamics on molybdenite surfaces". In: *Geochimica et Cosmochimica Acta* 67.5 (2003), pp. 923–934. DOI: 10.1016/s0016-7037(02)01144-4. URL: https://doi.org/10.1016%2Fs0016-7037%2802%2901144-4.

[32] N. Wakabayashi, H. G. Smith, and R. M. Nicklow. "Lattice dynamics of hexagonal MoS2studied by neutron scattering". In: *Physical Review B* 12.2 (1975), pp. 659–663. DOI: 10.1103/physrevb.12.659. URL: https://doi.org/10.1103%2Fphysrevb.12.659.

[33] K. Weiss and J. M. Phillips. "Calculated specific surface energy of molybdenite (MoS2)". In: *Physical Review B* 14.12 (1976), pp. 5392–5395. DOI: 10.1103/physrevb.14.5392. URL: https://doi.org/10.1103%2Fphysrevb.14.5392.

[34] C. Yi, C. Hu, M. Bai, J. Lv, and D. Tang. "Molecular dynamics study on the mechanical properties of multilayer MoS2 under different potentials". In: *Nanotechnology* 31.21 (2020), p. 215703. DOI: 10.1088/1361-6528/ab73b3. URL: https://doi.org/10.1088%2F1361-6528%2Fab73b3.

[35] Z. Ding, J.-W. Jiang, Q.-X. Pei, and Y.-W. Zhang. "In-plane and cross-plane thermal conductivities of molybdenum disulfide". In: *Nanotechnology* 26.6 (2015), p. 065703. DOI: 10.1088/0957-4484/26/6/065703. URL: https://doi.org/10.1088%2F0957-4484%2F26%2F6%2F065703.

[36] V. Sresht, A. G. Rajan, E. Bordes, M. S. Strano, A. A. Pádua, and D. Blankschtein. "Quantitative Modeling of MoS2Solvent Interfaces: Predicting Contact Angles and Exfoliation Performance using Molecular Dynamics". In: *The Journal of Physical Chemistry C* 121.16 (Mar. 2017), pp. 9022–9031. DOI: 10.1021/acs.jpcc.7b00484. URL: https://doi.org/10.1021%2Facs.jpcc.7b00484.

[37] J.-W. Jiang, H. S. Park, and T. Rabczuk. "Molecular dynamics simulations of single-layer molybdenum disulphide (MoS2): Stillinger-Weber parametrization, mechanical properties, and thermal conductivity". In: *Journal of Applied Physics* 114.6 (Aug. 2013), p. 064307. DOI: 10.1063/1.4818414. URL: https://doi.org/10.1063%2F1.4818414.

[38] V. Varshney, S. S. Patnaik, C. Muratore, A. K. Roy, A. A. Voevodin, and B. L. Farmer. "MD simulations of molybdenum disulphide (MoS2): Force-field parameterization and thermal transport behavior". In: *Computational Materials Science* 48.1 (Mar. 2010), pp. 101–108. DOI: 10.1016/j.commatsci.2009.12.009. URL: https://doi.org/10.1016%2Fj.commatsci.2009.12.009.

[39] T. Liang, S. R. Phillpot, and S. B. Sinnott. "Parametrization of a reactive many-body potential for Mo–S systems". In: *Physical Review B* 79.24 (June 2009). DOI: 10.1103/physrevb.79.245110. URL: https://doi.org/10.1103%2Fphysrevb.79.245110.

[40] T. Liang, S. R. Phillpot, and S. B. Sinnott. "Erratum: Parametrization of a reactive many-body potential for Mo–S systems [Phys. Rev. B 245110 (2009)]". In: *Physical Review B* 85.19 (May 2012). DOI: 10.1103/physrevb.85.199903. URL: https://doi.org/10.1103%2Fphysrevb.85.199903.

[41] B. Luan and R. Zhou. "Wettability and friction of water on a MoS2nanosheet". In: *Applied Physics Letters* 108.13 (Mar. 2016), p. 131601. DOI: 10.1063/1.4944840. URL: https://doi.org/10.1063%2F1.4944840.

[42] F. Leroy. "Revisiting the droplet simulation approach to derive force-field parameters for water on molybdenum disulfide from wetting angle measurements". In: *The Journal of Chemical Physics* 145.16 (Oct. 2016), p. 164705. DOI: 10.1063/1.4966215. URL: https://doi.org/10.1063%2F1.4966215.

[43] L. Zhang, B. Luan, and R. Zhou. "Parameterization of Molybdenum Disulfide Interacting with Water Using the Free Energy Perturbation Method". In: *The Journal of Physical Chemistry B* 123.34 (Aug. 2019), pp. 7243–7252. DOI: 10.1021/acs.jpcb.9b02797. URL: https://doi.org/10.1021%2Facs.jpcb.9b02797.

[44] A. T. Sose, E. Mohammadi, P. F. Achari, and S. A. Deshmukh. "Determination of Accurate Interaction Parameters between the Molybdenum Disulfide and Water to Investigate Their Interfacial Properties". In: *The Journal of Physical Chemistry C* 126.4 (Jan. 2022), pp. 2013–2022. DOI: 10.1021/acs.jpcc.1c07313. URL: https://doi.org/10.1021%2Facs.jpcc.1c07313.

[45] Z. Wang, Q. Tu, S. Zheng, J. J. Urban, S. Li, and B. Mi. "Understanding the Aqueous Stability and Filtration Capability of MoS2 Membranes". In: *Nano Letters* 17.12 (Dec. 2017), pp. 7289–7298. DOI: 10.1021/acs.nanolett.7b02804. URL: https://doi.org/10.1021%2Facs.nanolett.7b02804.

[46] M. Asadi, B. Kumar, A. Behranginia, B. A. Rosen, A. Baskin, N. Repnin, D. Pisasale, P. Phillips, W. Zhu, R. Haasch, R. F. Klie, P. Král, J. Abiade, and A. Salehi-Khojin. "Robust carbon dioxide reduction on molybdenum disulphide edges". In: *Nature Communications* 5.1 (2014). DOI: 10.1038/ncomms5470. URL: https://doi.org/10.1038%2Fncomms5470.

[47] P. Abbasi, M. Asadi, C. Liu, S. Sharifi-Asl, B. Sayahpour, A. Behranginia, P. Zapol, R. Shahbazian-Yassar, L. A. Curtiss, and A. Salehi-Khojin. "Tailoring the Edge Structure of Molybdenum Disulfide toward Electrocatalytic Reduction of Carbon Dioxide". In: *ACS Nano* 11.1 (2016), pp. 453–460. DOI: 10.1021/acsnano.6b06392. URL: https://doi.org/10.1021%2Facsnano.6b06392.

[48] M. Asadi, K. Kim, C. Liu, A. V. Addepalli, P. Abbasi, P. Yasaei, P. Phillips, A. Behranginia, J. M. Cerrato, R. Haasch, P. Zapol, B. Kumar, R. F. Klie, J. Abiade, L. A. Curtiss, and A. Salehi-Khojin. "Nanostructured transition metal dichalcogenide electrocatalysts for CO_2 reduction in ionic liquid". In: *Science* 353.6298 (2016), pp. 467–470. DOI:

10.1126/science.aaf4767. URL: https://doi.org/10.1126%2Fscience.aaf4767.

[49] W. Zhou, X. Zou, S. Najmaei, Z. Liu, Y. Shi, J. Kong, J. Lou, P. M. Ajayan, B. I. Yakobson, and J.-C. Idrobo. "Intrinsic Structural Defects in Monolayer Molybdenum Disulfide". In: *Nano Letters* 13.6 (May 2013), pp. 2615–2622. ISSN: 1530-6992. DOI: 10.1021/nl4007479. URL: http://dx.doi.org/10.1021/nl4007479.

[50] S. A. Francis, J. M. Velazquez, I. M. Ferrer, D. A. Torelli, D. Guevarra, M. T. McDowell, K. Sun, X. Zhou, F. H. Saadi, J. John, M. H. Richter, F. P. Hyler, K. M. Papadantonakis, B. S. Brunschwig, and N. S. Lewis. "Reduction of Aqueous CO2 to 1-Propanol at MoS2 Electrodes". In: *Chemistry of Materials* 30.15 (2018), pp. 4902–4908. DOI: 10.1021/acs.chemmater.7b04428. eprint: https://doi.org/10.1021/acs.chemmater.7b04428. URL: https://doi.org/10.1021/acs.chemmater.7b04428.

[51] Y. Xie, X. Li, Y. Wang, B. Li, L. Yang, N. Zhao, M. Liu, X. Wang, Y. Yu, and J.-M. Liu. "Reaction mechanisms for reduction of CO2 to CO on monolayer MoS2". In: *Applied Surface Science* 499 (Jan. 2020), p. 143964. ISSN: 0169-4332. DOI: 10.1016/j.apsusc.2019.143964. URL: http://dx.doi.org/10.1016/j.apsusc.2019.143964.

[52] K. Chan, C. Tsai, H. A. Hansen, and J. K. Nørskov. "Molybdenum Sulfides and Selenides as Possible Electrocatalysts for CO2 Reduction". In: *ChemCatChem* 6.7 (July 2014), pp. 1899–1905. ISSN: 1867-3899. DOI: 10.1002/cctc.201402128. URL: http://dx.doi.org/10.1002/cctc.201402128.

[53] A. A. Peterson and J. K. Nørskov. "Activity Descriptors for CO2 Electroreduction to Methane on Transition-Metal Catalysts". In: *The Journal of Physical Chemistry Letters* 3.2 (Jan. 2012), pp. 251–258. ISSN: 1948-7185. DOI: 10.1021/jz201461p. URL: http://dx.doi.org/10.1021/jz201461p.

3

Effects of alkali metal intercalation on structural and electronic properties of molybdenum disulfide

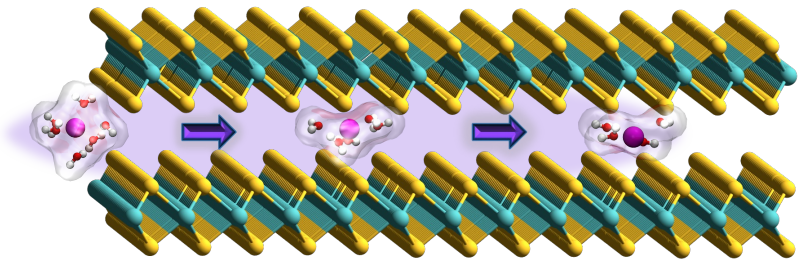

The chapter is based on:
E. Mádai, P.R. Anusuyadevi, P. Gonugunta, A. Mohseni Armaki, J.M.C. Mol, P. Taheri and R.M. Hartkamp, "Effects of alkali metal intercalation on structural and electronic properties of molybdenum disulfide" *Appl.Surf.Sci. 714, 164284*

3.1. Introduction

Meeting today's technological and societal needs relies on advanced materials whose properties can be precisely tailored for high performance and demanding applications. A prominent and widely researched group of advanced materials is the family of 2D materials, due to their superior mechanical, electronic, and structural properties [1]. The high surface-to-bulk ratio of 2D structures enhances their surface functionality, while their layered architecture allows for precise tuning of chemical and electronic properties [2]. These materials find applications across a wide range of fields, including electronics and optoelectronics (e.g., semiconductors, photodetectors), photo- and electrocatalysis (e.g., water purification, electrolyzers for water splitting, CO_2 reduction) [3], energy storage and conversion (e.g., batteries, supercapacitors)[4, 5], and sensing (e.g., gas and biosensors) [6, 7].

2D materials encompass a diverse range of classes, including transition metal dichalcogenides (TMDCs), MXenes, graphene and its derivatives, hexagonal boron nitride (h-BN), and layered metal oxides, each offering distinct structural and electronic properties tailored for various applications [8]. Recently, 2D transition metal borides (MBenes) have also emerged as a promising class of 2D materials, exhibiting notable electrochemical and catalytic properties [9]. As a member of the TMDC family, MoS_2 is an abundant and cost-effective material that offers a tunable chemistry and bandgap, excellent chemical stability, and a layered structure, making it a promising choice for advanced applications [10].

A monolayer of MoS_2 consists of a layer of molybdenum (Mo) atoms sandwiched between two layers of sulfur (S) atoms. These monolayers are held together by van der Waals forces, which then combine to form the bulk material [11]. The three major polytypes of bulk MoS_2 are the metastable 1T-polytype with octahedral structure and exhibiting metallic properties, the 3R- and the 2H-polytypes with trigonal prismatic structure (see Figure A.1) and displaying semiconducting properties [12]. The 2H-polytype MoS_2 is composed of a two-layer stacked unit cell that restores the otherwise broken inversion symmetry of the monolayer MoS_2, while the 3R-polytype consists of a three-layer unit cell, where the inversion symmetry is broken [13] [14].

Due to the broken inversion symmetry in the 3R-polytype, a strong spin-orbit coupling is possible based on the d-orbitals of the transition metals [15]. This provides the opportunity for the development of such applications as electronic and optoelectronic devices[16, 17] and using properties such as valley- and spin-Hall effect and superconductivity [18–20]. The 3R-polytype can be synthesized through chemical vapor deposition and via the mechanical folding and stacking of MoS_2 monolayers [21, 22]. Conversely, the 2H-polytype is the most commonly and naturally available polytype [12]. The applications with this polytype include utilizing bulk or monolayer MoS_2 as (electro-/photo-)catalyst both for hydrogen production

in aqueous media [23–25] and for CO_2 reduction in organic media [26–28]. Furthermore, the 2H-polytype MoS_2 has demonstrated to be a suitable anode material for aqueous rechargeable batteries (ARBs) based on alkali earth metals [29–34], earth metals [35–38], and earth-abundant materials [39–41], as emerging competitors to lithium-ion batteries (LIBs).

As both the 2H- and the 3R-polytypes are semiconducting, the presence of the bandgap presents a challenge, but also an opportunity for tuning the electronic properties. The layered structure of MoS_2 allows the intercalation of (alkali metal) ions, which then donate their valence electrons to the MoS_2 and increase its conductivity and change the bandgap. If the intercalation occurs at high concentrations of intercalants, then a phase transition is induced from the 2H polytype phase to the metastable 1T-polytype phase by the gliding of the monolayers [42]. The intercalation process of different alkali metal ions was studied through various experimental techniques [43, 44]. Wang et al. imaged the intercalation process of Na^+ ions in MoS_2 with aberration-corrected transmission electron microscopy (TEM) and they showed that the MoS_2 structure undergoes complicated phase transitions due to the presence of the Na^+ ions [43]. Attanayake et al. compared the intercalation of Na^+, Ca^{2+}, Co^{2+} and Ni^{2+} ions to MoS_2 based on the efficiency of hydrogen production [45]. The intercalation of K atoms and K^+ ions was studied by Andersen et al., using first-principle calculations [46]. Their calculations showed that the ions together with water molecules can be intercalated into the bulk MoS_2 structure, however, based on measurements by Zak et al. [47] they only added one or two water molecules next to the ions, not a full hydration shell.

Controlling intercalation on the microscale can significantly impact the property changes of the 2D material. However, achieving such control requires a mechanistic understanding of intercalation and the factors that influence it, such as the role of the intercalant and the material and its electronic properties. While the effects of different intercalants have been studied in the literature, a holistic and systematic comparison that links the mechanisms at the atomistic level to changes in material properties at the macroscopic level is still lacking.

The electrochemical intercalation process, where the driving force of the intercalation can be controlled externally, presents a path for this systematic comparison. Hence, this article aims to bridge this gap by shedding new light on the intercalation mechanism influenced by external and internal parameters, such as the applied voltage, and the inherent hydration shell of the alkali metal ions. We use molecular dynamics (MD) simulations to show the microscopic mechanisms of the intercalation, while the macroscopic mechanisms and changes in the material properties are studied experimentally.

3.2. Methods and Materials

3.2.1. Molecular dynamics simulations

All MD simulations were carried out in the Large-scale Atomic/Molecular Massively Parallel Simulator (LAMMPS) simulation package [48] using the DelftBlue supercomputer. For the MoS_2, the REBOMOS potential was used, developed by Jiang et al. [49]; the SPC/E water model was employed to describe the interactions between hydrogen and oxygen atoms in water molecules. The rigid structure of the water molecules was maintained using the SHAKE algorithm. A transferable ion force field, developed by Loche and co-workers [50], was used for KCl and NaCl. Packmol software was used to construct the simulation box. A detailed description of the MD simulations is provided in the Supplementary Information.

3.2.2. Electrode preparation

MoS_2 nanopowder (99% trace metal basis, Sigma Aldrich, for characterization see figures A.7–A.11) was mixed with Carbon Black (CB, Fischer Scientific) and poly(vinyl alcohol) (PVA) was mixed in a ratio of 90 wt%, 5 wt% and 5 wt%, respectively. Once the ingredients are measured and added to a 5 cm^3 vial, the mixture is diluted with 2 mL of Deionized (DI) water, then the ink is sonicated in a water bath for 10 minutes for homogenization. The glassy carbon substrates (1x1 cm, Sigma Aldrich, redox.me) are cleaned with DI water and then sonicated in isopropyl alcohol for 5 minutes, then dried with compressed air. After the sonication of the ink, 25 μL is dropcasted on the glassy carbon substrates, afterwards, the samples are left to dry in air. Afterwards, the electrodes are prepared by connecting a copper tape to the substrate and then it is covered with tape, exposing only a circle of 10 mm in diameter. Then, the intercalation of the two different alkali metal ions (Na^+ and K^+) in the MoS_2 was carried out to enhance its conductivity.

The intercalation of alkali metal ions into MoS_2 is known to induce a phase transition from the semiconducting 2H-phase to the metallic 1T-phase, which is metastable and prone to reversion to the 2H-phase upon thermal treatment or over time [51, 52]. In particular, Li^+ and Na^+ ions can intercalate reversibly and stabilize the 1T-phase to some extent due to their smaller size, while K^+ ions, having a larger atomic radii, cause more pronounced lattice distortion and reduced reversibility [52]. The 1T-phase has been reported to transform back to the thermodynamically stable 2H-phase at temperatures as low as 95 °C [53]. To mitigate such phase relaxation, all sample processing and characterization steps were performed at room temperature or below.

3.2.3. Electrochemical techniques

All electrochemical measurements were carried out on a BioLogic VMP-3e Multichannel Potentiostat with the software EC-Lab. For each measurement the prepared electrode was immersed in 40 mL of 1 mM $KHCO_3$ (Sigma Aldrich, 99.99%) (K^+-intercalation) or 1 mM $NaHCO_3$ (Sigma Aldrich, 99.99%) (Na^+-intercalation) in an electrochemical H-cell. The electrode was placed in the cathode compartment together with a saturated calomel electrode (SCE), while a Pt mesh electrode was put in the anode compartment. All electrodes were then connected to the potentiostat and the whole system was put into a Faradaic cage. For the electrochemical intercalation, first an electrochemical impedance spectroscopy (EIS) was carried out from 1.0 MHz to 100 mHz, then a chronoamperometry (CA) measurement was set on for 1 hour at a preset potential (the effect of potential was studied and an intercalation potential was defined for each ion). Afterwards, the working electrode was rinsed with DI water to remove any potential adsorbed layer and another EIS measurement was carried out to assess the conductivity of the sample.

3.2.4. Scanning Electron Microscopy

Scanning Electron Microscopy was performed using a JEOL IT800SHL system equipped with a field emission gun, operating at 10.00 kV and a beam current of 42.20 nA. Energy Dispersive Spectroscopy (EDS) analysis was conducted with an Oxford Instruments Maxim 100 detector.

3.2.5. XRD

The XRD patterns were measured in a Bruker D8 Advance diffractometer with Bragg-Brentano geometry and Lynxeye position sensitive detector with Cu Kα radiation, divergence slit V12, scatter screen height 5 mm, at 45 kV and at 40 mA. The Detector was set to LL 0.11 W 0.14. The measurement range was set between 5° to 80°, with a step size of 0.03° (in case of the V_S-MoS_2 and K^+-intercalated V_S-MoS_2) and 0.06° (in case of the Na^+-intercalated V_S-MoS_2) with a counting time per step of 2 s.

3.2.6. Raman Spectroscopy

The Raman spectra were obtained using a WiTec Alpha300R Raman Imaging microscope with a 532 nm laser at 1 mW power to prevent sample damage. The integration time was set to 5 seconds with 10 accumulations, and a 63X/0.9 water-dipping objective was used. To ensure high spectral resolution, a 1800 g/mm grating was employed, providing a resolution better than 1 cm^{-1}.

To accurately monitor structural changes induced by intercalation, in situ Raman measurements were performed at the exact same position on the sample surface before and after the electrochemical process. The

sample was mounted in a beaker filled with the electrolyte, which was fixed directly on the Raman stage. The initial (pristine) Raman spectrum was acquired while the sample was immersed in the electrolyte. Following this, the objective was retracted in the Z direction to remove it from the solution, and the electrochemical intercalation process was carried out. After intercalation, the objective was carefully repositioned to the same coordinates (The spatial positioning resolution of the system was approximately 25 nm in XYZ directions, enabling precise repositioning of the measurement spot) and focus depth to acquire the post-intercalation Raman spectrum. This ensured that the layer number and measurement location remained constant, and that any observed spectral changes originated from structural modifications, such as defect formation, rather than sample drift, delamination, or layer number variation.

3.2.7. X-ray Photoelectron Spectroscopy

X-ray photoelectron spectroscopy was carried out in Physical Electronics (PHI) 5400 (Eden Prairie, USA) instrument. The XPS spectra were acquired by using non-monochromatic Al Kα radiation produced from an X-ray source with an Al anode, operating at 200 W and 13.5 kV. The primary photoelectron lines for each element were captured with a step size of 0.1 eV and a dwell time of 1.25 s, employing a spherical capacitor analyzer configured with a pass energy of 71.55 eV. The MultiPak software was used to analyze and process the XPS data, where the acquired peaks were normalized and fitted using the iterated-Shirley background.

3.3. Results and discussions

3.3.1. Electrochemical intercalation

The insertion of Na^+- and K^+-ions into MoS_2 was achieved via electrochemical intercalation by applying a constant potential on the working electrode. Electrochemical impedance spectroscopy (EIS) measurements before and after the intercalation steps are used as an indicator of changes in conductivity, suggesting favorable conditions for intercalation. Figures 3.1 (a) and (b) show the Nyquist plots of unfavorable and favorable conditions, respectively, where Z_0 is the charge transfer resistance belonging to the unexposed electrode and Z is the charge transfer resistance belonging to the electrode which was subjected to chronoamperometry for 1 hour at the respective potentials. The position of Z with respect to Z_0 determines if the potential of the chronoamperometry can be considered as a favorable or unfavorable condition for electrochemical intercalation. In Figure 3.1 (a), a case of unfavorable condition is presented, where it shows that the internal resistance (the sum of the electrolyte resistance and the charge transfer resistance [54]) of the intercalated electrode is higher than the unexposed electrode, namely $Z > Z_0$. On the other hand, Figure

3.1 (b) shows the favorable conditions for intercalation, where the internal resistance of the exposed electrode is smaller than that of the unexposed electrode, namely $Z < Z_0$. This relation indicates favorable conditions for the intercalation, which results in a lower charge transfer resistance and therefore higher conductivity. The data from different measurements at different potentials are collected in Tables A.1 and A.2 for sodium and potassium intercalation, respectively.

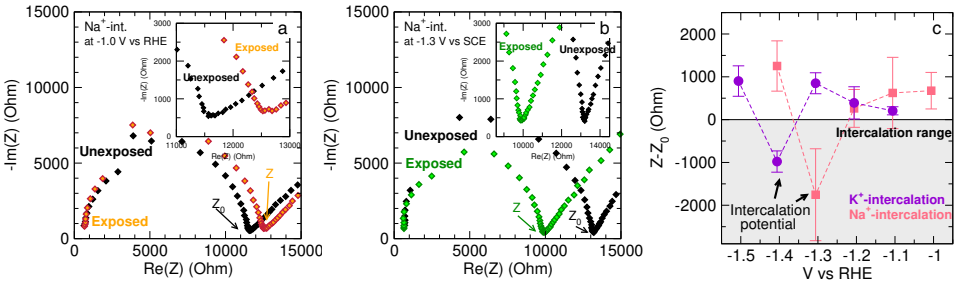

Figure 3.1. Nquist plots for **(a)** unfavorable (-1.0 V vs RHE) and **(b)** favorable (-1.3 V vs RHE) conditions of electrochemical intercalation of sodium ions, **(c)** resistance change at different potentials due to (un)favorable conditions for the electrochemical intercalation of Na^+ and K^+ ions.

Figure 3.1 (c) shows the averaged difference of the measured resistance of the electrode at different applied potentials. A negative difference indicates a drop in the internal resistance of the electrode due to intercalation. Where the $Z\text{-}Z_0$ value is strongly negative, they were labeled as 'intercalation potential' for each ion, namely for potassium -1.4 V vs RHE, for sodium -1.3 V vs RHE, respectively.

3.3.2. MD Simulations

MD simulations with umbrella sampling were used to study the intercalation mechanism of the Na^+ and K^+ ions. A simulation box (19.3 nm × 9.4 nm × 4.4 nm) was created with 18 000 water molecules, 4 MoS_2 sheets, containing 2700 atoms per sheet, and one cation (Na^+ or K^+) with one Cl^- ion for charge neutrality. A description of simulation details and the cross-interaction parameter optimization to reproduce the correct wettability can be found in the Supplementary Information (Tables A.3 and A.4, Figures A.2A.3,A.4A.6).

The intercalation Gibbs free-energy curves are shown in Figure 3.2 (a). The hydration shell of Na^+ and K^+ in bulk water contains approximately 6 and 7 water molecules on average, respectively [55, 56]. Intercalation of these ions into MoS_2 requires the hydration shell to be perturbed, resulting

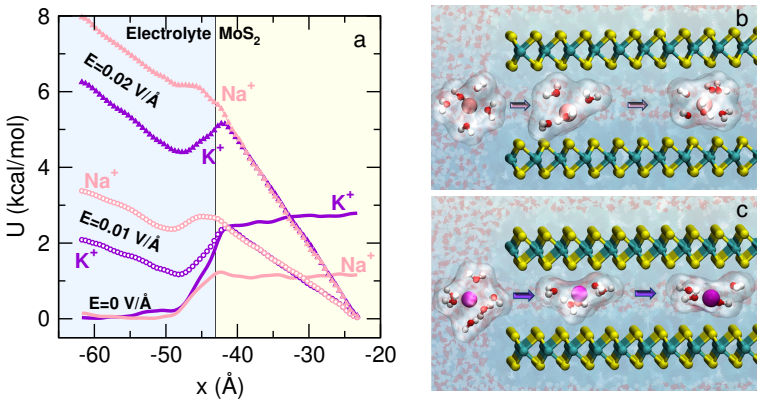

Figure 3.2. **(a)** Gibbs free-energy curves for non-biased (E=0 V/Å) and biased (E=-0.01 V/Å and E=-0.02 V/Å) intercalation. **(b and c)** Merged snapshots from MD simulations of Na^+-intercalation and K^+-intercalation, respectively, showing the deformation of the hydration shells of the ions upon intercalation, (molybdenum atoms are represented with blue color, sulfur atoms are represented with yellow color, sodium ions are represented with pink color, potassium ions are represented with purple color).

in an energy barrier at the edge of the MoS_2. This energy barrier for intercalation is almost twice as high for the K^+ ion as for the Na^+ ion.

If an external electric field is applied to the system, in accordance with our experiments, then a force $F = qE$ acts on each charged atom, where q is the charge and E is the electric field. The external electric field acts as an additional driving force for the ion insertion in the interlayers of the MoS_2. By applying 0.01 V/Å, the intercalation barrier for Na^+ and K^+ ions is lowered by about half with respect to the case without an external field applied. However, the barrier remains larger than the thermal energy $E_{th} = RT \approx 0.59$ kcal/mol, such that intercalation events are not likely to occur on the simulation time scale. At 0.02 V/Å, the intercalation barrier has vanished for Na^+, whereas a barrier remains for K^+.

Figures 3.2 (b and c) present merged snapshots of the MD simulations showing the difference between the disruption of the hydration shells of the two ions. The hydration shell of the Na^+ ion is only perturbed and deformed during the intercalation process, whereas the K^+ ion has to expel at least one water molecule from its shell to fit in the interlayer distance. Furthermore, the remaining shell is still sterically disrupted, hence the higher energy barrier for intercalation. This confirms the trend of the different energy barriers in the Gibbs free-energy profiles in Figure 3.2 (a), which then connects and explains well the higher experimental

intercalation energy for potassium in Figure 3.1 (c).

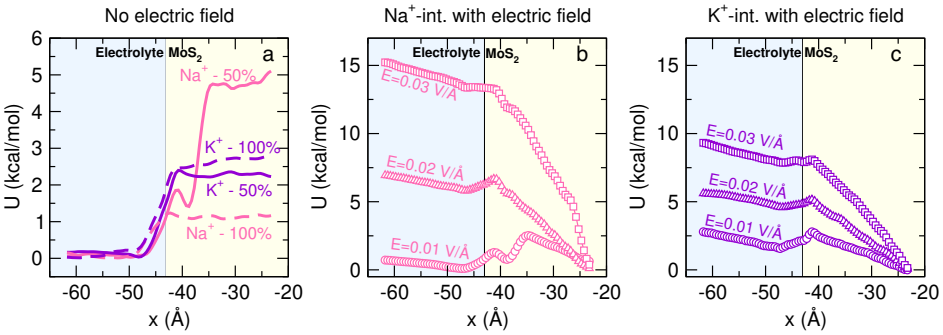

Figure 3.3. **(a)** Gibbs free-energy profiles when no electric field is present, **(b)** and **(c)** Gibbs free-energy profiles of sodium and potassium ions in a geometry of 50% hydrated MoS_2 and different electric fields are present.

These results deviate from the results of Andersen et al. [46], where only two water molecules were included in the hydration shell. Their computations were based on the work by Zak et al. [47] who measured a 50% increase in the vertical lattice parameter and suggested that one or two water molecules per K atom are also intercalated in the MoS_2. To test if their assumption is accurate, we also decreased the hydration of the MoS_2 to 50%, mimicking the 50% vertical lattice parameter increase. The simulation snapshots in Figure A.6 (a) and (c) show the perturbation of the hydration shell upon interaction of the ion. The hydration shell of the ions is more deformed than those in the case of a fully hydrated MoS_2. The hydration shell around both ions adopts a planar configuration containing four water molecules, which exceeds the two water molecules reported by Zak et al. [47]. The Gibbs free-energy curves for these 50% MoS_2 hydration cases in the absence of an externally applied electric field are shown in Figure 3.3 (a). Here, a switch in energy barrier trend can be observed: as the sodium ion has a stronger hydration shell, it presents a larger energy barrier for intercalation compared to the intercalation energy barrier of the potassium ion which stays almost the same as for 100% MoS_2 hydration. Figures 3.3 (b) and (c) show that the intercalation energy barrier of both ions drastically decreases if an external electric field is applied.

3.3.3. Structure analysis

Structural and surface characterization methods are used to study the effect of the electrochemical intercalation on the structural properties of MoS_2. Figure 3.4 (a) shows the XRD patterns of the intercalated and non-intercalated MoS_2. The intensity of the main peak at the (002)

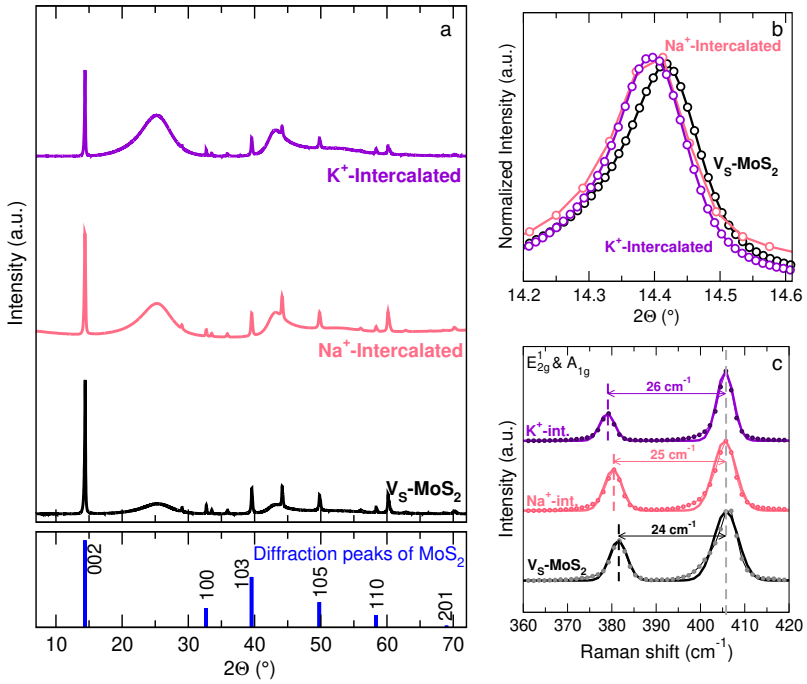

Figure 3.4. **(a)** XRD pattern of V_S-MoS_2, Na^+-intercalated V_S-MoS_2 and K^+-intercalated V_S-MoS_2. **(b)** XRD pattern showing a slight shift in (002) crystal plane orientation of Na^+-intercalated V_S-MoS_2 and K^+-intercalated V_S-MoS_2 with respect to V_S-MoS_2. **(c)** Raman spectra focused on E^1_{2g} and A_{1g} modes. (All spectra were normalized to their respective A_{1g} peak and the plots were stacked for maximum visibility of the shift).

crystal plane orientation for the Na^+-intercalated and K^+-intercalated electrodes weakens with respect to the non-intercalated MoS_2 and a slight broadening can also be observed (Figure 3.4 (b)), which indicates a decrease of the crystallinity as a consequence of the intercalation [43]. Furthermore, this can also indicate irreversible changes in the crystal structure [43]. This slight broadening can better be observed in Figure 3.4 (b), which also shows a slight shift of the peak at the (002) crystal plane orientation to smaller angles, which corresponds to an interlayer expansion due to the intercalation [57].

Raman spectroscopy (Figure 3.4 (c)) was carried out to confirm the presence of vacancies indicated by XRD. Bulk MoS_2 has four characteristic modes in the Raman spectrum E^2_{2g}, E_{1g}, E^1_{2g} and A_{1g}, at ~32 cm^{-1} at ~286 cm^{-1}, at ~384.5 cm^{-1} and at ~405.5 cm^{-1}, respectively [58]. Figure A.8 shows all the mentioned characteristic modes except E^2_{2g}

due to the limitation of low-frequency measurements of the instrument. The peaks appearing between ~430 cm^{-1} and ~470 cm^{-1} are due to the near-the-zone-edge longitudinal and acoustic phonons and their combinations [59]. The two main peaks, E^1_{2g} and A_{1g}, are characteristic of different vibrations of the material: E^1_{2g} is activated by the in-plane vibrations of the Mo and S atoms, while A_{1g} is activated by out-of-plane vibrations of the S atoms[58, 60].

Figure 3.4 (c) shows the E^1_{2g} and A_{1g} modes stacked for intercalated and non-intercalated electrodes. The A_{1g} mode was measured at 405.7 cm^{-1} for all samples, while for the intercalated samples, the E^1_{2g} shows a shift to lower frequencies compared to the non-intercalated electrode. The increased separation between the E^1_{2g} and A_{1g} modes indicates a compressive strain in the MoS_2 structure due to the presence of monosulfur defects [61]. The creation of these monosulfur defects is a consequence of the unused electrode preparation process, hence, this difference in the spectra can also be used for the estimation of the defect concentration in MoS_2 [62, 63]. For a structurally pristine MoS_2, the difference between the E^1_{2g} and A_{1g} peaks is 21 cm^{-1} [58], whereas this value has already increased to 24 cm^{-1} for our MoS_2 electrode. This suggests that monosulfur defects are created in the electrode (from now denoted as V_S-MoS_2) during the sonication step of the sample preparation process. The further blue-shift of the E^1_{2g} peaks of the intercalated samples compared to the V_S-MoS_2 electrode indicates an increased concentration of monosulfur vacancies as a consequence of the intercalation process and confirms our findings in the XRD patterns [61, 64].

3.3.4. XPS analysis

Figure 3.5 (a) shows the Mo 3d XPS spectra of V_S-MoS_2, Na^+-intercalated and K^+-intercalated V_S-MoS_2. The monosulfur vacancies in the MoS_2 structure identified with Raman spectroscopy are also confirmed with the presence of undercoordinated Mo sites (Mo^{UC}) in the Mo 3d spectra [65, 66]. In these fitted Mo 3d5 spectra, the area (Table A.6) of the Mo^{UC} atoms is increased for the intercalated V_S-MoS_2 compared to the V_S-MoS_2. This also correlates with the results from the Raman spectroscopy, as the concentration of these undercoordinated Mo sites in the XPS spectra increases with the same tendency as the concentration of the monosulfur defects increases in the Raman spectra. In all three fits, a small peak at a ~234.5 eV and ~235.5 eV can be observed, which corresponds to the oxidation state of Mo^{6+} in MoO_3, which can be present due to the exposure to air and water in the ink during the sample preparation process and in the electrolyte during the electrochemical intercalation [44, 67].

For V_S-MoS_2, the two main peaks, Mo 3d 1/2 and 3/2 for the V_S-MoS_2 are located at 229.1 eV and 232.4 eV, respectively, which agree with

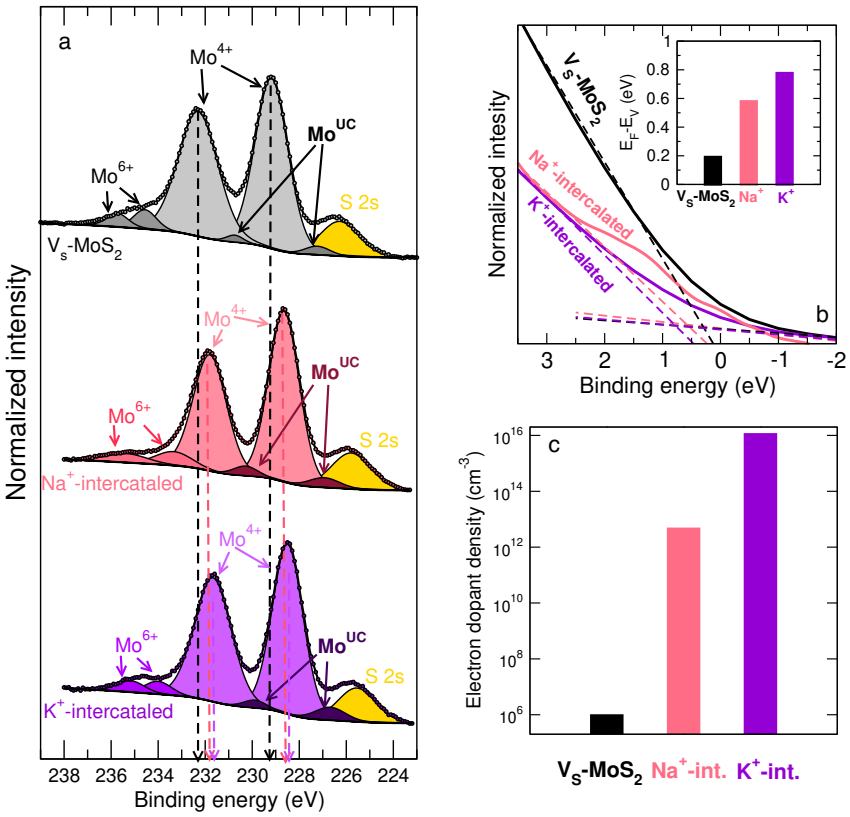

Figure 3.5. **(a)** Fitting of normalized Mo 3d XPS spectra of V_S-MoS_2, Na^+-intercalated V_S-MoS_2 and K^+-intercalated V_S-MoS_2, respectively, the spectra of the intercalated V_S-MoS_2 compared to V_S-MoS_2 spectrum showing a down-shift in binding energy. **(b)** Linear fitting of valence band spectra to determine E_F-E_V (shown in inset). **(c)** Calculated electron doping density of pristine, Na^+-intercalated and K^+-intercalated V_S-MoS_2 based on valence band spectra showing the amount of electron dopants for each electrode.

the literature values [43, 68]. Figure 3.5 (a) also shows the shift in the binding energy for the intercalated V_S-MoS_2 electrodes with respect to the V_S-MoS_2 electrode. However, these peaks are down-shifted for the Na^+-intercalated and K^+-intercalated V_S-MoS_2 by 0.5 eV and 0.7 eV, respectively, which indicates the presence of excess electrons compared to the V_S-MoS_2. This also suggests that electrons were donated from the intercalants (Na^+ and K^+ ions) to the V_S-MoS_2 [43]. The same downshift in energy was observed for the S 2p3 spectra of the three materials (see

Figure A.10 (a)).

The degree of alkali metal intercalation into V_S-MoS_2 was estimated based on the observed binding energy shifts in the XPS spectra. Specifically, shifts of 0.6 eV for K^+ and 0.5 eV for Na^+ in the Mo 3d core level suggest a significant level of intercalation. Comparing our results to literature benchmarks, these chemical shifts correspond to intercalation levels of approximately $x \approx 0.3$–0.5 in A_xMoS_2 [69–71]. These levels are known to induce measurable structural and electronic changes, supporting the observed modifications in our system.

To study the effect of the intercalation on the electronic structure of the V_S-MoS_2 further, Figures 3.5 (b) and (c) assess the effect of intercalation on the valence band, hence, high-resolution XPS measurements were taken from 20 eV to -15 eV. The value of the bandgap can be changed through intercalation of alkali metal ions and, consequently, electron doping [46]. The intercalation of the alkali metal ions changes the slope of the spectra and, hence, changes the energy level difference between the Fermi level and the valence band (E_F-E_V). With a linear extrapolation to the valence band tail (near 0 eV binding energy) in the XPS spectra, the value of E_F-E_V was determined, where E_F is the Fermi level energy and E_V is the valence band energy, respectively [72].

The high electron dopant density for the Na^+-intercalated and K^+-intercalated V_S-MoS_2 is a consequence of the synergy between the sulfur defects and donated s-electrons of the alkali metal ions. The change in the electronic properties of lithiated and sodiated defective MoS_2 has already been investigated with density functional theory (DFT) by Barik et al. [73]. According to the DFT calculations, the sulfur defects create a midgap state and reduce the bandgap significantly. The adsorption of the intercalants (lithium and sodium in their case) is enhanced as the midgap state coming from the d-orbital of the Mo atom and the s-orbital of the alkali metal atom forms a strong hybridization. This results in an enhanced conductivity and changes the semiconducting nature of the defective MoS_2 to metallic with the lithiation/sodiation. Our experimental results correlate well with these calculations in the case of the Na^+-intercalated V_S-MoS_2. However, for the K^+-intercalated V_S-MoS_2 the electron dopant density is even higher, which can be due to the presence of potassium's empty *d*-orbital. The separation of light (Li^+ and Na^+) and heavy alkali metal ions (K^+, Rb^+ and Cs^+) are based on the presence of this empty *d*-orbital, as it gives the possibility of further hybridization between the heavy alkali metal's *d*-orbital and the transition metal's *p*-orbital. This hybridization and the charge transfer then create a low work function due to a larger dipole moment than for light alkali metals [74]. This behavior is similar to what Yu et al. found with regards to the intercalation of sodium and potassium ions in Cu_4Se_4 [75, 76]. Intercalation of alkali-metal ions into Cu_4Se_4 nanosheets induces a surface phase transition, with K^+ intercalation occurring at a higher voltage (0.756 V) than Na^+ (0.659

V), indicative of stronger charge transfer[75]. This stronger interaction leads to a larger surface dipole and therefore a more pronounced decrease in work function for K^+-intercalated Cu_4Se_4 compared to the Na^+-intercalated counterpart [75].

3.3.5. Electrochemical CO_2 reduction

MoS_2 is a well-known electrocatalyst for HER, tends to suppress the competing CO_2RR. Hence, either the surface of the catalyst has to be modified to change this tendency and suppress HER and promote CO_2RR, or the environment it is exposed to. Ab initio Molecular Dynamics simulations showed that by using the mixture of water and [EMIM][BF_4], the activated the CO_2 molecule can form a complex with the $[EMIM]^+$ and this complex can physisorb on the surface of the MoS_2 [77]. This process provides a direct CO_2 feedstock for the catalyst. Building on the results of Asadi et al., non-intercalated V_S-MoS_2 and the intercalated V_S-MoS_2 electrodes were exposed to the mixture of 4 mol% [EMIM][BF_4] and 96 mol% water.

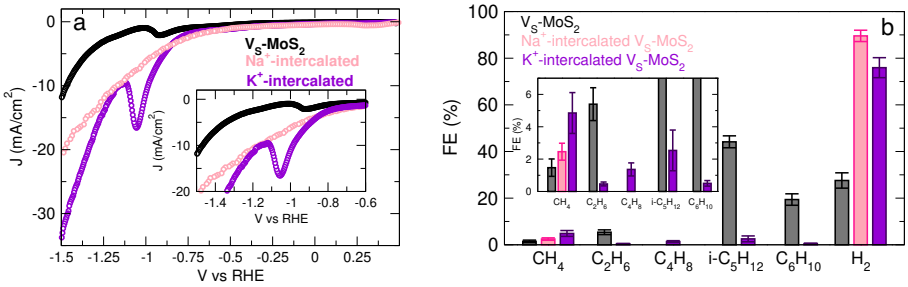

Figure 3.6. **(a)** LSV curves in IL-water mixture for non-intercalated V_S-MoS_2 and intercalated V_S-MoS_2 catalysts. **(b)** Faradaic efficiencies of non-intercalated V_S-MoS_2 and intercalated V_S-MoS_2 catalysts.

Figure 3.6 (a) shows the linear sweep voltammetry curves of the three electrodes in the CO_2-saturated IL-water mixture. The three electrodes show a trend in the current density. The lowest current density was measured for the V_S-MoS_2, then the Na^+-intercalated V_S-MoS_2 shows already significantly higher current density reaching more than -20 mA/cm^2 at -1.5 V vs RHE. The highest current density can be assigned to the K^+-intercalated V_S-MoS_2, where the it reaches -35 mA/cm^2 at -1.5 V vs RHE. This trend in the conductivity agrees well with the electron dopant concentration in figure 3.5 (c). Two of the three LSV curves show furthermore reduction wells in Figure 3.6. The V_S-MoS_2 shows a smaller reduction well at -0.85 V vs RHE, while the K^+-intercalated V_S-MoS_2 shows

deep reduction well at -1.05 V vs RHE, whereas Na^+-intercalated V_S-MoS_2 does not show any.

Therefore, chronoamperometry measurements were conducted at these specific voltages of the respective reduction wells, the gaseous products were collected at distinct time intervals and the components were identified by gas chromatography. In the product analysis, the V_S-MoS_2 and the K^+-intercalated V_S-MoS_2 electrocatalysts showed activity towards the CO_2RR and different yields of multicarbon products. While in the case of the Na^+-intercalated V_S-MoS_2 there was only very little amount of H_2 measured and no other products at the voltage of -1.0 V vs RHE. The lack of carbon-based products can be attributed to the instability of the Na^+-intercalation in MoS_2. In a non-intercalated V_S-MoS_2, as it was shown by our MD simulations, the Na^+ ion can only follow a 2D path, meaning the ion intercalates from the edges into the bulk. However, in a V_S-MoS_2, the Na^+ ion is capable to a 3D diffusion, due to its smaller size than a K^+ ion, and it can diffuse through the vacancies of the MoS_2 which was observed previously by Yao et al. [78]. Hence, it is possible that the V_S-MoS_2 lets the Na^+ ions escape through the sulfur vacancies which potentially renders the system to an inactive state.

Figure 3.6 (b) shows the Faradaic efficiency of the CO_2 reduction reaction on the three electrodes. For the non-intercalated V_S-MoS_2, the main product with 44% FE of the CO_2RR is isopentane, hexyne was found with a FE of 19%, methane and ethane were found in small quantities also. Comparing these results to the findings of Asadi et al., where CVD-grown monolayers were exposed to the same IL-water mixture and the main and only product of the CO_2RR was CO, our results confirm the theory of the production of multicarbon species due to the presence of sulfur vacancies by Kang et al. [79]. In the case of the K^+-intercalated V_S-MoS_2 electrode, the FE of H_2 is more than double compared to hydrogen production on the non-intercalated V_S-MoS_2. Furthermore, the inset shows that the selectivity of the catalyst changed with regards to the multicarbon products: isobutane appears among the products.

The presented FE results show that (1) the non-intercalated V_S-MoS_2 the presence of sulfur vacancies lead to five different multicarbon products in the CO_2RR. (2) The potential instability of the Na^+-intercalation renders the electrocatalytic system inactive with regards to CO_2RR and shows activity only towards the HER. (3) The K^+-intercalated V_S-MoS_2 shows a different selectivity of the CO_2RR and still favors the HER even in an environment which supports the CO_2RR.

3.4. Conclusions

In this chapter, we have studied the intercalation mechanisms of Na^+ and K^+ ions into MoS_2 and their effect on the structural and electronic properties of the host material. We have found that the intercalation

energy strongly depends on the perturbed hydration shell of the alkali metal ion in an aqueous environment at the interface with the MoS_2. Furthermore, we have shown that the intercalation process increases the concentration of monosulfur defects in the MoS_2 structure. However, the presence of these defects and the donated electrons from the alkali metal ions have a synergistic effect on the electronic material properties, resulting in increased conductivity. The difference between the level of electron dopant density with regard to light and heavy alkali metal ions can be attributed to the presence of the empty orbitals, which allow further hybridization. These results also have shown that MoS_2 is a highly tunable material regarding not only its structural properties, regarding its flexibility in the vertical dimension, but also its electronic properties through changing the valance band structure; and that the structure engineered on the atomic scale has a large influence on the macroscopic properties.

references

[1] M. Akhtar, G. Anderson, R. Zhao, A. Alruqi, J. E. Mroczkowska, G. Sumanasekera, and J. B. Jasinski. "Recent advances in synthesis, properties, and applications of phosphorene". In: *npj 2D Materials and Applications* 1.1 (2017), p. 5. DOI: 10.1038/s41699-017-0007-5.

[2] P. R. Anusuyadevi, S. Pranavi, R. N. R. Shaw, **E. Mádai**, D. J. P. Kumar, P. Gonugunta, P. Taheri, and A. Mol. "An Overview of Emerging 2D Nanomaterials: General Synthesis Methods and Properties". In: *Next-generation 2D Nanomaterials for Sustainable Energy and Environment-oriented Applications: Electrocatalysis, Photoelectrocatalysis and Photocatalysis*. Royal Society of Chemistry, 2025. ISBN: 978-1-83767-381-0.

[3] L. Zhang, K. Liu, Z. Chen, and Y. Wang. "Advances in 2D Materials for Catalytic Applications: A Review". In: *Journal of Colloid and Interface Science* 695 (2025), p. 137799. DOI: 10.1016/j.jcis.2023.137799.

[4] B. Radisavljevic, A. Radenovic, J. Brivio, V. Giacometti, and A. Kis. "Single-layer MoS_2 transistors". In: *Nature Nanotechnology* 6.3 (2011), pp. 147–150. DOI: 10.1038/nnano.2010.279.

[5] H. Liu, L. Zhao, T. Zhang, and J. Li. "Recent progress of 2D materials in energy storage and conversion". In: *Applied Surface Science* 546 (2021), p. 149062. DOI: 10.1016/j.apsusc.2021.149062.

[6] J. Z. Hassan, A. Raza, Z. U. Din Babar, U. Qumar, N. T. Kaner, and A. Cassinese. "2D material-based sensing devices: an update". In: *Journal of Materials Chemistry A* 11.12 (2023), pp. 6016–6063. ISSN: 2050-7496. DOI: 10.1039/d2ta07653e.

[7] F. Zhang, C. Li, Z. Li, L. Dong, and J. Zhao. "Recent progress in three-terminal artificial synapses based on 2D materials: from mechanisms to applications". In: *Microsystems & Nanoengineering* 9.1 (2023), p. 16. DOI: 10.1038/s41378-023-00487-2.

[8] Y.-C. Lin, R. Torsi, R. Younas, C. L. Hinkle, A. F. Rigosi, H. M. Hill, K. Zhang, S. Huang, C. E. Shuck, C. Chen, Y.-H. Lin, D. Maldonado-Lopez, J. L. Mendoza-Cortes, J. Ferrier, S. Kar, N. Nayir, S. Rajabpour, A. C. T. van Duin, X. Liu, D. Jariwala, J. Jiang, J. Shi, W. Mortelmans, R. Jaramillo, J. M. J. Lopes, R. Engel-Herbert, A. Trofe, T. Ignatova, S. H. Lee, Z. Mao, L. Damian, Y. Wang, M. A. Steves, K. L. J. Knappenberger, Z. Wang, S. Law, G. Bepete, D. Zhou, J.-X. Lin, M. S. Scheurer, J. Li, P. Wang, G. Yu, S. Wu, D. Akinwande, J. M. Redwing, M. Terrones, and

J. A. Robinson. "Recent Advances in 2D Material Theory, Synthesis, Properties, and Applications". In: *ACS Nano* 17.11 (2023). PMID: 37219929, pp. 9694–9747. DOI: 10.1021/acsnano.2c12759.

[9] Z.-H. Wu and Y.-X. Yu. "Theoretical study on catalytic performance of Ti_2B monolayer as cathodes of Li–O_2 and Na–O_2 batteries promoted by surface functionalization". In: *Applied Surface Science* 666 (2024), p. 160380. DOI: 10.1016/j.apsusc.2024.160380.

[10] S. Joseph, J. Mohan, S. Lakshmy, S. Thomas, B. Chakraborty, S. Thomas, and N. Kalarikkal. "A review of the synthesis, properties, and applications of 2D transition metal dichalcogenides and their heterostructures". In: *Materials Chemistry and Physics* 297 (2023), p. 127332. ISSN: 0254-0584. DOI: 10.1016/j.matchemphys.2023.127332.

[11] L. F. Mattheiss. "Band Structures of Transition-Metal-Dichalcogenide Layer Compounds". In: *Physical Review B* 8.8 (1973), pp. 3719–3740. ISSN: 0556-2805. DOI: 10.1103/physrevb.8.3719.

[12] J. Wilson and A. Yoffe. "The transition metal dichalcogenides discussion and interpretation of the observed optical, electrical and structural properties". In: *Advances in Physics* 18.73 (1969), pp. 193–335. ISSN: 1460-6976. DOI: 10.1080/00018736900101307.

[13] X. Fan, W.-T. Zheng, J.-L. Kuo, D. J. Singh, C.-W. Sun, and W. Zhu. "Modulation of electronic properties from stacking orders and spin-orbit coupling for 3R-type MoS_2". In: *Scientific Reports* 6.24140 (2016). DOI: 10.1038/srep24140.

[14] S. Thomas, S. Moolayadukkam, and K. P. Priyanka. "Structural, Mechanical, and Electronic Properties of In-Plane 1T/2H-MoS_2, 2H-MoS_2, and 3R-MoS_2". In: *Structural, Mechanical, and Electronic Properties of In-Plane 1T/2H-MoS_2, 2H-MoS_2, and 3R-MoS_2*. Singapore: Springer Nature Singapore, 2024. DOI: 10.1007/978-981-97-7367-1_5.

[15] W. Feng, Y. Yao, W. Zhu, J. Zhou, W. Yao, and D. Xiao. "Intrinsic spin Hall effect in monolayers of group-VI dichalcogenides: A first-principles study". In: *Physical Review B* 86.16 (2012), p. 165108. DOI: 10.1103/PhysRevB.86.165108.

[16] Q. H. Wang, K. Kalantar-Zadeh, A. Kis, J. N. Coleman, and M. S. Strano. "Electronics and optoelectronics of two-dimensional transition metal dichalcogenides". In: *Nature Nanotechnology* 7.11 (2012), pp. 699–712. ISSN: 1748-3395. DOI: 10.1038/nnano.2012.193.

[17] B. Radisavljevic, A. Radenovic, J. Brivio, V. Giacometti, and A. Kis. "Single-layer MoS_2 transistors". In: *Nature Nanotechnology* 6.3 (2011), pp. 147–150. ISSN: 1748-3395. DOI: 10.1038/nnano.2010.279.

[18] Z. Y. Zhu, Y. C. Cheng, and U. Schwingenschlögl. "Giant spin-orbit-induced spin splitting in two-dimensional transition-metal dichalcogenide semiconductors". In: *Physical Review B* 84.15 (2011), p. 153402. ISSN: 1550-235X. DOI: 10.1103/physrevb.84.153402.

[19] H. Zeng, J. Dai, W. Yao, D. Xiao, and X. Cui. "Valley polarization in MoS_2 monolayers by optical pumping". In: *Nature Nanotechnology* 7.8 (2012), pp. 490–493. ISSN: 1748-3395. DOI: 10.1038/nnano.2012.95.

[20] R. Roldán, E. Cappelluti, and F. Guinea. "Interactions and superconductivity in heavily doped MoS_2". In: *Phys. Rev. B* 88 (5 2013), p. 054515. DOI: 10.1103/PhysRevB.88.054515.

[21] R. Suzuki, M. Sakano, Y. J. Zhang, R. Akashi, D. Morikawa, A. Harasawa, K. Yaji, K. Kuroda, K. Miyamoto, T. Okuda, K. Ishizaka, R. Arita, and Y. Iwasa. "Valley-dependent spin polarization in bulk MoS_2 with broken inversion symmetry". In: *Nature Nanotechnology* 9.8 (2014), pp. 611–617. ISSN: 1748-3395. DOI: 10.1038/nnano.2014.148.

[22] K. Liu, L. Zhang, T. Cao, C. Jin, D. Qiu, Q. Zhou, A. Zettl, P. Yang, S. G. Louie, and F. Wang. "Evolution of interlayer coupling in twisted molybdenum disulfide bilayers". In: *Nature Communications* 5.1 (2014), p. 4966. ISSN: 2041-1723. DOI: 10.1038/ncomms5966.

[23] H. Wang, X. Xiao, S. Liu, C.-L. Chiang, X. Kuai, C.-K. Peng, Y.-C. Lin, X. Meng, J. Zhao, J. Choi, Y.-G. Lin, J.-M. Lee, and L. Gao. "Structural and Electronic Optimization of MoS2 Edges for Hydrogen Evolution". In: *Journal of the American Chemical Society* 141.46 (2019). PMID: 31692351, pp. 18578–18584. DOI: 10.1021/jacs.9b09932. URL: https://doi.org/10.1021/jacs.9b09932.

[24] Y. Shi, Y. Zhou, D.-R. Yang, W.-X. Xu, C. Wang, F.-B. Wang, J.-J. Xu, X.-H. Xia, and H.-Y. Chen. "Energy Level Engineering of MoS2 by Transition-Metal Doping for Accelerating Hydrogen Evolution Reaction". In: *Journal of the American Chemical Society* 139.43 (Oct. 2017), pp. 15479–15485. ISSN: 1520-5126. DOI: 10.1021/jacs.7b08881. URL: http://dx.doi.org/10.1021/jacs.7b08881.

[25] Y. Yu, S.-Y. Huang, Y. Li, S. N. Steinmann, W. Yang, and L. Cao. "Layer-Dependent Electrocatalysis of MoS2 for Hydrogen Evolution". In: *Nano Letters* 14.2 (2014). PMID: 24397410, pp. 553–558. DOI: 10.1021/nl403620g. URL: https://doi.org/10.1021/nl403620g.

[26] P. Abbasi, M. Asadi, C. Liu, S. Sharifi-Asl, B. Sayahpour, A. Behranginia, P. Zapol, R. Shahbazian-Yassar, L. A. Curtiss, and A. Salehi-Khojin. "Tailoring the Edge Structure of Molybdenum Disulfide toward Electrocatalytic Reduction of Carbon Dioxide". In: *ACS Nano* 11.1 (2016), pp. 453–460. DOI: 10.1021/acsnano.6b06392. URL: https://doi.org/10.1021%2Facsnano.6b06392.

[27] M. Asadi, B. Kumar, A. Behranginia, B. A. Rosen, A. Baskin, N. Repnin, D. Pisasale, P. Phillips, W. Zhu, R. Haasch, *et al.* "Robust carbon dioxide reduction on molybdenum disulphide edges". In: *Nature communications* 5.1 (2014), p. 4470.

[28] M. Asadi, K. Kim, C. Liu, A. V. Addepalli, P. Abbasi, P. Yasaei, P. Phillips, A. Behranginia, J. M. Cerrato, R. Haasch, P. Zapol, B. Kumar, R. F. Klie, J. Abiade, L. A. Curtiss, and A. Salehi-Khojin. "Nanostructured transition metal dichalcogenide electrocatalysts for CO_2 reduction in ionic liquid". In: *Science* 353.6298 (2016), pp. 467–470. DOI: 10.1126/science.aaf4767. URL: https://doi.org/10.1126%2Fscience.aaf4767.

[29] L. Chen, Z. Chen, L. Chen, P. Zhou, J. Wang, H. Yang, Z. Feng, X. Li, and J. Huang. "The exfoliation of bulk MoS2 by a three-roller mill for high-performance potassium ion batteries". In: *Applied Surface Science* 615 (Apr. 2023), p. 156253. DOI: 10.1016/j.apsusc.2022.156253. URL: https://doi.org/10.1016%2Fj.apsusc.2022.156253.

[30] J. Li, F. Hu, H. Wei, J. Hei, Y. Yin, G. Liu, N. Wang, and H. Wei. "Confining MoS2/C nanoparticles on two-dimensional graphene sheets for high reversible capacity and long-life potassium ions batteries". In: *Composites Part B: Engineering* 250 (Feb. 2023), p. 110424. DOI: 10.1016/j.compositesb.2022.110424. URL: https://doi.org/10.1016%2Fj.compositesb.2022.110424.

[31] J. Zheng, F. Xiao, H. Jin, C. Cao, Z. Lei, Y. Wang, M. Wei, Q. Qian, L. Zeng, and Q. Chen. "Facile fabrication of MoS2 nanocrystals confined in waste leather derived N, P co-doped carbon fiber for long-lifespan of sodium/potassium ion batteries". In: *Journal of Physics and Chemistry of Solids* 172 (Jan. 2023), p. 111080. DOI: 10.1016/j.jpcs.2022.111080. URL: https://doi.org/10.1016%2Fj.jpcs.2022.111080.

[32] J. Huang, Y. Yao, M. Huang, Y. Zhang, Y. Xie, M. Li, L. Yang, X. Wei, and Z. Li. "Creating Unidirectional Fast Ion Diffusion Channels in G/NiS2-MoS2 Heterostructures for High-Performance Sodium-Ion Batteries". In: *Small* 18.18 (Apr. 2022), p. 2200782. DOI: 10.1002/smll.202200782. URL: https://doi.org/10.1002%2Fsmll.202200782.

[33] E. V. Sukhanova, L. A. Bereznikova, A. M. Manakhov, H. S. A. Qahtani, and Z. I. Popov. "A Novel Membrane-like 2D A'-MoS2 as Anode for Lithium- and Sodium-Ion Batteries". In: *Membranes* 12.11 (Nov. 2022), p. 1156. DOI: 10.3390/membranes12111156. URL: https://doi.org/10.3390%2Fmembranes12111156.

[34] H. Zhang, J. Song, J. Li, J. Feng, Y. Ma, L. Ma, H. Liu, Y. Qin, X. Zhao, and F. Wang. "Interlayer-Expanded MoS2 Nanoflowers Vertically Aligned on MXene@Dual-Phased TiO2 as High-Performance Anode for Sodium-Ion Batteries". In: *ACS Applied Materials andInterfaces*

14.14 (Apr. 2022), pp. 16300–16309. DOI: 10.1021/acsami.2c02080. URL: https://doi.org/10.1021%2Facsami.2c02080.

[35] X. Fan, M. Tebyetekerwa, Y. Wu, R. R. Gaddam, and X. S. Zhao. "Magnesium/Lithium Hybrid Batteries Based on SnS2-MoS2with Reversible Conversion Reactions". In: *Energy Material Advances* 2022 (Jan. 2022). DOI: 10.34133/2022/9846797. URL: https://doi.org/10.34133%2F2022%2F9846797.

[36] M. Shao, H. Sheng, L. Lin, H. Ma, Q. Wang, J. Yuan, X. Zhang, G. Chen, W. Li, Q. Su, E. Xie, J. Wang, Z. Zhang, and W. Lan. "High-Performance Biodegradable Energy Storage Devices Enabled by Heterostructured MoO3 –MoS2 Composites". In: *Small* 19.10 (Dec. 2022), p. 2205529. DOI: 10.1002/smll.202205529. URL: https://doi.org/10.1002%2Fsmll.202205529.

[37] M. Wang, H. Ye, V. Vasudevan, and N. V. Medhekar. "Enhancing kinetic and electrochemical performance of layered MoS2 cathodes with interlayer expansion for Mg-ion batteries". In: *Journal of Power Sources* 542 (Sept. 2022), p. 231722. DOI: 10.1016/j.jpowsour.2022.231722. URL: https://doi.org/10.1016%2Fj.jpowsour.2022.231722.

[38] J. B. D. Linganay and D. B. Putungan. "Adsorption and diffusion properties of calcium ions at the van der Waals interface of NbSe2-graphene 2D heterostructure for multivalent battery applications: density functional theory calculations". In: *Materials Research Express* 9.9 (Sept. 2022), p. 095506. DOI: 10.1088/2053-1591/ac92c8. URL: https://doi.org/10.1088%2F2053-1591%2Fac92c8.

[39] H. Liang, Z. Cao, F. Ming, W. Zhang, D. H. Anjum, Y. Cui, L. Cavallo, and H. N. Alshareef. "Aqueous Zinc-Ion Storage in MoS2 by Tuning the Intercalation Energy". In: *Nano Letters* 19.5 (Apr. 2019), pp. 3199–3206. DOI: 10.1021/acs.nanolett.9b00697. URL: https://doi.org/10.1021%2Facs.nanolett.9b00697.

[40] J. Liu, P. Xu, J. Liang, H. Liu, W. Peng, Y. Li, F. Zhang, and X. Fan. "Boosting aqueous zinc-ion storage in MoS2 via controllable phase". In: *Chemical Engineering Journal* 389 (June 2020), p. 124405. DOI: 10.1016/j.cej.2020.124405. URL: https://doi.org/10.1016%2Fj.cej.2020.124405.

[41] Z. Yao, W. Zhang, X. Ren, Y. Yin, Y. Zhao, Z. Ren, Y. Sun, Q. Lei, J. Wang, L. Wang, T. Ji, P. Huai, W. Wen, X. Li, D. Zhu, and R. Tai. "A Volume Self-Regulation MoS2 Superstructure Cathode for Stable and High Mass-Loaded Zn-Ion Storage". In: *ACS Nano* 16.8 (Aug. 2022), pp. 12095–12106. DOI: 10.1021/acsnano.2c02330. URL: https://doi.org/10.1021%2Facsnano.2c02330.

[42] Z. Wang, Q. Tu, S. Zheng, J. J. Urban, S. Li, and B. Mi. "Understanding the Aqueous Stability and Filtration Capability of MoS2 Membranes". In: *Nano Letters* 17.12 (Dec. 2017), pp. 7289–7298. ISSN: 1530-6992. DOI: 10.1021/acs.nanolett.7b02804. URL: http://dx.doi.org/10.1021/acs.nanolett.7b02804.

[43] X. Wang, X. Shen, Z. Wang, R. Yu, and L. Chen. "Atomic-Scale Clarification of Structural Transition of MoS2 upon Sodium Intercalation". In: *ACS Nano* 8.11 (Nov. 2014), pp. 11394–11400. ISSN: 1936-086X. DOI: 10.1021/nn505501v. URL: http://dx.doi.org/10.1021/nn505501v.

[44] G. Wang, Y. Zhang, H. S. Cho, X. Zhao, F. Kim, and J. Zou. "Revisiting the Structural Evolution of MoS2 During Alkali Metal (Li, Na, and K) Intercalation". In: *ACS Applied Energy Materials* 4.12 (Nov. 2021), pp. 14180–14190. ISSN: 2574-0962. DOI: 10.1021/acsaem.1c02937. URL: http://dx.doi.org/10.1021/acsaem.1c02937.

[45] N. H. Attanayake, A. C. Thenuwara, A. Patra, Y. V. Aulin, T. M. Tran, H. Chakraborty, E. Borguet, M. L. Klein, J. P. Perdew, and D. R. Strongin. "Effect of Intercalated Metals on the Electrocatalytic Activity of 1T-MoS_2 for the Hydrogen Evolution Reaction". In: *ACS Energy Letters* 3.1 (2017), pp. 7–13. DOI: 10.1021/acsenergylett.7b00865. URL: https://doi.org/10.1021%2Facsenergylett.7b00865.

[46] A. Andersen, S. M. Kathmann, M. A. Lilga, K. O. Albrecht, R. T. Hallen, and D. Mei. "First-Principles Characterization of Potassium Intercalation in Hexagonal 2H-MoS_2". In: *The Journal of Physical Chemistry C* 116.2 (2012), pp. 1826–1832. DOI: 10.1021/jp206555b. URL: https://doi.org/10.1021%2Fjp206555b.

[47] A. Zak, Y. Feldman, V. Lyakhovitskaya, G. Leitus, R. Popovitz-Biro, E. Wachtel, H. Cohen, S. Reich, and R. Tenne. "Alkali Metal Intercalated Fullerene-Like MS2 (M = W, Mo) Nanoparticles and Their Properties". In: *Journal of the American Chemical Society* 124.17 (2002), pp. 4747–4758. ISSN: 1520-5126. DOI: 10.1021/ja012060q.

[48] A. P. Thompson, H. M. Aktulga, R. Berger, D. S. Bolintineanu, W. M. Brown, P. S. Crozier, P. J. in 't Veld, A. Kohlmeyer, S. G. Moore, T. D. Nguyen, R. Shan, M. J. Stevens, J. Tranchida, C. Trott, and S. J. Plimpton. "LAMMPS - a flexible simulation tool for particle-based materials modeling at the atomic, meso, and continuum scales". In: *Computer Physics Communications* 271 (Feb. 2022), p. 108171. DOI: 10.1016/j.cpc.2021.108171. URL: https://doi.org/10.1016%2Fj.cpc.2021.108171.

[49] J.-W. Jiang, H. S. Park, and T. Rabczuk. "Molecular dynamics simulations of single-layer molybdenum disulphide (MoS2): Stillinger-Weber parametrization, mechanical properties, and thermal conductivity".

In: *Journal of Applied Physics* 114.6 (Aug. 2013), p. 064307. DOI: 10.1063/1.4818414. URL: https://doi.org/10.1063%2F1.4818414.

[50] P. Loche, P. Steinbrunner, S. Friedowitz, R. R. Netz, and D. J. Bonthuis. "Transferable Ion Force Fields in Water from a Simultaneous Optimization of Ion Solvation and Ion–Ion Interaction". In: *The Journal of Physical Chemistry B* 125.30 (July 2021), pp. 8581–8587. DOI: 10.1021/acs.jpcb.1c05303. URL: https://doi.org/10.1021%2Facs.jpcb.1c05303.

[51] K. E. Dungey, M. D. Curtis, and J. E. Penner-Hahn. "Structural Characterization and Thermal Stability of MoS2 Intercalation Compounds". In: *Chemistry of Materials* 10.8 (1998), pp. 2152–2161. DOI: 10.1021/cm9800341.

[52] J. Zhang, A. Yang, X. Wu, and et al. "Reversible and selective ion intercalation through the top surface of few-layer MoS2". In: *Nature Communications* 9 (2018), p. 5289. DOI: 10.1038/s41467-018-07710-z.

[53] A. N. Enyashin and G. Seifert. "New Route for Stabilization of 1T-WS2 and MoS2 Phases". In: *The Journal of Physical Chemistry C* 115.50 (2011), pp. 24586–24591. DOI: 10.1021/jp2076325.

[54] B.-A. Mei, O. Munteshari, J. Lau, B. Dunn, and L. Pilon. "Physical Interpretations of Nyquist Plots for EDLC Electrodes and Devices". In: *The Journal of Physical Chemistry C* 122.1 (2017), pp. 194–206. ISSN: 1932-7455. DOI: 10.1021/acs.jpcc.7b10582.

[55] R. Hartkamp and B. Coasne. "Structure and transport of aqueous electrolytes: From simple halides to radionuclide ions". In: *The Journal of Chemical Physics* 141.12 (2014), p. 124508. DOI: http://dx.doi.org/10.1063/1.4896380.

[56] J. Mähler and I. Persson. "A Study of the Hydration of the Alkali Metal Ions in Aqueous Solution". In: *Inorganic Chemistry* 51.1 (Dec. 2011), pp. 425–438. ISSN: 1520-510X. DOI: 10.1021/ic2018693. URL: http://dx.doi.org/10.1021/ic2018693.

[57] K. D. Rasamani, F. Alimohammadi, and Y. Sun. "Interlayer-expanded MoS 2". In: *Materials Today* 20.2 (Mar. 2017), pp. 83–91. ISSN: 1369-7021. DOI: 10.1016/j.mattod.2016.10.004. URL: http://dx.doi.org/10.1016/j.mattod.2016.10.004.

[58] H. Li, Q. Zhang, C. C. R. Yap, B. K. Tay, T. H. T. Edwin, A. Olivier, and D. Baillargeat. "From Bulk to Monolayer MoS2: Evolution of Raman Scattering". In: *Advanced Functional Materials* 22.7 (Jan. 2012), pp. 1385–1390. ISSN: 1616-3028. DOI: 10.1002/adfm.201102111. URL: http://dx.doi.org/10.1002/adfm.201102111.

[59] R. N. Gontijo, A. Gadelha, O. J. Silveira, B. R. Carvalho, R. W. Nunes, L. C. Campos, M. A. Pimenta, A. Righi, and C. Fantini. "Temperature dependence of the double-resonance Raman bands in monolayer <scp>MoS2</scp>". In: *Journal of Raman Spectroscopy* 50.12 (Sept. 2019), pp. 1867–1874. ISSN: 1097-4555. DOI: 10.1002/jrs.5736. URL: http://dx.doi.org/10.1002/jrs.5736.

[60] H. Zeng, B. Zhu, K. Liu, J. Fan, X. Cui, and Q. M. Zhang. "Low-frequency Raman modes and electronic excitations in atomically thin MoS_2 films". In: *Phys. Rev. B* 86 (24 Dec. 2012), p. 241301. DOI: 10.1103/PhysRevB.86.241301. URL: https://link.aps.org/doi/10.1103/PhysRevB.86.241301.

[61] L. Li, Z. Qin, L. Ries, S. Hong, T. Michel, J. Yang, C. Salameh, M. Bechelany, P. Miele, D. Kaplan, M. Chhowalla, and D. Voiry. "Role of Sulfur Vacancies and Undercoordinated Mo Regions in MoS2 Nanosheets toward the Evolution of Hydrogen". In: *ACS Nano* 13.6 (May 2019), pp. 6824–6834. ISSN: 1936-086X. DOI: 10.1021/acsnano.9b01583. URL: http://dx.doi.org/10.1021/acsnano.9b01583.

[62] W. M. Parkin, A. Balan, L. Liang, P. M. Das, M. Lamparski, C. H. Naylor, J. A. Rodríguez-Manzo, A. T. C. Johnson, V. Meunier, and M. Drndić. "Raman Shifts in Electron-Irradiated Monolayer MoS2". In: *ACS Nano* 10.4 (2016), pp. 4134–4142. ISSN: 1936-086X. DOI: 10.1021/acsnano.5b07388. URL: http://dx.doi.org/10.1021/acsnano.5b07388.

[63] P. Maguire, C. Downing, J. Jadwiszczak, M. O'Brien, D. Keane, J. B. McManus, G. S. Duesberg, V. Nicolosi, N. McEvoy, and H. Zhang. "Suppression of the shear Raman mode in defective bilayer MoS2". In: *Journal of Applied Physics* 125.6 (Feb. 2019). ISSN: 1089-7550. DOI: 10.1063/1.5086366. URL: http://dx.doi.org/10.1063/1.5086366.

[64] Q. Wang, X. Li, X. Ma, Z. Li, and Y. Yang. "Activation of the MoS2 Basal Plane to Enhance CO Hydrogenation to Methane Activity Through Increasing S Vacancies". In: *ACS Applied Materials amp; Interfaces* 14.6 (Feb. 2022), pp. 7741–7755. ISSN: 1944-8252. DOI: 10.1021/acsami.1c18291. URL: http://dx.doi.org/10.1021/acsami.1c18291.

[65] X. Zhang, S. Wang, C.-K. Lee, C.-M. Cheng, J.-C. Lan, X. Li, J. Qiao, and X. Tao. "Unravelling the effect of sulfur vacancies on the electronic structure of the MoS_2 crystal". In: *Physical Chemistry Chemical Physics* 22.38 (2020), pp. 21776–21783. ISSN: 1463-9084. DOI: 10.1039/c9cp07004d.

[66] H. Fei, R. Liu, J. Wang, T. Guo, Z. Wu, D. Wang, and F. Liu. "Targeted Modulation of Competitive Active Sites toward Nitrogen Fixation via Sulfur Vacancy Engineering Over MoS_2". In:

Advanced Functional Materials 33.36 (2023). ISSN: 1616-3028. DOI: 10.1002/adfm.202302501.

[67] Q. Liu, Q. Fang, W. Chu, Y. Wan, X. Li, W. Xu, M. Habib, S. Tao, Y. Zhou, D. Liu, T. Xiang, A. Khalil, X. Wu, M. Chhowalla, P. M. Ajayan, and L. Song. "Electron-Doped 1T-MoS2 via Interface Engineering for Enhanced Electrocatalytic Hydrogen Evolution". In: *Chemistry of Materials* 29.11 (May 2017), pp. 4738–4744. ISSN: 1520-5002. DOI: 10.1021/acs.chemmater.7b00446. URL: http://dx.doi.org/10.1021/acs.chemmater.7b00446.

[68] W. Li, J. Huang, B. Han, C. Xie, X. Huang, K. Tian, Y. Zeng, Z. Zhao, P. Gao, Y. Zhang, T. Yang, Z. Zhang, S. Sun, and Y. Hou. "Molten-Salt-Assisted Chemical Vapor Deposition Process for Substitutional Doping of Monolayer MoS2 and Effectively Altering the Electronic Structure and Phononic Properties". In: *Advanced Science* 7.16 (July 2020). ISSN: 2198-3844. DOI: 10.1002/advs.202001080. URL: http://dx.doi.org/10.1002/advs.202001080.

[69] R. Zhang, L. Wei, J. Zhang, Y. Wang, X. Qiao, Y. Han, J. He, G. Zhang, X. Wu, L. Gu, S. Du, S. T. Pantelides, and H. J. Gao. "Superconductivity in potassium-doped metallic polymorphs of MoS_2". In: *Proceedings of the National Academy of Sciences* 113.31 (2016), pp. 8762–8765. DOI: 10.1073/pnas.1606042113.

[70] Q. Li, Y. Zhang, W. Chen, J. Sun, W. Huang, and H. Zhang. "Intermediate phases in sodium intercalation into MoS_2 nanosheets". In: *Nano Energy* 38 (2017), pp. 342–349. DOI: 10.1016/j.nanoen.2017.06.024.

[71] M. D. Curtis, J. E. Penner-Hahn, and K. E. Dungey. "Alkali-metal intercalation of MS_2: structure and bonding". In: *RSC Advances* 4 (2014), pp. 2942–2953. DOI: 10.1039/C3RA45477C.

[72] M. Tosun, L. Chan, M. Amani, T. Roy, G. H. Ahn, P. Taheri, C. Carraro, J. W. Ager, R. Maboudian, and A. Javey. "Air-Stable n-Doping of WSe2 by Anion Vacancy Formation with Mild Plasma Treatment". In: *ACS Nano* 10.7 (2016). ISSN: 1936086X. DOI: 10.1021/acsnano.6b02521.

[73] G. Barik and S. Pal. "Defect Induced Performance Enhancement of Monolayer MoS2 for Li- and Na-Ion Batteries". In: *The Journal of Physical Chemistry C* 123.36 (2019), pp. 21852–21865. DOI: 10.1021/acs.jpcc.9b04128. eprint: https://doi.org/10.1021/acs.jpcc.9b04128. URL: https://doi.org/10.1021/acs.jpcc.9b04128.

[74] S. Kim, M. Y. Lee, S. Lee, and S.-H. Jhi. "Super low work function of alkali-metal-adsorbed transition metal dichalcogenides". In: *Journal of Physics: Condensed Matter* 29.31 (July 2017), p. 315702. ISSN: 1361-648X. DOI: 10.1088/1361-648x/aa79bd. URL: http://dx.doi.org/10.1088/1361-648x/aa79bd.

[75] Y.-X. Yu. "Theoretical insights into surface-phase transition and ion competition during alkali ion intercalation on the Cu_4Se_4 nanosheet". In: *Phys. Chem. Chem. Phys.* 26 (2024), pp. 323–335. DOI: 10.1039/D3CP05423C.

[76] Y.-X. Yu. "Sodium/Potassium Intercalation on the Cu_4S_4 Nanosheet Accompanied by a Surface Phase Transition and Their Competition with Protons". In: *ACS Appl. Energy Mater.* 6.19 (2023), pp. 10048–10060. DOI: 10.1021/acsaem.3c01623.

[77] M. Asadi, B. Kumar, A. Behranginia, B. A. Rosen, A. Baskin, N. Repnin, D. Pisasale, P. Phillips, W. Zhu, R. Haasch, R. F. Klie, P. Král, J. Abiade, and A. Salehi-Khojin. "Robust carbon dioxide reduction on molybdenum disulphide edges". In: *Nature Communications* 5.1 (2014). DOI: 10.1038/ncomms5470. URL: https://doi.org/10.1038%2Fncomms5470.

[78] K. Yao, Z. Xu, J. Huang, M. Ma, L. Fu, X. Shen, J. Li, and M. Fu. "Bundled Defect-Rich MoS2 for a High-Rate and Long-Life Sodium-Ion Battery: Achieving 3D Diffusion of Sodium Ion by Vacancies to Improve Kinetics". In: *Small* 15.12 (Feb. 2019). ISSN: 1613-6829. DOI: 10.1002/smll.201805405. URL: http://dx.doi.org/10.1002/smll.201805405.

[79] S. Kang, S. Han, and Y. Kang. "Unveiling Electrochemical Reaction Pathways of CO2 Reduction to CN Species at S-Vacancies of MoS2". In: *ChemSusChem* 12.12 (May 2019), pp. 2671–2678. ISSN: 1864-564X. DOI: 10.1002/cssc.201900779. URL: http://dx.doi.org/10.1002/cssc.201900779.

4

Production of Higher Hydrocarbons via Electrochemical CO_2 Reduction on Sulfur-Vacant Molybdenum Disulfide Catalyst

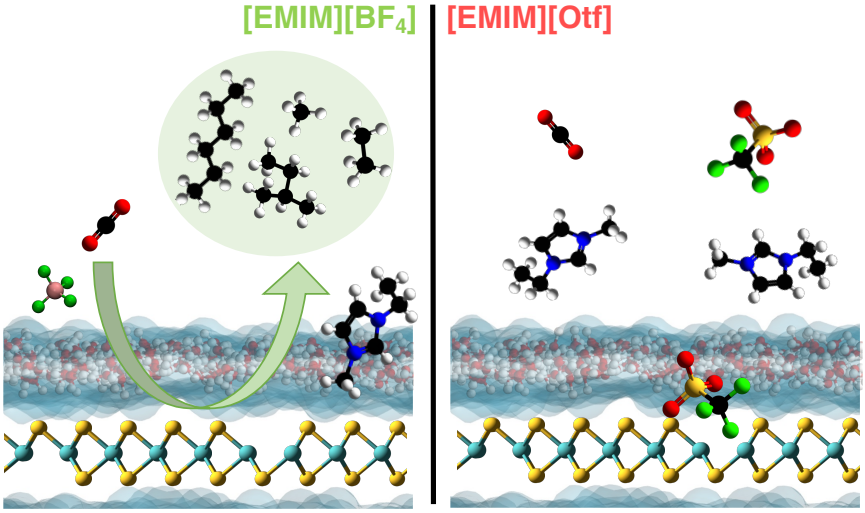

The chapter is based on:
E. Mádai, P.R. Anusuyadevi, P. Gonugunta, S. Mohseni Armaki, J.M.C. Mol, R.M. Hartkamp and P. Taheri, "Influence of Ionic-Liquid Anions on Electrochemical CO_2 Reduction to Higher Hydrocarbons on Sulfur-Vacant MoS_2" *under review at the Journal of Applied Catalysis O: Open*

4.1. Introduction & Background

The Paris agreement, signed by 196 parties in 2016, targets carbon-neutrality by 2050 [1]. Hence, establishing a carbon-neutral or carbon-negative cycle is one of the primary targets in research and policy since. This goal demands the development of viable technologies for carbon capture and utilization to value-added compounds [2]. Consequently, the electrochemical conversion of carbon dioxide (CO_2) to multi-carbon (C_n) species has attracted attention as it presents a viable path to carbon-neutrality [3].

Recently, 2D materials emerged as future electrocatalysts for CO_2 reduction reaction (CO_2RR) due to their high surface-to-bulk ratio [4]. Among them, transition metal dichalcogenides (TMDCs) showed great potential [5]. Their layered structure allows the surface-to-bulk ratio to be maximized with exfoliation and their earth-abundance makes them favorable and more cost-effective than precious metals. MoS_2, a prominent member of TMDCs, has garnered significant attention for its remarkable affordability, high tunability and efficiency in electrolysis. Currently, researchers are exploring its potential in the CO_2RR.

MoS_2 shows a great affinity towards the hydrogen evolution reaction (HER) [6] which, as a competitive reaction, reduces the CO_2RR efficiency. However, when molybdenum disulfide is aided by 1-ethyl-3-methylimidazolium tetrafluoroborate ([EMIM][BF_4]) as a co-catalyst, it offers a superior selectivity of the CO_2RR to carbon monoxide (CO), reported by Asadi et al. [7, 8]. It has been suggested that incorporating a co-catalyst can effectively lower the overpotential and suppress the HER by the ionic liquid (IL) adsorbing onto the catalyst surface, thereby blocking water molecules from accessing it [9]. While the HER is suppressed by the co-catalyst, the catalytic activity toward CO_2RR is attributed to the Mo-terminated edges of MoS_2, where Mo atoms facilitate a continuous electron supply to the attached intermediates, enhancing the reaction efficiency.

Building on these results, it was shown that doping vertically aligned (VA) MoS_2 with Nb-doping further increases the FE of the CO_2RR towards CO up to 90%, while Ta-doping decreases it due to a suboptimal electronic structure resulting from the binding between the Ta atoms and the host structure [10]. The improved FE for the $Nb_{0.05}Mo_{0.95}S_2$ is caused by the Nb atoms near the Mo-edge terminated MoS_2 which can potentially decrease the binding between the intermediates and the Mo atoms, leading to a higher turnover efficiency. Another study on CO_2RR using single-crystal-terrace MoS_2 electrodes (mechanically exfoliated MoS_2) in 0.1 M Na_2CO_3 aqueous solution established a correlation between edge density and product selectivity [11]. It revealed that increasing the edge density reduces the Faradaic efficiency (FE) for CO_2RR to 1-propanol, the primary product in this case. This suggests that in an aqueous environment, Mo-terminated edges favor HER over CO_2RR, while the activation of

basal planes is necessary for producing higher hydrocarbons. Although the HER significantly suppressed the CO_2RR, the authors also identified formate, ethylene glycol, methanol, and t-butanol in trace concentrations alongside 1-propanol.

Motivated by the available experimental information, density functional theory (DFT) calculations showed the possible pathways of the CO_2RR to CO or C_n products on MoS_2 [12]. As the reaction takes place on the exposed Mo edges, they showed that the d-band center of the Mo atom is much closer to the Fermi level of MoS_2 than for metallic catalysts, such as copper or titanium. Thus, the adsorbed species interact stronger with the Mo atoms. Furthermore, assuming that the intermediates are COOH* and CO*, their formation energies are smaller than those of CO_2 and CO (one of the possible primary products), thus the Mo atoms at the edges also exhibit a strong binding of the intermediates. The reaction pathway towards CO is energetically favorable to the pathway towards C_n products, consistent with findings in prior work[7]. While CO serves as a valuable feedstock for various chemical reactions, developing catalysts capable of directly producing a range of higher-carbon products offers significant advantages in terms of market value and energy density [13]. Many catalysts are only able to produce C_1-C_2 products and suffer from stability issues at high potentials [14, 15]. Hence, finding a way to achieve higher hydrocarbon products with a stable and active electrocatalyst like MoS_2 is of high interest.

A potential pathway for hydrocarbon production is linked to sulfur vacancies (V_Ss) in the MoS_2 structure. Building on the findings of Francis et al.[11], Kang et al.[16] proposed that the active sites are more likely to reside on the basal plane, based on the observation that an increased edge density correlates with a decrease in the FE toward 1-propanol [11]. The clean basal plane of the MoS_2 is known to be inert, hence the authors investigated the effect of sulfur vacancies as potential active sites in the basal plane. It is already proved that during the synthesis of MoS_2 films, V_Ss in the basal plane can occur up to 10% as their formation energy is relatively low (1-3 eV dependent on growth conditions) [17] and it has been shown that these V_Ss can act as active sites for the HER [18]. The authors demonstrated through DFT calculations that three sub-gap states, associated with V_Ss, are inherently localized. As a result, these states enable the independent occurrence of electron and proton transfer during the reduction reaction, which otherwise would proceed concurrently. Furthermore, the authors demonstrated that, contrary to previous studies, *OCHO is formed in the initial protonation step instead of *COOH due to the bowl-shape of the V_Ss as it sterically hinders the incorporation of more than one molecule into the vacancy site. Moreover, this new intermediate facilitates the formation pathway of formaldehyde as a C_1 product, a highly reactive chemical. As this new intermediate makes its binding to the active sites (sulfur vacancies) viable, in turn, it

also enables subsequent C-C coupling reactions, fostering the formation of higher C_n products.

Despite the theoretical studies on sulfur-vacant MoS_2 (V_S-MoS_2) as a catalyst for the electrochemical CO2 reduction reaction, the experimental influence of sulfur vacancies on product distribution remains unaddressed. Additionally, while the role of [EMIM][BF_4] as co-catalysts has been investigated, comparative studies involving different anions, beyond the commonly used [EMIM][BF4], are lacking. As Asadi et al. emphasized the importance of the [EMIM]$^+$ cation of the ionic liquids, because of the complex formation and the potential physisorption on the surface of the MoS_2 catalyst. Furthermore, results from the literature have suggested that along [EMIM][BF_4], 1-ethyl-3-methilimidazolium trifluoromethanesulfonate ([EMIM][Otf]) could be a possible co-catalyst to promote the CO_2RR over the HER [18]. Hence, in this work, we experimentally study V_S-MoS2 nanoflakes in the CO2RR using two ionic liquids, [EMIM][BF_4] and [EMIM][Otf], which share the [EMIM]$^+$ cation but differ in their anions. By comparing the performance of [EMIM][BF_4] and [EMIM][Otf], we aim to establish criteria for the key physicochemical properties an optimal co-catalyst should possess.

4.2. Results & Discussion

For the working electrodes MoS_2 nanopowder (Sigma-Aldrich, 90 nm average particle size) was mixed with carbon black (Fischer Scientific) and polyvinyl alcohol and then dropcasted on glassy carbon substrates.

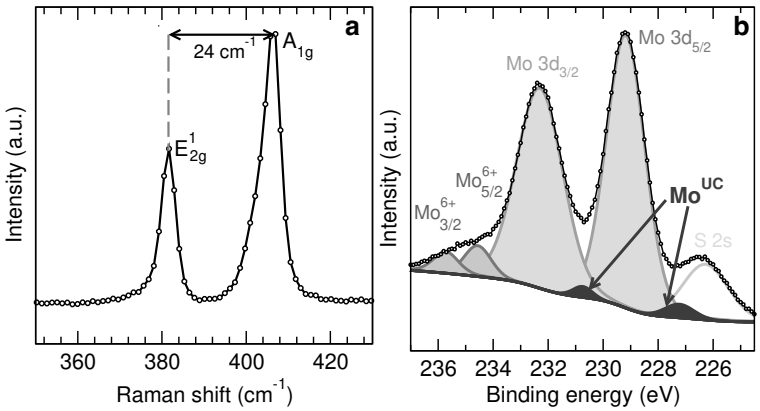

Figure 4.1. **(a)** Raman spectrum of the V_S-MoS_2 catalyst showing the two characteristic peaks, $E^1{}_{2g}$ and A_{1g} of the material, **(b)** Fitted Mo 3d5 XPS spectrum of the V_S-MoS_2 catalyst showing the different valence states of the Mo atoms in the structure.

Figure 4.1 (a) presents the Raman spectrum of the MoS_2 nanoflakes, where the separation between the two main characteristic peaks ($E^1{}_{2g}$ and A_{1g}) is 24 cm^{-1}, compared to 21 cm^{-1} for the pristine MoS_2 [19]. This larger separation shows the formation of monosulfur vacancies in the MoS_2 structure [20, 21]. X-ray photoelectron spectroscopy (XPS) further confirmed the presence of these monosulfur vacancies. Figure 2.1 (b) shows the fitted Mo 3d5 spectrum of the V_S-MoS_2 catalyst, where the two main peaks were identified as the Mo $3d_{3/2}$ and $3d_{5/2}$ peaks at 229.1 eV and 232.4 eV, respectively. Furthermore, Mo^{6+} was identified due to possible oxidation during the sonication process; and undercoordinated Mo sites (Mo^{UC}) were also found, which confirms the presence of the monosulfur vacancies [21–23]. The SEM image in Figure B.2 shows the differently oriented V_S-MoS_2 nanoflakes at the surface of the catalyst. The image shows that mainly the basal planes of the V_S-MoS_2 nanoflakes were exposed on the surface, giving the opportunity for the activation of these planes.

To see the effect of monosulfur vacancies in the V_S-MoS_2 structure on the product distribution of the electrochemical CO_2 reduction, two different ionic liquids were used as co-catalysts to promote the CO_2RR. They were each used as 30 vol% IL mixed with 70 vol% deionized water and purged with CO_2 gas. Figure 4.2 shows the linear sweep voltammetry curves obtained with the two different co-catalysts. For [EMIM][BF_4], a small reduction well was seen at 0.9 V vs RHE, while no reduction well was detected with [EMIM][Otf]. Nonetheless, the CO_2 reduction efficiency was measured with gas chromatography and then the FE was calculated for both ionic liquids, which is shown in Figure 4.3. When [EMIM][BF_4] was used

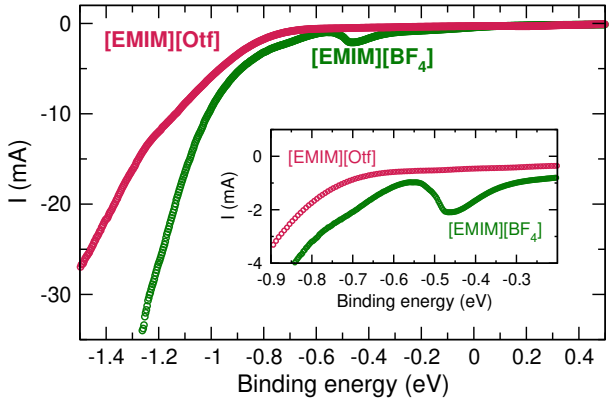

Figure 4.2. Recorded linear sweep voltammetry curves of the MoS_2 catalyst in [EMIM][BF_4]-water mixture (green) and [EMIM][Otf]-water (red) mixture.

as a co-catalyst, a wide range of hydrocarbons (CH_4, C_2H_6, i-H_5C_{12} and C_6H_{10}) was produced with some hydrogen as a side-product. Out of this range of hydrocarbons, isopentane emerged as the main product with 44% FE. On the other hand, when [EMIM][Otf] is used as a co-catalyst, hydrogen is the only product that is detected.

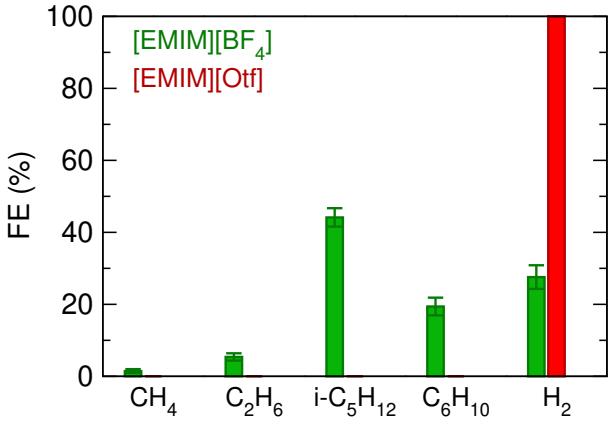

Figure 4.3. Calculated Faradaic efficiencies and product distribution of the CO_2RR on MoS_2 with the two different 30 vol% ILs and 70 vol% water mixtures as co-catalysts at -0.9 V vs RHE.

A crucial feature of MoS_2 is the deviation from the linear scaling relations, where the adsorption energy scales with the concentration of the intermediate [24]. It has been shown that for different transition-metal catalysts the adsorption energies of the COOH* and the CHO* intermediates are strongly correlated with the adsorption energy of CO* [25]. In the case of V_S-MoS_2, the exposed transition metal Mo atoms are the active sites for the CO_2RR. Hence, these linear scaling relations between the reaction intermediates of the CO_2RR also strongly affect the reduction activity of the transition-metal catalysts [26]. These relations also suggest that the stability of COOH* and CHO* is strongly dependent on CO*, whereas a criterion for the catalyst would be to stabilize COOH* and CHO* better than CO*. In this regard, it was also shown that MoS_2 and $MoSe_2$ (both pristine and doped) break the scaling relations by binding the COOH*and CHO* more strongly than the CO*/CO, leading to a higher selectivity [27]. This phenomenon is attributed to the presence of S and Se atoms on the edges of the catalysts, which have a higher binding affinity towards the other intermediates than towards CO. On the other hand, this higher affinity towards the binding of these intermediates also implies the affinity towards C_n (n>1) products, as to produce longer chain hydrocarbons in addition to the expected selectivity as it was also shown by Francis et al.[11] and our experiments. Hence, the synergy of using

V_S-MoS_2 as a catalyst originates from two factors: (1) that it inherently breaks the linear scaling relations between the reaction intermediates [24] and (2) it exposes transition metal centers as active sites for the CO_2RR due to the sulfur vacancies [21, 28].

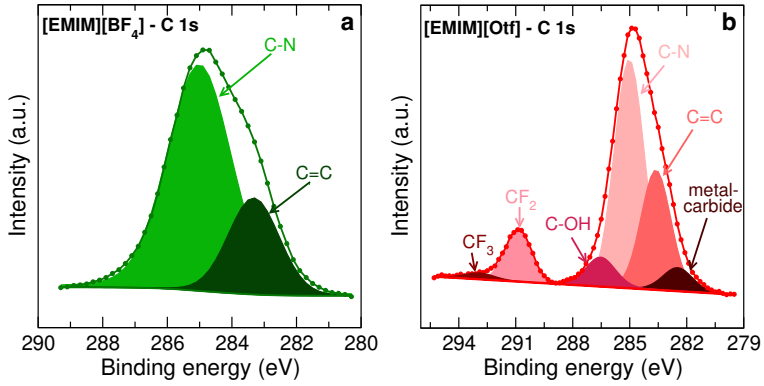

Figure 4.4. Normalized C 1s XPS spectra of VS-MoS2 catalyst exposed to **(a)** [EMIM][BF4] and to **(b)** [EMIM][Otf].

To assess the origin of the difference between the product distributions when the different ionic liquids were used as co-catalysts, XPS measurements were done on the exposed V_S-MoS_2 catalysts. Figure 4.4 (a) shows the fitted C 1s spectrum of the V_S-MoS_2 catalyst exposed prior to [EMIM][BF_4]. Two subpeaks were found, one peak was identified at 283.5 eV which comprises the adventitious carbon peak (284.4 eV, possible contamination from the device) and the C=C bonding from the IL [29], and a C-N bonding peak at 285.5 eV [30]. The latter peak could originate from the physisorbed $[EMIM]^+$ cation, as the ab-initio molecular dynamics simulations of Asadi et al. indicated[7]. Figure 4.4 (b) presents the deconvoluted C 1s spectrum of the V_S-MoS_2 catalyst exposed to [EMIM][Otf]. During the deconvolution, 6 peaks were identified: at 282.5 a small peak which shows the presence of metal carbides on the surface, the adventitious carbon and the C=C bond from the IL at 283.5 eV, the C-N bonding at 285.5 eV showing the presence of the $[EMIM]^+$ cation on the surface, a small C-OH peak at 286.5 eV and CF_2 and CF_3 peaks at 291 eV and 293 eV, respectively[29]. The presence of the metal carbide, CF_2 and CF_3 peaks leads to the assumption that the [Otf]- anion of the ionic liquid is chemically bound to the undercoordinated Mo sites of the V_S-MoS_2 catalyst. As the $[Otf]^+$ anion possesses a CF_3 group, the small peak of the CF_3 group and the larger peak of the CF_2 group and the presence of the metal-carbide peak suggests that the anion of the ionic liquid is chemically bound to the Mo atom. This binding process is likely to occur on the Mo atoms that are exposed on the surface due to the

presence of the sulfur vacancies. Therefore, as the active sites of the electrochemical CO_2RR are blocked, H_2 was the only product measured.

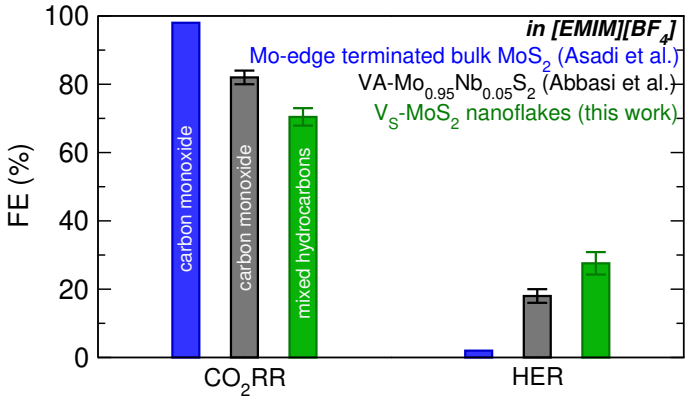

Figure 4.5. Comparison of CO_2RR FE of V_S-MoS_2 nanoflakes with Mo-edge terminated bulk MoS_2 and VA-$Nb_{0.05}Mo_{0.95}S_2$ with [EMIM][BF_4] as co-catalyst. For comparison data was extracted from Abbasi et al.[10] and Asadi et al.[7].

Figure 4.5 compares the Faradaic efficiencies of CO_2RR and HER when [EMIM][BF_4] is used as co-catalyst between this work (V_S-MoS_2), and other data that can be found in the literature, namely the Mo-edge terminated bulk MoS_2 (Asadi et al.) and VA-$Nb_{0.05}Mo_{0.95}S_2$ (Abbasi et al.) catalysts. For the V_S-MoS_2 catalyst, the different hydrocarbon products of the CO_2RR are added up, reaching 70% overall FE for the CO_2RR, which is lower than the bulk MoS_2 and the VA-$Nb_{0.05}Mo_{0.95}S_2$ catalysts, with 98% and 82% FEs, respectively. Improving the FE of the V_S-MoS_2 can potentially originate from two sources: (1) improving the electronic properties of the V_S-MoS_2 catalyst and/or (2) finding a more suitable co-catalyst in the form of different ionic liquids.

Abbasi et al. showed that doping MoS_2 with different metals is a potential way to change its material properties and through that, influence the FE of CO_2RR. However, the dopant must be carefully selected, as it can also negatively impact the efficiency of the CO_2RR[10]. To avoid this potentially negative influence on the efficiency, another path to change the electronic properties is through utilizing the layered 2-dimensional structure of MoS_2 and intercalate different ions in the interlayer space. The conductivity of MoS_2 can be increased through electron donation from the intercalants [31, 32], which can potentially influence the product distribution and the FE of the CO_2RR. Regarding the effect of the co-catalyst, we experimentally proved that the $[EMIM]^+$ cation is indeed important for creating an environment that favors the CO_2RR over the HER at the catalyst surface. However, using [EMIM][BF_4] as a co-catalyst

also has the hazardous aspect that the [BF_4]- anion can hydrolyse to HF [7]. This aspect compromises the potential for scaling up the process. Furthermore, the capacity of [EMIM][BF_4] to absorb CO_2 is much lower than that of other imidazolium-based ionic liquids [33]. We also showed that not only does the cation of the ionic liquid matter, but also the anion, as it can potentially poison the catalyst. Taking all these criteria into account, imidazolium-based acetates seem to be an ideal choice as a next step for co-catalyst selection, due to their high affinity towards CO_2 absorption, stable structure and lack of potential side-reactions [34].

4.3. Conclusions

We experimentally demonstrated that introducing sulfur vacancies into the basal plane of MoS_2 enhances its catalytic activity for the electrochemical CO_2 reduction reaction, enabling the formation of multi-carbon (C_n) products. However, the presence of V_S alone results in a broad product distribution with limited selectivity. To further understand the catalytic environment, we investigated the role of the ionic liquid co-catalyst by comparing [EMIM][BF_4] and [EMIM][Otf], which share the $[EMIM]^+$ cation but differ in their anions. Our results reveal that, in addition to the crucial contribution of the $[EMIM]^+$ cation, the choice of anion significantly affects catalytic performance by influencing surface interactions. Specifically, chemically aggressive anions may bind to the catalyst surface and deactivate it. Hence, the criteria for an efficient co-catalyst includes imidazolium-based ionic liquids with anions which are less reactive, furthermore, possess a structure which allows high CO_2 uptake (such as acetates) which can enhance CO_2 availability. Moreover, safety considerations are critical, as certain anions like BF_4^- may lead to hazardous by-products, such as HF. These findings address key experimental gaps in the understanding of sulfur-vacant MoS_2 catalysts and ionic liquid composition in CO_2RR, and they provide a foundation for the rational design of more effective and selective catalyst–co-catalyst systems.

references

[1] M.-C. C. Segger. "Advancing the Paris Agreement on climate change for sustainable development". In: *Cambridge International Law Journal* 5.2 (2016), pp. 202–237.

[2] G. Garcia-Garcia, M. C. Fernandez, K. Armstrong, S. Woolass, and P. Styring. "Analytical review of life-cycle environmental impacts of carbon capture and utilization technologies". In: *ChemSusChem* 14.4 (2021), pp. 995–1015.

[3] M. G. Kibria, J. P. Edwards, C. M. Gabardo, C.-T. Dinh, A. Seifitokaldani, D. Sinton, and E. H. Sargent. "Electrochemical CO2 reduction into chemical feedstocks: from mechanistic electrocatalysis models to system design". In: *Advanced Materials* 31.31 (2019), p. 1807166.

[4] X. Duan, J. Xu, Z. Wei, J. Ma, S. Guo, S. Wang, H. Liu, and S. Dou. "Metal-free carbon materials for CO2 electrochemical reduction". In: *Advanced Materials* 29.41 (2017), p. 1701784.

[5] F.-Y. Gao, Z.-Z. Wu, and M.-R. Gao. "Electrochemical CO2 reduction on transition-metal chalcogenide catalysts: recent advances and future perspectives". In: *Energy & Fuels* 35.16 (2021), pp. 12869–12883.

[6] D. Voiry, M. Salehi, R. Silva, T. Fujita, M. Chen, T. Asefa, V. B. Shenoy, G. Eda, and M. Chhowalla. "Conducting MoS2 nanosheets as catalysts for hydrogen evolution reaction". In: *Nano letters* 13.12 (2013), pp. 6222–6227.

[7] M. Asadi, B. Kumar, A. Behranginia, B. A. Rosen, A. Baskin, N. Repnin, D. Pisasale, P. Phillips, W. Zhu, R. Haasch, *et al.* "Robust carbon dioxide reduction on molybdenum disulphide edges". In: *Nature communications* 5.1 (2014), p. 4470.

[8] M. Asadi, K. Kim, C. Liu, A. V. Addepalli, P. Abbasi, P. Yasaei, P. Phillips, A. Behranginia, J. M. Cerrato, R. Haasch, *et al.* "Nanostructured transition metal dichalcogenide electrocatalysts for CO2 reduction in ionic liquid". In: *Science* 353.6298 (2016), pp. 467–470.

[9] B. A. Rosen, J. L. Haan, P. Mukherjee, B. Braunschweig, W. Zhu, A. Salehi-Khojin, D. D. Dlott, and R. I. Masel. "In situ spectroscopic examination of a low overpotential pathway for carbon dioxide conversion to carbon monoxide". In: *The Journal of Physical Chemistry C* 116.29 (2012), pp. 15307–15312.

[10] P. Abbasi, M. Asadi, C. Liu, S. Sharifi-Asl, B. Sayahpour, A. Behranginia, P. Zapol, R. Shahbazian-Yassar, L. A. Curtiss, and A. Salehi-Khojin. "Tailoring the edge structure of molybdenum disulfide toward electrocatalytic reduction of carbon dioxide". In: *ACS nano* 11.1 (2017), pp. 453–460.

[11] S. A. Francis, J. M. Velazquez, I. M. Ferrer, D. A. Torelli, D. Guevarra, M. T. McDowell, K. Sun, X. Zhou, F. H. Saadi, J. John, *et al.* "Reduction of aqueous CO2 to 1-propanol at MoS2 electrodes". In: *Chemistry of Materials* 30.15 (2018), pp. 4902–4908.

[12] Y. Xie, X. Li, Y. Wang, B. Li, L. Yang, N. Zhao, M. Liu, X. Wang, Y. Yu, and J.-M. Liu. "Reaction mechanisms for reduction of CO2 to CO on monolayer MoS2". In: *Applied Surface Science* 499 (2020), p. 143964.

[13] S. Verma, S. Lu, and P. J. Kenis. "Co-electrolysis of CO2 and glycerol as a pathway to carbon chemicals with improved technoeconomics due to low electricity consumption". In: *Nature Energy* 4.6 (2019), pp. 466–474.

[14] X. Zhi, Y. Jiao, Y. Zheng, A. Vasileff, and S.-Z. Qiao. "Selectivity roadmap for electrochemical CO2 reduction on copper-based alloy catalysts". In: *Nano Energy* 71 (2020), p. 104601.

[15] M. T. Tang, H. Peng, P. S. Lamoureux, M. Bajdich, and F. Abild-Pedersen. "From electricity to fuels: descriptors for C1 selectivity in electrochemical CO2 reduction". In: *Applied Catalysis B: Environmental* 279 (2020), p. 119384.

[16] S. Kang, S. Han, and Y. Kang. "Unveiling Electrochemical Reaction Pathways of CO2 Reduction to CN Species at S-Vacancies of MoS2". In: *ChemSusChem* 12.12 (2019), pp. 2671–2678.

[17] G. Li, D. Zhang, Q. Qiao, Y. Yu, D. Peterson, A. Zafar, R. Kumar, S. Curtarolo, F. Hunte, S. Shannon, *et al.* "All the catalytic active sites of MoS2 for hydrogen evolution". In: *Journal of the American Chemical Society* 138.51 (2016), pp. 16632–16638.

[18] A. Hailu and S. K. Shaw. "Efficient electrocatalytic reduction of carbon dioxide in 1-ethyl-3-methylimidazolium trifluoromethanesulfonate and water mixtures". In: *Energy & Fuels* 32.12 (2018), pp. 12695–12702.

[19] H. Li, Q. Zhang, C. C. R. Yap, B. K. Tay, T. H. T. Edwin, A. Olivier, and D. Baillargeat. "From Bulk to Monolayer MoS2: Evolution of Raman Scattering". In: *Advanced Functional Materials* 22.7 (Jan. 2012), pp. 1385–1390. ISSN: 1616-3028. DOI: 10.1002/adfm.201102111. URL: http://dx.doi.org/10.1002/adfm.201102111.

[20] Q. Wang, X. Li, X. Ma, Z. Li, and Y. Yang. "Activation of the MoS2 basal plane to enhance CO hydrogenation to methane activity through increasing S vacancies". In: *ACS Applied Materials & Interfaces* 14.6 (2022), pp. 7741–7755.

[21] L. Li, Z. Qin, L. Ries, S. Hong, T. Michel, J. Yang, C. Salameh, M. Bechelany, P. Miele, D. Kaplan, *et al.* "Role of sulfur vacancies and undercoordinated Mo regions in MoS2 nanosheets toward the evolution of hydrogen". In: *ACS nano* 13.6 (2019), pp. 6824–6834.

[22] X. Zhang, S. Wang, C.-K. Lee, C.-M. Cheng, J.-C. Lan, X. Li, J. Qiao, and X. Tao. "Unravelling the effect of sulfur vacancies on the electronic structure of the MoS_2 crystal". In: *Physical Chemistry Chemical Physics* 22.38 (2020), pp. 21776–21783. ISSN: 1463-9084. DOI: 10.1039/c9cp07004d.

[23] H. Fei, R. Liu, J. Wang, T. Guo, Z. Wu, D. Wang, and F. Liu. "Targeted Modulation of Competitive Active Sites toward Nitrogen Fixation via Sulfur Vacancy Engineering Over MoS_2". In: *Advanced Functional Materials* 33.36 (2023). ISSN: 1616-3028. DOI: 10.1002/adfm.202302501.

[24] Y. Ji, J. K. Nørskov, and K. Chan. "Scaling relations on basal plane vacancies of transition metal dichalcogenides for CO2 reduction". In: *The Journal of Physical Chemistry C* 123.7 (2019), pp. 4256–4261.

[25] A. A. Peterson and J. K. Nørskov. "Activity descriptors for CO2 electroreduction to methane on transition-metal catalysts". In: *The Journal of Physical Chemistry Letters* 3.2 (2012), pp. 251–258.

[26] P. Mano, T. Jitwatanasirikul, T. Roongcharoen, K. Takahashi, and S. Namuangruk. "Tuning covalent bonding of single transition metal atom doped in S vacant MoS2 for catalytic CO2 reduction reaction product selectivity". In: *Applied Surface Science* 688 (2025), p. 162339.

[27] K. Chan, C. Tsai, H. A. Hansen, and J. K. Nørskov. "Molybdenum sulfides and selenides as possible electrocatalysts for CO2 reduction". In: *ChemCatChem* 6.7 (2014), pp. 1899–1905.

[28] H. Li, C. Tsai, A. L. Koh, L. Cai, A. W. Contryman, A. H. Fragapane, J. Zhao, H. S. Han, H. C. Manoharan, F. Abild-Pedersen, *et al.* "Activating and optimizing MoS2 basal planes for hydrogen evolution through the formation of strained sulphur vacancies". In: *Nature materials* 15.1 (2016), pp. 48–53.

[29] K. Dave, K. H. Park, and M. Dhayal. "Two-step process for programmable removal of oxygen functionalities of graphene oxide: functional, structural and electrical characteristics". In: *RSC advances* 5.116 (2015), pp. 95657–95665.

[30] J. Kalaiyarasi, K. Pandian, S. Ramanathan, and S. C. Gopinath. "Graphitic carbon nitride/graphene nanoflakes hybrid system for electrochemical sensing of DNA bases in meat samples". In: *Scientific Reports* 10.1 (2020), p. 12860.

[31] R. Somoano, V. Hadek, and A. Rembaum. "Alkali metal intercalates of molybdenum disulfide". In: *The Journal of Chemical Physics* 58.2 (1973), pp. 697–701.

[32] X. Wang, X. Shen, Z. Wang, R. Yu, and L. Chen. "Atomic-scale clarification of structural transition of MoS2 upon sodium intercalation". In: *ACS nano* 8.11 (2014), pp. 11394–11400.

[33] C. Wang, H. Luo, X. Luo, H. Li, and S. Dai. "Equimolar CO 2 capture by imidazolium-based ionic liquids and superbase systems". In: *Green chemistry* 12.11 (2010), pp. 2019–2023.

[34] J. D. Watkins and A. B. Bocarsly. "Direct Reduction of Carbon Dioxide to Formate in High-Gas-Capacity Ionic Liquids at Post-Transition-Metal Electrodes". In: *ChemSusChem* 7.1 (2014), pp. 284–290.

5

Effect of anion of ionic liquids on CO_2 reduction selectivity with MoS_2

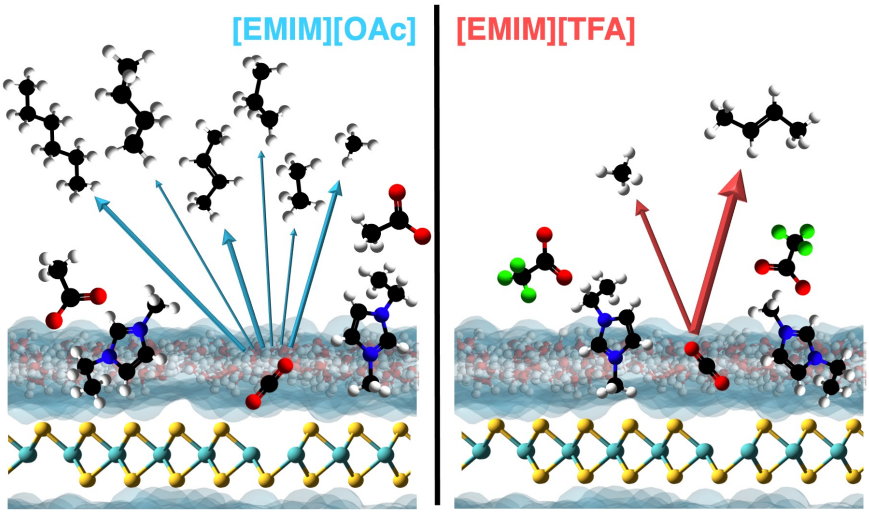

The chapter is based on:
E. Mádai, N. Khossosi, P. Ravi Anusuyadevi, P. Gonogunta, R. Hartkamp, J.M.C. Mol, P. Dey and P. Taheri, "Effect of imidazolium-based acetates as co-catalysts on the product selectivity of the electrochemical CO_2 reduction reaction Using MoS_2" *in preparation*

5.1. Introduction

The global rise in CO_2 emissions and the sustained reliance on fossil fuels over recent decades have significantly contributed to environmental degradation and an increase in the frequency and intensity of extreme weather events driven by global warming [1]. Despite growing awareness of these impacts, fossil fuels remain the predominant energy source worldwide, with global consumption projected to double by 2050 [2]. Current estimates suggest that cumulative CO_2 emissions may reach 500 Gt by 2060 [3]. Addressing the critical issue of atmospheric CO_2 accumulation is essential to mitigate the severe consequences of climate change. Among the various strategies under investigation, the capture and conversion of CO_2 into value-added fuels through electrocatalysis or photocatalysis represents a particularly promising approach [4–7].

Using 2D materials as catalysts in electrocatalysis and photocatalysis presents a novel path due to their high surface-to-bulk ratio. Hence, N-doped graphene [8, 9], 2-dimensional metal-organic frameworks [10, 11] and transition metal dichalcogenides (TMDCs) [12–15] have been lately researched extensively as potential electro- and photocatalysts. Molybdenum disulfide (MoS_2), a prominent member of TMDCs, had shown potential as a catalyst both for CO_2 reduction in organic media [12–14] and for hydrogen production in aqueous media [16–18]. MoS_2, predominantly existing in its semiconducting 2H phase, is a layered material that offers the advantage of facile monolayer fabrication. Asadi et al. used the MoS_2 monolayers as a electrocatalysts for CO_2 reduction to CO in the presence of a 1-ethyl-3-methylimidazolium tetrafluoroborate ([EMIM][BF_4]) co-catalyst [12–14]. Their results showed that the Mo-terminated edges are responsible for a robust CO_2 reduction when [EMIM][BF_4] is used as a co-catalyst [13]. Additionally, when the vertically aligned MoS_2 was doped with Nb atoms, the turnover frequency of CO_2 reduction to CO was further increased, they achieved a Faradaic Efficiency (FE) of CO_2 reduction to CO above 80% [12].

While the production of CO from CO_2 is beneficial, as it serves as a feedstock or building block for downstream chemical processes, the direct conversion of CO_2 into multicarbon products may be more advantageous in terms of energy efficiency and overall process economics. The potential of MoS_2 to produce multicarbon species directly from CO_2 was also theoretically explored [19–21]. Kang et al. studied the effect of sulfur vacancies (V_S) in the MoS_2 structure on the selectivity of CO_2 reduction using ab initio calculations [19]. They found that while pristine MoS_2 is highly selective towards C_1 products (methane and CO), MoS_2 with sulfur vacancies shows selectivity towards multicarbon species [19]. Sulfur vacancies on the basal plane were already known to be catalytic sites for HER [22, 23], however, they showed that the vacancies can also adsorb CO_2 and its reduction intermediates, thus facilitating the carbon-carbon coupling and the growth of hydrocarbon chains. Their theory was

confirmed experimentally by chapters 3 and 4, where sulfur-vacant-MoS_2 (V_S-MoS_2) was used as a catalyst for CO_2 reduction to multicarbon species together with [EMIM][BF_4] as a co-catalyst.

The requirement for a co-catalyst arises from the high HER activity of MoS_2, as the presence of an ionic liquid facilitates CO_2RR [12, 13]. Using [EMIM][BF_4] as a co-catalyst was favored by Asadi et al. [13], as they showed through ab-initio molecular dynamics simulations that the cation of the ionic liquid can potentially form a complex with the CO_2 molecule, which then can physisorb on the surface of the MoS_2 catalyst. Using [EMIM][BF_4], however, gives a way to the formation of HF during the reaction, which poses a potential danger for the setup and the reaction environment. Hence, our investigation turned towards other imidazolium-based ionic liquids with the criteria of minimized possibility towards side-reactions and improved CO_2 absorption properties compared with [EMIM][BF_4]. It was shown that the [EMIM]-acetates, namely 1-Ethyl-3-

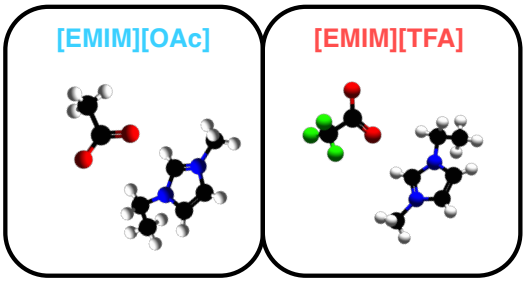

Figure 5.1. Molecular structures of the imidazolium-based ionic liquids investigated as potential co-catalysts, (left panel) [EMIM][OAc] and (right panel) [EMIM][TFA].

methylimidazolium acetate ([EMIM][OAc]) and 1-Ethyl-3-methylimidazolium trifluoroacetate ([EMIM][TFA]) can absorb CO_2 up to 27 mol% [24]. Figure 5.1 shows the molecular structure of the two ionic liquids, where the main difference in the anions can be seen: the three hydrogen atoms of the acetate anion are changed to fluor atoms in the trifluoroacetate anion.

The electrochemical reduction of CO_2 (CO_2RR) on conventional *p*-block metals such as indium, tin, and lead typically yields formate as the dominant product and suffers from modest Faradaic efficiencies [25]. As these metals obey linear scaling relationships that also govern the competing hydrogen-evolution reaction (HER), further improvements in selectivity are intrinsically limited. In contrast, TMDCs break these scaling relations and therefore offer a promising platform for steering CO_2RR pathways toward more valuable products [26]. Ionic liquids are frequently employed as co-catalysts [12, 13] or media to enhance CO_2 capture

[27, 28], yet their interaction with CO_2 is highly structure-dependent: for example, [EMIM][OAc] chemisorbs CO_2, whereas [EMIM][TFA] interacts mainly through physisorption [29]. When TMDC electrodes are paired with such ILs, the mode of CO_2 uptake is expected to modulate transport to S-vacancy sites in MoS_2 and thus influence both product distribution and overall selectivity. Despite this intuitive link, the combined effect of CO_2 absorption chemistry in ILs and the unique catalytic landscape of TMDCs remains largely unexplored, constituting the knowledge gap that the present work addresses.

In this chapter, we explore the impact of [EMIM][OAc] and [EMIM][TFA] ionic liquids co-catalysts on the electrochemical CO_2 reduction reaction towards multicarbon products using V_S-containing MoS_2 as the catalyst. Our experimental findings demonstrate that the presence of sulfur vacancies, identified with X-ray photoelectron spectroscopy and Raman spectroscopy, significantly affects the reaction selectivity, promoting the formation of multicarbon products over C1 products. Moreover, we show through DFT calculations that the nature of the interaction between the CO_2 molecule and the ionic liquid co-catalyst — whether through physisorption or chemisorption — plays a crucial role in dictating the product distribution and overall selectivity of the CO_2RR.

5.2. Methods and Materials

5.2.1. Experimental

Electrode preparation

The commercially available MoS_2 nanopowder (99% trace metals basis, Sigma Aldrich) was used to prepare electrodes. A mixture of MoS_2, carbon black (CB, Fisher Scientific), and poly(vinyl alcohol) (PVA) was prepared in a 90:5:5 weight ratio and transferred to a 5 cm^3 vial with 2 mL of deionized (DI) water. The suspension was sonicated in a water bath for 10 minutes to achieve uniform dispersion. Glassy carbon substrates (1.5 cm × 1.5 cm, Sigma Aldrich) were cleaned with DI water, sonicated in isopropyl alcohol for 5 minutes, and dried with compressed air. Subsequently, 25 μL of the ink was drop-cast onto each substrate and dried under ambient conditions. A copper tape was affixed to the substrate as an electrical contact, and the electrode was masked to expose a circular area of 10 mm in diameter.

Electrochemical measurements

Linear Sweep Voltammetry (LSV) measurements were carried out using a BioLogic VMP-3e multichannel potentiostat controlled via EC-Lab software. The working electrode was placed in the cathodic compartment together with a micro Ag/AgCl reference electrode (Mengel Engineering), while a platinum mesh served as the counter electrode in the anodic

compartment. All electrodes were connected to the potentiostat, and the system was enclosed in a Faraday cage to minimize electrical noise.

Raman Spectroscopy

Raman spectra were acquired using a WiTec Alpha300R Raman imaging microscope equipped with a 532 nm excitation laser operated at 1 mW to prevent sample damage. Spectra were collected with a 5-second integration time over 10 accumulations using a 63×/0.9 water-dipping objective. A 1800 g/mm grating was employed to achieve a spectral resolution better than 1 cm^{-1}.

Scanning Electron Microscopy

Scanning Electron Microscopy (SEM) imaging was performed using a JEOL IT800SHL system equipped with a field emission gun, operated at an accelerating voltage of 10.00 kV and a beam current of 42.20 nA.

X-ray Photoelectron Spectroscopy

X-ray Photoelectron Spectroscopy (XPS) measurements were conducted using a PHI 5400 system (Physical Electronics, Eden Prairie, USA) with a non-monochromatic Al Kα X-ray source (13.5 kV, 200 W). Core-level spectra were recorded with a step size of 0.1 eV and a dwell time of 1.25 s using a spherical capacitor analyzer set to a pass energy of 71.55 eV. Data analysis was performed using MultiPak software; peaks were normalized and fitted with an iterated-Shirley background.

Product analysis

Product analysis was performed in a two-compartment, three-electrode electrochemical H-cell (Pine Research) connected to a BioLogic SP-50e potentiostat. The anode compartment contained a Pt wire counter electrode, while the cathode compartment housed the working electrode, a micro Ag/AgCl reference electrode (Mengel Engineering), and a glass tube for continuous CO_2 purging into the electrolyte. The working electrode consisted of MoS_2 drop-cast on a 15 mm × 15 mm glassy carbon substrate, masked to expose a circular area of 10 mm in diameter, and connected to the potentiostat via copper tape. Both compartments were filled with an electrolyte composed of 70 vol% deionized water and 30 vol% [EMIM][BF_4] (Iolitec). Prior to the measurements, the electrolyte was purged with CO_2 for 1 hour at a flow rate of 10 mL/min. A constant potential was then applied for 1 hour, during which CO_2 bubbling was maintained at 10 mL/h to ensure a continuous supply for the CO_2 reduction reaction. Gas samples were collected from the cathodic compartment every 10 minutes using a 10 mL Hamilton gas-tight sample lock syringe and analyzed via gas chromatography (GC, CompactGC 4.0,

Interscience). The GC was equipped with three detectors: two thermal conductivity detectors (TCDs) with Carboxen1010 columns and one flame ionization detector (FID). The first TCD channel used helium (He, 99.999%, Linde) as the carrier gas, enabling detection of O_2, N_2, CO, and CO_2. The second TCD channel used argon (Ar, 99.999%, Linde) to detect H_2, while the FID enabled detection of hydrocarbon species. The GC system was baked out and calibrated using certified gas standards (Linde) for H_2, CH_4, C_2H_6, C_3H_8, C_4H_{10}, C_5H_{12}, C_5H_{10}, C_6H_{14}, C_6H_{12}, and C_7H_{14}. For Faradaic efficiency (FE) calculations, chromatographic peak areas were extracted using Chromeleon software and converted to ppm values based on GC calibration curves. FEs were then calculated according to the method reported by Asadi et al.[12–14], using the following equation:

$$FE = \frac{\text{moles}_{\text{product}} \times nF}{I \times t} \times 100, \tag{5.1}$$

where n is the number of electrons transferred per product molecule, F is the Faraday constant, I is the applied current, and t is the duration of the electrolysis.

5.2.2. Computational details

All calculations were performed within the density functional theory (DFT) framework as implemented in the Vienna Ab initio Simulation Package (VASP) [30, 31]. We employed the projector augmented wave (PAW) method to describe the electron-ion interactions [32, 33], with a plane-wave cutoff energy of 520 eV. The exchange-correlation effects were treated using the Perdew-Burke-Ernzerhof (PBE) functional [34], with Grimme's D3 dispersion correction including Becke-Johnson damping [35] to accurately capture the weak interactions governing physisorption processes. This methodology has been extensively validated for systems involving ionic liquids and 2D materials [36, 37]. For all calculations, the electronic self-consistency was converged to 10^{-6} eV, and the geometric relaxations were performed until the Hellmann-Feynman forces on all atoms were less than 0.01 eV/Å. Spin polarization was included throughout all calculations to properly account for the magnetic moments induced by sulfur vacancies. The Brillouin zone was sampled using a 3×3×1 Γ-centered Monkhorst-Pack k-point mesh for structural relaxations, with a denser 9×9×1 grid employed for density of states (DOS) calculations to ensure high-resolution electronic structure analysis critical for identifying subtle changes in orbital hybridization.

The S-defective MoS_2 substrate was constructed as a 5×5×1 supercell containing a single S-vacancy, corresponding to a 2% vacancy concentration identified as catalytically optimal in previous experimental studies [38, 39]. A vacuum spacing of 25 Å perpendicular to the MoS_2 sheet was utilized to eliminate spurious interactions between periodic images.

Two distinct vacancy sites were considered, and after full optimization, the top-layer S-vacancy was identified as the most catalytically active and was therefore selected for the subsequent adsorption studies. For the ionic liquid (IL) systems, we constructed molecular models of 1-ethyl-3-methylimidazolium acetate ([EMIM][OAc]) and 1-ethyl-3-methylimidazolium trifluoroacetate ([EMIM][TFA]). Initial adsorption geometries were systematically explored by placing the ILs at various positions and orientations relative to the S-vacancy site, with a minimum of 5 distinct initial configurations tested for each system to ensure thorough sampling of the configuration space. For each IL, we examined configurations with: (i) the imidazolium ring parallel to the MoS_2 surface, (ii) the imidazolium ring perpendicular to the surface, (iii) the anion positioned directly above the vacancy, and (iv) combined ion pairs in different orientations. For the CO_2 adsorption studies, we similarly tested multiple adsorption sites and orientations, including configurations with the CO_2 molecule aligned parallel or perpendicular to the surface, and positioned at various distances from both the S-vacancy and the ionic liquid components.

The adsorption energies (E_{ads}) for the multi-component systems were calculated using a stepwise approach. First, the IL adsorption energy on the defective MoS_2 substrate was calculated as

$$E_{ads}(IL) = E(MoS_2 - def + IL) - E(MoS_2 - def) - E(IL), \quad (5.2)$$

where E(MoS_2-def+IL) is the total energy of the IL-adsorbed system, E(MoS_2-def) is the energy of the isolated defective MoS_2 substrate, and E(IL) is the energy of the isolated IL. Subsequently, the CO_2 adsorption energy in the presence of ILs was calculated as

$$E_{ads}(CO_2) = E(MoS_2 - def + IL + CO_2) - E(MoS_2 - def + IL) - E(CO_2), \quad (5.3)$$

where E(MoS_2-def+IL+CO_2) represents the total energy of the complete system. This decomposition allowed us to separately quantify the energetic contributions from each component. To analyze the electronic properties and understand the mechanisms governing the different binding behaviors, we calculated partial charge densities, projected density of states (PDOS), and performed Bader charge analysis [40, 41]. The charge density difference ($\Delta\rho$) was evaluated as:

$$\Delta\rho = \rho(MoS_2 - def + IL + CO_2) - \rho(MoS_2 - def + IL) - \rho(CO_2), \quad (5.4)$$

where ρ represents the electronic charge density.

5.3. Results and discussion

5.3.1. CO_2 with different imidazolium acetates

The catalyst material for the CO_2RR was as-purchased MoS_2 nanopowder (Sigma Aldrich, average particle size of 90 nm). It was the same

nanopowder as was used in the previous works, where, the presence of the sulfur vacancies was established through the presence of under-coordinated molybdenum sites in the Mo 3d5 spectrum by XPS and the downshift of the A^1_{2g} peak in the Raman spectrum (see chapter 3). Figure 5.2 (a) shows an SEM image of the catalyst material, while Figure 5.2 (b) shows an EDS map of it. The SEM image and the EDS map show

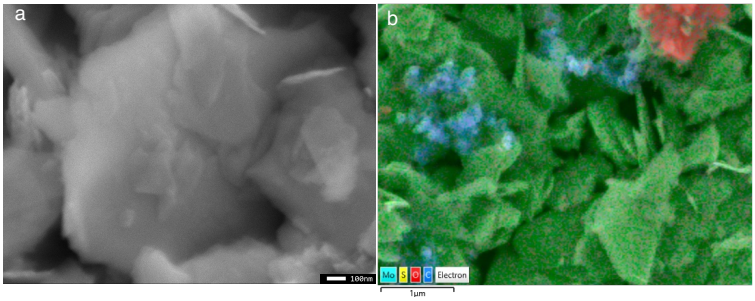

Figure 5.2. **(a)** SEM image taken of the MoS_2 nanopowder showing the exposed basal planes on the surface of the electrode. **(b)** EDS map taken of the electrode showing the chemical composition of the electrode surface.

that on the surface of the electrode, mainly the basal planes of MoS_2 catalyst are exposed, whereas the sulfur vacancies are present in the MoS_2 structure. Hence, if the basal plane is activated by the sulfur vacancies, then the product distribution of the CO_2RR should shift towards higher hydrocarbons, based on the calculations of Kang et al. [19]. The EDS mapping also shows a slight oxidation of the MoS_2, which is consistent with the Mo^{6+} phases identified through XPS in chapter 3.

For the investigation of the electrochemical activity towards the CO_2RR of the V_S-MoS_2 with the two different co-catalysts, a three-electrode setup was used. Figure 5.3 (a) shows the linear sweep voltammetry curves when the two different co-catalysts are present in the electrochemical cell. The figure shows that when the [EMIM][TFA] co-catalyst is applied, there is a distinguishable reduction well between ∼-0.3 V vs RHE and ∼-0.7 V vs RHE compared to the case where the [EMIM][OAc] is used as co-catalyst.

Therefore, this potential window was explored to see the electrochemical activity of the system towards the CO_2RR in 0.1 V intervals. Figure 5.3 (b) shows the product distribution regarding Faradaic efficiency in the potential window when the two different co-catalysts are used (for FE calculations, see Appendix B). In both cases a mixture of hydrocarbons (C_xH_y) and H_2 was also detected in different amounts. At the two edges of the potential window for both cases the HER is dominating the CO_2RR, however, in the middle of the production window, the production of

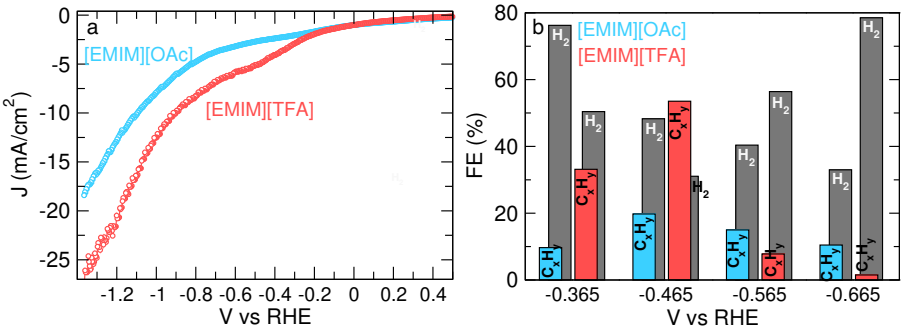

Figure 5.3. **(a)** LSV curves of the electrochemical systems when [EMIM][OAc] is used as a co-catalyst (blue) and when [EMIM][TFA] is applied as a co-catalyst (red). **(b)** FEs of the two different systems in the potential window of -0.3 V vs RHE and -0.7 V vs RHE.

hydrocarbons increased and the H_2 production decreased. Specifically, at -0.465 V vs RHE when the [EMIM][TFA] is used as co-catalyst, the hydrocarbon production (∼53.54%) is significantly higher than the H_2 production (∼31.06%).

Figure 5.4 shows the component breakdown of the hydrocarbon mixtures measured during the electrochemical CO_2RR. The most significant

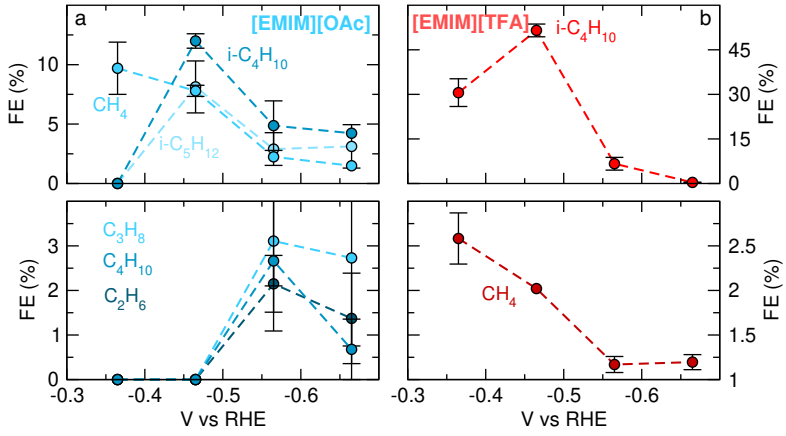

Figure 5.4. FE of the different components in the hydrocarbon mixtures at different potentials with regards to which co-catalyst is used.

difference in the effects of the two co-catalysts is on the selectivity of the CO_2RR. When [EMIM][TFA] is used as a co-catalyst, there are only two types of hydrocarbons detected, namely isobutane (i-C_4H_{10}) and methane (CH_4). However, when co-catalyst is changed to [EMIM][OAc], the selectivity of the CO_2RR becomes poor and there were six different hydrocarbon products detected, namely CH_4, ethane (C_2H_6), propane (C_3H_8), butane (C_4H_{10}) and i-C_4H_{10}, and isopentane (i-C_5H_{12}). For both co-catalysts, the optimum voltage - for which the hydrocarbons are produced in the highest amounts - for CO_2RR is at -0.465 V vs RHE, and in the case of the [EMIM][TFA], the CO_2RR can dominate the HER. Furthermore, it is worth noting that even though the selectivity of the CO_2RR is poor in the case of the [EMIM][OAc] co-catalyst, i-C_4H_{10} is still the dominant product for both co-catalysts.

5.3.2. DFT Analysis

Contrasting Adsorption Mechanisms of Ionic Liquids on Defective MoS_2

The reason behind the significantly different selectivities of the CO_2RR with the two different co-catalysts was studied with DFT. The adsorption of [EMIM][OAc] and [EMIM][TFA] on S-defective MoS_2 revealed significant differences in binding configurations and energetics despite their structural similarities. For [EMIM][OAc], the most stable configuration involves the acetate anion positioned directly above the S-vacancy with an adsorption energy of -3.57 eV (see Table C.1). The acetate forms strong coordinate bonds with three Mo atoms surrounding the vacancy site, with average O-Mo distances of 2.12 Å. The $[EMIM]^+$ cation adopts a tilted orientation with respect to the surface plane, primarily interacting through non-covalent π-stacking between the imidazolium ring and the intact regions of the MoS_2 surface as it is shown in Figure 5.5 (a). This configuration maximizes both the electrostatic interaction between the acetate and the electron-deficient vacancy site and the dispersion interactions between the imidazolium ring and the surface.

In contrast, [EMIM][TFA] exhibits stronger binding to the S-vacancy site, with an adsorption energy of -3.85 eV (see Table C.2). The most energetically favorable configuration still involves the anion positioned above the S-vacancy, but the trifluoroacetate forms notably longer and weaker bonds with the Mo atoms (average O-Mo distances of 2.31 Å). The increased bond lengths can be attributed to the electron-withdrawing effect of the trifluoromethyl group, which reduces the electron density on the carboxylate oxygen atoms and weakens their interaction with the electron-deficient Mo atoms at the vacancy site. The $[EMIM]]^+$ cation adopts a more planar orientation relative to the surface compared to the [EMIM][OAc] system, maximizing dispersion interactions (see Figure 5.5 (c)). These findings are consistent with previous experimental observations that suggested different surface interactions for fluorinated ionic liquids

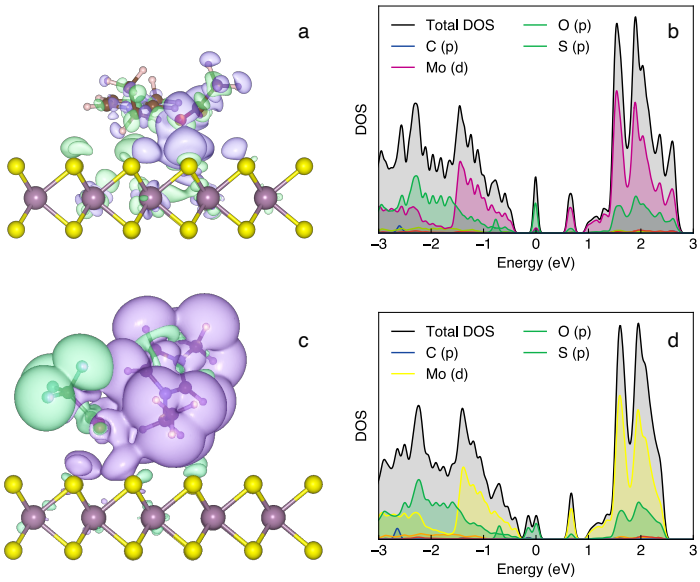

Figure 5.5. **(a)** and **(c)** Charge transfer density distribution and **(b)** and **(d)** PDOS of the MoS_2-[EMIM][OAc] and MoS_2-[EMIM][TFA] systems.

[42, 43]. Bader charge analysis reveals substantial electron transfer from the MoS_2 substrate to the [EMIM][OAc] ionic liquid (0.72 e), while the charge transfer is significantly less pronounced for [EMIM][TFA] (0.38 e). This differential charge transfer further supports the different interaction patterns between the ionic liquids and the defective MoS_2 surface. The PDOS analysis (Figures 5.5 (b) & (d)) shows that the acetate anion creates new hybridized states near the Fermi level through strong interaction with the Mo d-orbitals, while the trifluoroacetate anion exhibits less pronounced hybridization, maintaining electronic states that more closely resemble those of the isolated anion.

CO_2 Binding Mechanisms (Chemical versus Physical Absorption)

To establish a benchmark for CO_2 interactions with the catalyst, we first examined the direct interaction between CO_2 and the S-deficient MoS_2 surface without any ionic liquid present. The charge transfer density distribution shows strong localization around the Mo-S bonds and a distinct electronic restructuring at the CO_2 adsorption site, as shown in Figure 5.6 (a). The charge density difference analysis demonstrates a moderate charge transfer between the CO_2 molecule and the S-vacancy site of the MoS_2, consistent with the calculated adsorption energy of -0.37 eV.

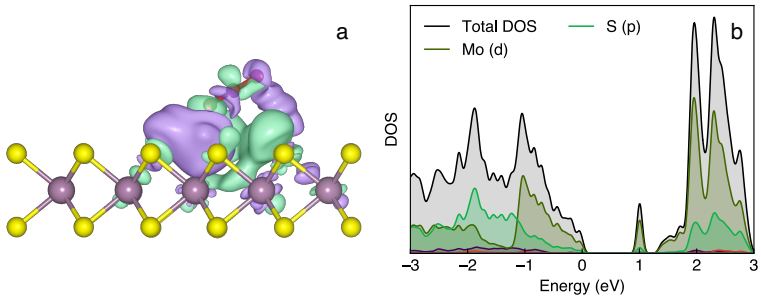

Figure 5.6. **(a)** Charge transfer density distribution and **(b)** PDOS of the MoS_2-CO_2 system

This energy range suggests an optimal binding strength that facilitates CO_2 activation without complete molecular dissociation. Therefore, the localized nature of these electronic interactions suggests that the S-vacancies serve as isolated catalytic sites, while maintaining the overall electronic structure of the MoS_2. This -0.37 eV adsorption energy of the CO_2 is a relatively weak binding, suggesting physisorption rather than chemisorption and this weak binding implies that the CO_2 may not be effectively activated by the defect site alone.

The interaction of CO_2 with the IL-MoS_2 systems exhibited distinctly different characteristics based on anion composition. For the [EMIM][OAc]-MoS_2 system, our calculations reveal that CO_2 undergoes chemical coordination with the acetate anion, forming a carboxylate-CO_2 complex rather than interacting directly with the MoS_2 substrate. Analysis of the optimized geometry shows that this chemical coordination substantially restructures the CO_2 molecule from its linear gas-phase configuration. The O-C-O bond angle contracts significantly from 180° to 133.2°, while the C-O bond distances elongate from 1.16 Å to an average of 1.24 Å. This geometric transformation indicates the formation of a carbonate-like intermediate structure. The calculated adsorption energy for this chemical coordination process is -1.42 eV, indicating a thermodynamically favorable interaction. Bader charge analysis confirms substantial electron transfer to the CO_2 molecule (0.61 e), primarily from the acetate anion rather than from the MoS_2 substrate. This charge transfer populates the antibonding orbitals of CO_2, resulting in the observed bond elongation and angle bending. Electronic projected density of state analysis reveals new hybridized states between the acetate and CO_2 molecular orbitals, providing further evidence for chemical bond formation. The strong chemical interaction effectively activates the CO_2 molecule but

simultaneously reduces its mobility, which may explain the experimentally observed lower absorption and desorption rates for this system.

In contrast, CO_2 interaction with the [EMIM][TFA]-MoS_2 system exhibits characteristics of physical absorption. The CO_2 molecule remains essentially linear (O-C-O angle of 178.3°) with minimal bond elongation (average C-O bond length of 1.17 Å). The molecule adopts a configuration where it interacts simultaneously with both the trifluoroacetate anion and the S-vacancy site on the MoS_2 surface, with an adsorption energy of -0.58 eV. This dual-site interaction creates a unique adsorption environment that facilitates CO_2 transport while maintaining sufficient binding to enable catalytic conversion. The weaker physical absorption in the [EMIM][TFA] system is accompanied by minimal charge transfer to the CO_2 molecule (0.14 e), consistent with the preservation of its linear geometry. Projected density of state analysis shows only slight perturbations to the CO_2 molecular orbitals, with no significant formation of new hybridized states. The charge density difference clearly visualizes these contrasting binding mechanisms, showing localized regions of charge accumulation between the acetate and CO_2 in the [EMIM][OAc] system, indicative of covalent bond formation, versus more diffuse and weaker polarization patterns in the [EMIM][TFA] system characteristic of physical interactions.

Mechanism of Enhanced Catalytic Activity in the [EMIM][TFA] System

Our computational results provide a molecular-level explanation for the experimentally observed enhanced catalytic activity of the [EMIM][TFA]-MoS_2 system compared to [EMIM][OAc]-MoS_2. The key factor appears to be the optimal balance between CO_2 activation and mobility achieved in the [EMIM][TFA] system. While the [EMIM][OAc] system more effectively activates CO_2 through chemical binding, the strong interaction simultaneously impedes CO_2 transport to the catalytically active sites on the MoS_2 surface. The [EMIM][TFA] system, with its weaker physical absorption, maintains sufficient CO_2 mobility to facilitate rapid transport to the MoS_2 catalyst surface, where the actual reduction reaction occurs. The charge density analysis of the MoS_2 surface with adsorbed [EMIM][TFA] reveals that the S-vacancy sites maintain their electron-deficient character despite the presence of the ionic liquid. These sites remain accessible to CO_2 molecules and can participate in catalytic reactions. In contrast, the [EMIM][OAc] interaction with the MoS_2 surface partially passivates the catalytically active vacancy sites through stronger binding and greater charge transfer, reducing their availability for direct CO_2 activation.

5.3.3. Surface analysis of exposed electrodes

To gain insights into the surface chemistry of the V_S-MoS_2-based electrodes and to support the predictions from our DFT calculations, XPS analysis was performed on a set of exposed samples. Four electrodes were

measured which were subjected to distinct conditions: (1) the V_S-MoS_2 electrode exposed only to the [EMIM][OAc]; (2) the V_S-MoS_2 electrode exposed to [EMIM][OAc] with CO_2 bubbled through the system; (3) the V_S-MoS_2 electrode exposed only to [EMIM][TFA]; and (4) the V_S-MoS_2 electrode exposed to [EMIM][TFA] with CO_2 bubbled. These conditions were chosen to investigate the specific chemical interactions between V_S-MoS_2, the ionic liquids, and CO_2. Figure 5.7 (a) and (b) presents the fitted high-resolution C 1s and Mo 3d spectra, respectively, for all four systems, highlighting the chemical state changes across the different environments.

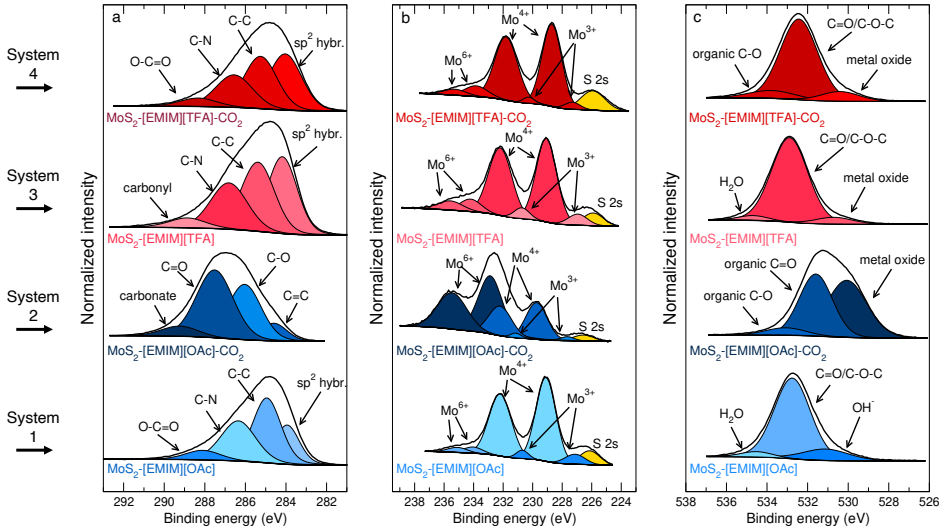

Figure 5.7. **(a)** C 1s, **(b)** Mo 3d and **(c)** O 1s spectra of V_S-MoS_2 electrodes exposed to different environments.

In the fitted C 1s spectra, three of the four systems , namely 1, 3, and 4, exhibited similar chemical characteristics. Specifically, these systems showed an sp^2-hybridized carbon peak at ~284 eV [44] and a C–N bonding feature around ~286.5 eV [45], both of which are consistent with the presence of the imidazolium cation. Additionally, aromatic carbon was detected in systems 3 and 4 at around ~285.3 eV, while O–C=O bonding, indicative of carboxylate-type environments, appeared in systems 1 and 4 near ~288.2 eV [46, 47]. A distinct carbonyl peak at ~289 eV was uniquely observed in system 3 [47]. In contrast, system 2, where the V_S-MoS_2 electrode was exposed to [EMIM][OAc] under CO_2 flow, presented a markedly different chemical composition. The spectrum revealed peaks corresponding to C=C bonding at ~284.6 eV, C–O bonding at ~286 eV, C=O bonding at ~287.5 eV, and a carbonate species at ~289.2 eV [46,

47]. These findings suggest that different surface-bound complexes were formed depending on the exposure conditions. In systems 1, 3, and 4, the presence of sp^2-hybridized carbon and C–N bonding supports the adsorption of the ionic liquid's anion and cation on the electrode surface. In system 2, however, the spectral features are more consistent with a CO_2-derived carbonate complex, likely involving anion of the ionic liquid and CO_2, as predicted by our DFT calculations.

The Mo 3d spectra revealed the presence of three distinct molybdenum oxidation states across the samples. A Mo^{3+} component was identified at approximately 227.5 eV, corresponding to undercoordinated Mo surface sites [48, 49], with a possible Mo–N interaction appearing as a subtle feature near 228 eV [50, 51]. The dominant Mo^{4+} peak, centered at around 229.4 eV, is attributed to the V_S-MoS_2 lattice [52, 53], while a Mo^{6+} contribution at approximately 232.4 eV indicates partial surface oxidation [54]. A similar trend to that observed in the C 1s spectra emerges: systems 1, 3, and 4 display comparable behavior, with Mo^{4+} as the major spectral component. In contrast, system 2, where V_S-MoS_2 was exposed to [EMIM][OAc] and CO_2, shows a significant shift toward Mo^{6+}, suggesting a higher degree of surface oxidation under these conditions.

The C 1s and Mo 3d spectra are further complemented by the fitting of the O 1s spectra, providing a more complete picture of the surface chemistry across the four systems. In systems 1, 3, and 4, the dominant O 1s contribution originates from surface-adsorbed C=O and C–O–C species, centered around ∼532.7 eV, which are consistent with organic oxygen functionalities derived from the ionic liquid components [46]. In system 1, aside from this main feature, only minor signals corresponding to surface-adsorbed water (at approximately ∼534.5 eV [55]) and hydroxyl groups (at ∼531.1 eV [55]) are observed. System 3, in addition to the organic oxygen signal, also shows features attributable to surface-adsorbed water and a small contribution from metal oxides at around ∼530 eV. In system 4, the spectrum includes organic C–O bonding (at ∼533.7 eV) and a minor metal oxide component [46, 47]. In contrast, system 2 presents a markedly different O 1s spectrum, dominated by a pronounced metal oxide peak near 530 eV, which aligns with the Mo^{6+} oxidation state observed in the Mo 3d region [55]. This is accompanied by features assigned to organic C=O and C–O groups, similar to the other systems. These findings support and reinforce the conclusions drawn from our DFT calculations: namely, that in system 2, the interaction between CO_2 and the ionic liquid is significantly stronger, leading to decreased Faradaic efficiency for CO_2 reduction and potentially contributing to the oxidation of the V_S-MoS_2 catalyst surface.

5.4. Conclusions

In this chapter, we investigated two imidazolium-based ionic liquids, [EMIM][OAc] and [EMIM][TFA], as co-catalysts for the electrochemical CO_2 reduction reaction (CO_2RR) using a V_S-MoS_2 catalyst. Strikingly different product distributions were observed depending on the ionic liquid employed: when [EMIM][OAc] was used, a broad spectrum of six distinct CO_2RR products was detected, each in relatively low yield. In contrast, the use of [EMIM][TFA] resulted in the formation of only two products, with one dominating the overall distribution. To understand the origin of this selectivity shift, DFT calculations were performed, which revealed that [EMIM][OAc] interacts much more strongly with CO_2 than [EMIM][TFA], as the [EMIM][TFA] creates a balance between the activation and the mass transfer of the CO_2. These computational insights were supported by XPS measurements of the exposed V_S-MoS_2 electrodes, which showed chemical signatures consistent with strong CO_2–[EMIM][OAc] interactions. Overall, this study demonstrates that the selectivity of the CO_2RR is governed not only by the interaction between CO_2 and the catalyst surface, but also by the nature of the co-catalyst. Thus, careful selection and molecular design of the co-catalyst are essential for tuning the reaction pathway and engineering product selectivity.

references

[1] M. R. McCrystall, J. Stroeve, M. Serreze, B. C. Forbes, and J. A. Screen. "New climate models reveal faster and larger increases in Arctic precipitation than previously projected". In: *Nature Communications* 12.1 (2021). DOI: 10.1038/s41467-021-27031-y. URL: https://doi.org/10.1038%2Fs41467-021-27031-y.

[2] D. McCollum, N. Bauer, K. Calvin, A. Kitous, and K. Riahi. "Fossil resource and energy security dynamics in conventional and carbon-constrained worlds". In: *Climatic Change* 123.3-4 (2013), pp. 413–426. DOI: 10.1007/s10584-013-0939-5. URL: https://doi.org/10.1007%2Fs10584-013-0939-5.

[3] S. J. Davis, K. Caldeira, and H. D. Matthews. "Future CO_2 Emissions and Climate Change from Existing Energy Infrastructure". In: *Science* 329.5997 (2010), pp. 1330–1333. DOI: 10.1126/science.1188566. URL: https://doi.org/10.1126%2Fscience.1188566.

[4] S. Nitopi, E. Bertheussen, S. B. Scott, X. Liu, A. K. Engstfeld, S. Horch, B. Seger, I. E. L. Stephens, K. Chan, C. Hahn, J. K. Nørskov, T. F. Jaramillo, and I. Chorkendorff. "Progress and Perspectives of Electrochemical CO2 Reduction on Copper in Aqueous Electrolyte". In: *Chemical Reviews* 119.12 (2019). PMID: 31117420, pp. 7610–7672. DOI: 10.1021/acs.chemrev.8b00705. eprint: https://doi.org/10.1021/acs.chemrev.8b00705. URL: https://doi.org/10.1021/acs.chemrev.8b00705.

[5] Y. Hori. "Electrochemical CO2 Reduction on Metal Electrodes". In: *Modern Aspects of Electrochemistry*. Ed. by C. G. Vayenas, R. E. White, and M. E. Gamboa-Aldeco. New York, NY: Springer New York, 2008, pp. 89–189. ISBN: 978-0-387-49489-0. DOI: 10.1007/978-0-387-49489-0_3. URL: https://doi.org/10.1007/978-0-387-49489-0_3.

[6] Z. Sun, T. Ma, H. Tao, Q. Fan, and B. Han. "Fundamentals and Challenges of Electrochemical CO2 Reduction Using Two-Dimensional Materials". In: *Chem* 3.4 (Oct. 2017), pp. 560–587. ISSN: 2451-9294. DOI: 10.1016/j.chempr.2017.09.009. URL: http://dx.doi.org/10.1016/j.chempr.2017.09.009.

[7] J. Wu, Y. Huang, W. Ye, and Y. Li. "CO2 Reduction: From the Electrochemical to Photochemical Approach". In: *Advanced Science* 4.11 (Sept. 2017). ISSN: 2198-3844. DOI: 10.1002/advs.201700194. URL: http://dx.doi.org/10.1002/advs.201700194.

[8] S. Liu, H. Yang, X. Huang, L. Liu, W. Cai, J. Gao, X. Li, T. Zhang, Y. Huang, and B. Liu. "Identifying active sites of nitrogen-doped carbon materials for the CO2 reduction reaction". In: *Advanced Functional Materials* 28.21 (2018), p. 1800499.

[9] W. Bi, X. Li, R. You, M. Chen, R. Yuan, W. Huang, X. Wu, W. Chu, C. Wu, and Y. Xie. "Surface immobilization of transition metal ions on nitrogen-doped graphene realizing high-efficient and selective CO2 reduction". In: *Advanced Materials* 30.18 (2018), p. 1706617.

[10] J. Liu, D. Yang, Y. Zhou, G. Zhang, G. Xing, Y. Liu, Y. Ma, O. Terasaki, S. Yang, and L. Chen. "Tricycloquinazoline-based 2D conductive metal–organic frameworks as promising electrocatalysts for CO2 reduction". In: *Angewandte Chemie International Edition* 60.26 (2021), pp. 14473–14479.

[11] M. K. Lee, M. Shokouhimehr, S. Y. Kim, and H. W. Jang. "Two-dimensional metal–organic frameworks and covalent–organic frameworks for electrocatalysis: distinct merits by the reduced dimension". In: *Advanced Energy Materials* 12.4 (2022), p. 2003990.

[12] P. Abbasi, M. Asadi, C. Liu, S. Sharifi-Asl, B. Sayahpour, A. Behranginia, P. Zapol, R. Shahbazian-Yassar, L. A. Curtiss, and A. Salehi-Khojin. "Tailoring the Edge Structure of Molybdenum Disulfide toward Electrocatalytic Reduction of Carbon Dioxide". In: *ACS Nano* 11.1 (2016), pp. 453–460. DOI: 10.1021/acsnano.6b06392. URL: https://doi.org/10.1021%2Facsnano.6b06392.

[13] M. Asadi, B. Kumar, A. Behranginia, B. A. Rosen, A. Baskin, N. Repnin, D. Pisasale, P. Phillips, W. Zhu, R. Haasch, R. F. Klie, P. Král, J. Abiade, and A. Salehi-Khojin. "Robust carbon dioxide reduction on molybdenum disulphide edges". In: *Nature Communications* 5.1 (2014). DOI: 10.1038/ncomms5470. URL: https://doi.org/10.1038%2Fncomms5470.

[14] M. Asadi, K. Kim, C. Liu, A. V. Addepalli, P. Abbasi, P. Yasaei, P. Phillips, A. Behranginia, J. M. Cerrato, R. Haasch, P. Zapol, B. Kumar, R. F. Klie, J. Abiade, L. A. Curtiss, and A. Salehi-Khojin. "Nanostructured transition metal dichalcogenide electrocatalysts for CO_2 reduction in ionic liquid". In: *Science* 353.6298 (2016), pp. 467–470. DOI: 10.1126/science.aaf4767. URL: https://doi.org/10.1126%2Fscience.aaf4767.

[15] S. A. Francis, J. M. Velazquez, I. M. Ferrer, D. A. Torelli, D. Guevarra, M. T. McDowell, K. Sun, X. Zhou, F. H. Saadi, J. John, M. H. Richter, F. P. Hyler, K. M. Papadantonakis, B. S. Brunschwig, and N. S. Lewis. "Reduction of Aqueous CO2 to 1-Propanol at MoS2 Electrodes". In: *Chemistry of Materials* 30.15 (2018), pp. 4902–4908. DOI: 10.1021/acs.chemmater.7b04428.

eprint: https://doi.org/10.1021/acs.chemmater.7b04428. URL: https://doi.org/10.1021/acs.chemmater.7b04428.

[16] H. Wang, X. Xiao, S. Liu, C.-L. Chiang, X. Kuai, C.-K. Peng, Y.-C. Lin, X. Meng, J. Zhao, J. Choi, Y.-G. Lin, J.-M. Lee, and L. Gao. "Structural and Electronic Optimization of MoS2 Edges for Hydrogen Evolution". In: *Journal of the American Chemical Society* 141.46 (2019). PMID: 31692351, pp. 18578–18584. DOI: 10.1021/jacs.9b09932. URL: https://doi.org/10.1021/jacs.9b09932.

[17] Y. Shi, Y. Zhou, D.-R. Yang, W.-X. Xu, C. Wang, F.-B. Wang, J.-J. Xu, X.-H. Xia, and H.-Y. Chen. "Energy Level Engineering of MoS2 by Transition-Metal Doping for Accelerating Hydrogen Evolution Reaction". In: *Journal of the American Chemical Society* 139.43 (Oct. 2017), pp. 15479–15485. ISSN: 1520-5126. DOI: 10.1021/jacs.7b08881. URL: http://dx.doi.org/10.1021/jacs.7b08881.

[18] Y. Yu, S.-Y. Huang, Y. Li, S. N. Steinmann, W. Yang, and L. Cao. "Layer-Dependent Electrocatalysis of MoS2 for Hydrogen Evolution". In: *Nano Letters* 14.2 (2014). PMID: 24397410, pp. 553–558. DOI: 10.1021/nl403620g. URL: https://doi.org/10.1021/nl403620g.

[19] S. Kang, S. Han, and Y. Kang. "Unveiling Electrochemical Reaction Pathways of CO2 Reduction to CN Species at S-Vacancies of MoS2". In: *ChemSusChem* 12.12 (May 2019), pp. 2671–2678. ISSN: 1864-564X. DOI: 10.1002/cssc.201900779. URL: http://dx.doi.org/10.1002/cssc.201900779.

[20] S. Kang, S. Ju, S. Han, and Y. Kang. "Computational Identification of Transition-Metal Dichalcogenides for Electrochemical CO2 Reduction to Highly Reduced Species Beyond CO and HCOOH". In: *The Journal of Physical Chemistry C* 124.47 (Nov. 2020), pp. 25812–25820. ISSN: 1932-7455. DOI: 10.1021/acs.jpcc.0c07113. URL: http://dx.doi.org/10.1021/acs.jpcc.0c07113.

[21] Y. Ji, J. K. Nørskov, and K. Chan. "Scaling Relations on Basal Plane Vacancies of Transition Metal Dichalcogenides for CO2 Reduction". In: *The Journal of Physical Chemistry C* 123.7 (Jan. 2019), pp. 4256–4261. ISSN: 1932-7455. DOI: 10.1021/acs.jpcc.8b11628. URL: http://dx.doi.org/10.1021/acs.jpcc.8b11628.

[22] C. B. Roxlo, H. W. Deckman, J. Gland, S. D. Cameron, and R. R. Chianelli. "Edge Surfaces in Lithographically Textured Molybdenum Disulfide". In: *Science* 235.4796 (Mar. 1987), pp. 1629–1631. ISSN: 1095-9203. DOI: 10.1126/science.235.4796.1629. URL: http://dx.doi.org/10.1126/science.235.4796.1629.

[23] D. Liu, Y. Guo, L. Fang, and J. Robertson. "Sulfur vacancies in monolayer MoS2 and its electrical contacts". In: *Applied Physics Letters* 103.18 (Oct. 2013). ISSN: 1077-3118. DOI: 10.1063/1.4824893. URL: http://dx.doi.org/10.1063/1.4824893.

[24] M. B. Shiflett, D. J. Kasprzak, C. P. Junk, and A. Yokozeki. "Phase behavior of {carbon dioxide+[bmim][Ac]} mixtures". In: *The Journal of Chemical Thermodynamics* 40.1 (2008), pp. 25–31.

[25] J. D. Watkins and A. B. Bocarsly. "Direct Reduction of Carbon Dioxide to Formate in High-Gas-Capacity Ionic Liquids at Post-Transition-Metal Electrodes". In: *ChemSusChem* 7.1 (2014), pp. 284–290.

[26] A. Datar, M. Bar-Sadan, and A. Ramasubramaniam. "Interactions between transition-metal surfaces and MoS2 monolayers: Implications for hydrogen evolution and CO2 reduction reactions". In: *The Journal of Physical Chemistry C* 124.37 (2020), pp. 20116–20124.

[27] Y. Liu, J. Sun, H. Huang, L. Bai, X. Zhao, B. Qu, L. Xiong, F. Bai, J. Tang, and L. Jing. "Improving CO_2 photoconversion with ionic liquid and Co single atoms". In: *Nature Communications* 14 (2023), p. 1457. DOI: 10.1038/s41467-023-36980-5.

[28] X.-R. Qin, J.-J. Li, L.-L. Wang, H. Liu, Z.-T. Yang, G.-J. Feng, X.-R. Wang, X.-X. Cheng, C. Zhang, Z.-Y. Yu, and T.-B. Lu. "Electroreduction of diluted CO_2 to multicarbon products with high carbon utilization at 800 mA cm^{-2} in strongly acidic media". In: *Nature Communications* 16 (2025), p. 4447. DOI: 10.1038/s41467-025-59783-2.

[29] M. B. Shiflett and A. Yokozeki. "Phase behavior of carbon dioxide in ionic liquids:[emim][acetate],[emim][trifluoroacetate], and [emim][acetate]+[emim][trifluoroacetate] mixtures". In: *Journal of Chemical & Engineering Data* 54.1 (2009), pp. 108–114.

[30] G. Kresse and J. Furthmüller. "Efficient iterative schemes for ab initio total-energy calculations using a plane-wave basis set". In: *Physical review B* 54.16 (1996), p. 11169.

[31] G. Kresse and D. Joubert. "From ultrasoft pseudopotentials to the projector augmented-wave method". In: *Physical review b* 59.3 (1999), p. 1758.

[32] P. E. Blöchl. "Projector augmented-wave method". In: *Physical review B* 50.24 (1994), p. 17953.

[33] J. Hafner. "Ab-initio simulations of materials using VASP: Density-functional theory and beyond". In: *Journal of computational chemistry* 29.13 (2008), pp. 2044–2078.

[34] J. P. Perdew, K. Burke, and M. Ernzerhof. "Generalized gradient approximation made simple". In: *Physical review letters* 77.18 (1996), p. 3865.

[35] S. Grimme, S. Ehrlich, and L. Goerigk. "Effect of the damping function in dispersion corrected density functional theory". In: *Journal of computational chemistry* 32.7 (2011), pp. 1456–1465.

[36] X. Zhang, Z. Lei, B. Hu, X. Zhang, W. Fan, L. Zhao, and H. Luo. "Insights into CO_2 absorption mechanisms in ionic liquid solutions by integrating experimental and computational studies". In: *ACS Applied Materials & Interfaces* 12 (2020), pp. 47420–47429. DOI: 10.1021/acsami.0c16496.

[37] C. R. C. Rêgo, P. Tereshchuk, L. F. N. Oliveira, and J. L. F. Da Silva. "Unraveling the energetics of site-specific adsorption of molecules on two-dimensional MoS_2". In: *Physical Chemistry Chemical Physics* 21 (2019), pp. 23076–23089. DOI: 10.1039/C9CP04253C.

[38] H. Li, C. Tsai, A. L. Koh, L. Cai, A. W. Contryman, A. H. Fragapane, J. Zhao, H. S. Han, H. C. Manoharan, F. Abild-Pedersen, *et al.* "Activating and optimizing MoS2 basal planes for hydrogen evolution through the formation of strained sulphur vacancies". In: *Nature materials* 15.1 (2016), pp. 48–53.

[39] C. Tsai, K. Chan, J. K. Nørskov, and F. Abild-Pedersen. "Rational design of MoS 2 catalysts: tuning the structure and activity via transition metal doping". In: *Catalysis Science & Technology* 5.1 (2015), pp. 246–253.

[40] R. F. W. Bader. *Atoms in Molecules: A Quantum Theory*. Oxford, U.K.: Oxford University Press, 1990. ISBN: 9780470210444.

[41] G. Henkelman, A. Arnaldsson, and H. Jónsson. "A fast and robust algorithm for Bader decomposition of charge density". In: *Computational Materials Science* 36.3 (2006), pp. 354–360.

[42] M. Mezger, H. Schroder, H. Reichert, S. Schramm, J. S. Okasinski, S. Schoder, V. Honkimaki, M. Deutsch, B. M. Ocko, J. Ralston, *et al.* "Molecular layering of fluorinated ionic liquids at a charged sapphire (0001) surface". In: *Science* 322.5900 (2008), pp. 424–428.

[43] A. S. Pensado, F. Malberg, M. C. Gomes, A. A. Padua, J. Fernández, and B. Kirchner. "Interactions and structure of ionic liquids on graphene and carbon nanotubes surfaces". In: *RSC advances* 4.35 (2014), pp. 18017–18024.

[44] S. T. Jackson and R. G. Nuzzo. "Determining hybridization differences for amorphous carbon from the XPS C 1s envelope". In: *Applied Surface Science* 90.2 (1995), pp. 195–203.

[45] M. Baker and P. Hammer. "A Study of the Chemical Bonding and Microstructure of Ion Beam-deposited CNx Films Including an XPS C 1s Peak Simulation". In: *Surface and Interface Analysis: An International Journal devoted to the development and application of techniques for the analysis of surfaces, interfaces and thin films* 25.9 (1997), pp. 629–642.

[46] G. P. López, D. G. Castner, and B. D. Ratner. "XPS O 1s binding energies for polymers containing hydroxyl, ether, ketone and ester groups". In: *Surface and interface analysis* 17.5 (1991), pp. 267–272.

[47] A. Dolgov, D. Lopaev, C. Lee, E. Zoethout, V. Medvedev, O. Yakushev, and F. Bijkerk. "Characterization of carbon contamination under ion and hot atom bombardment in a tin-plasma extreme ultraviolet light source". In: *Applied surface science* 353 (2015), pp. 708–713.

[48] X. Zhang, S. Wang, C.-K. Lee, C.-M. Cheng, J.-C. Lan, X. Li, J. Qiao, and X. Tao. "Unravelling the effect of sulfur vacancies on the electronic structure of the MoS_2 crystal". In: *Physical Chemistry Chemical Physics* 22.38 (2020), pp. 21776–21783. ISSN: 1463-9084. DOI: 10.1039/c9cp07004d.

[49] H. Fei, R. Liu, J. Wang, T. Guo, Z. Wu, D. Wang, and F. Liu. "Targeted Modulation of Competitive Active Sites toward Nitrogen Fixation via Sulfur Vacancy Engineering Over MoS_2". In: *Advanced Functional Materials* 33.36 (2023). ISSN: 1616-3028. DOI: 10.1002/adfm.202302501.

[50] C. Wang, X. Li, H. Song, P. K. Chu, and K. Huo. "In-Plane Heterostructured MoN/MoC Nanosheets with Enhanced Interfacial Charge Transfer for Superior Pseudocapacitive Storage". In: *Advanced Functional Materials* 34.12 (2024), p. 2311040.

[51] H. Wu and K. Lian. "The development of pseudocapacitive molybdenum oxynitride electrodes for supercapacitors". In: *ECS Transactions* 58.25 (2014), p. 67.

[52] W. Li, J. Huang, B. Han, C. Xie, X. Huang, K. Tian, Y. Zeng, Z. Zhao, P. Gao, Y. Zhang, T. Yang, Z. Zhang, S. Sun, and Y. Hou. "Molten-Salt-Assisted Chemical Vapor Deposition Process for Substitutional Doping of Monolayer MoS2 and Effectively Altering the Electronic Structure and Phononic Properties". In: *Advanced Science* 7.16 (July 2020). ISSN: 2198-3844. DOI: 10.1002/advs.202001080. URL: http://dx.doi.org/10.1002/advs.202001080.

[53] X. Wang, X. Shen, Z. Wang, R. Yu, and L. Chen. "Atomic-Scale Clarification of Structural Transition of MoS2 upon Sodium Intercalation". In: *ACS Nano* 8.11 (Nov. 2014), pp. 11394–11400. ISSN: 1936-086X. DOI: 10.1021/nn505501v. URL: http://dx.doi.org/10.1021/nn505501v.

[54] S. Yoon, Q. Huang, Rusli, H. Yang, J. Ahn, Q. Zhang, C. Blomfield, B. Tielsch, and L. Y. Tan. "X-ray photoelectron spectroscopy of molybdenum-containing carbon films". In: *Journal of applied physics* 86.9 (1999), pp. 4871–4875.

[55] J.-C. Dupin, D. Gonbeau, P. Vinatier, and A. Levasseur. "Systematic XPS studies of metal oxides, hydroxides and peroxides". In: *Physical Chemistry Chemical Physics* 2.6 (2000), pp. 1319–1324.

6

Conclusion and recommendations

The research presented in this thesis showed a path and its challenges for the possible application of MoS_2 as an electrocatalyst with different ionic liquid co-catalysts. MoS_2 as a catalyst for CO_2 reduction is a promising candidate due to its structural flexibility and electronic tunability. However, its superior electrocatalytic affinity towards HER hinders these tunable properties from being utilized for CO_2RR, therefore, the presence of a co-catalyst in the form of ionic liquids is inevitable to facilitate the CO_2RR. In this thesis, the effect of the sulfur vacancies in the MoS_2 structure, the role of different co-catalysts and the changed electronic properties of MoS_2 were studied on the selectivity of the CO_2RR. Based on these studies, brief conclusions of the thesis are listed below:

- Activating the basal plane of MoS_2 by inducing sulfur vacancies drives the selectivity of the CO_2RR towards multicarbon products instead of C_1 products. This important finding proved theoretical calculations in the literature and opened up the path to the direct production of higher hydrocarbons via the electrochemical CO_2RR.

- This thesis also showed that the selectivity of the CO_2RR on V_S-MoS_2 catalyst also depends on the used co-catalyst. Selecting the right co-catalyst, which assists the CO_2RR is crucial to engineer the selectivity of the reaction. It was shown that imidazolium-based acetates are working better as co-catalysts than [EMIM][BF_4] due to the absence of harmful side products, such as HF and because of the higher selectivity in the multicarbon products. Furthermore, it was also studied that with [EMIM][TFA] as a co-catalyst, the selectivity of the CO_2RR on V_S-MoS_2 can be tuned towards one single product, isobutane.

- The thesis also showed that the layered structure of MoS_2 provides the opportunity of intercalating different ions in the interlayer space and

through that, tuning its conductivity. Molecular dynamics proved to be a useful tool for studying the intercalation mechanism. Through the simulations, it was shown that the energy barrier of intercalation originates from the deformation of the hydration shell of the ions. When sodium ions are compared to potassium ions, as representatives of light and heavy alkali metal ions, respectively, the ion's inherent relationship with its hydration shell plays a crucial role. It was shown that to overcome the energy barrier of the intercalation, it is necessary to impose an external electric field on the system, which acts as a driving force for the intercalation. The needed strength of the external electric field is, however, different for sodium and potassium due to the different levels of steric hindrance of their respective hydration shells.

- On the macro scale, the effects of intercalation were investigated experimentally on the electronic and structural properties of MoS_2. It was shown through XRD measurements and Raman spectroscopy, that the electrochemical intercalation process creates additional sulfur vacancies in the MoS_2 structure. While XPS measurements showed that the intercalation of the different alkali ions changes the bandgap and increases the electron dopant density in the MoS_2. This value however, is different in the case of the intercalation of sodium and potassium ions due to the presence of empty orbitals in the heavy alkali metals.

- Our measurements proved the hypothesis about the presence of monosulfur vacancies in the MoS_2 structure that leads to multicarbon products during the CO_2RR. However, the changed electronic properties of the MoS_2 electrode through the intercalation of alkali metal ions proved to favor HER over the CO_2RR even in the presence of a co-catalyst.

RECOMMENDATIONS

Scaling up the electrocatalytic process remains a complex and challenging task. MoS_2 has been demonstrated as a promising electrocatalyst due to its affinity for producing multicarbon products and its earth-abundant nature. However, the reaction environment must be carefully tuned, particularly through the introduction of co-catalysts, to enhance CO_2RR activity while suppressing the competing hydrogen evolution reaction (HER).

Although the use of ionic liquids is encouraged due to their green chemistry potential, their large-scale application raises concerns related to user safety (e.g., possible side reactions), environmental impact and cost-efficiency. Hence, the use of inorganic aqueous electrolytes represents a more practical and economically viable alternative. This shift in electrolyte strategy necessitates a redesign of the catalyst to emulate the beneficial roles of ILs: namely, modulating charge distribution at the active site and enabling preferential mass transport of CO_2 molecules and reaction intermediates toward

sulfur vacancies, while simultaneously excluding water molecules from the catalyst surface.

- One strategy to mimic the effect of ILs is the growth of hydrophobic self-assembled monolayers (SAMs) on the MoS_2 catalyst surface. These SAMs are widely studied in MoS_2-based nanoelectronic devices, where they induce controllable *p*- or *n*-type doping effects. Specifically, APTMS ((3-aminopropyl)-triethoxysilane) and OTS (octadecyltrichlorosilane) have shown promising compatibility with MoS_2 monolayers. The introduction of hydrophobic SAMs can enhance interfacial charge separation, repel water molecules, and promote the selective adsorption and conversion of CO_2 and its intermediates, thus supporting CO_2RR even in aqueous electrolytes.
- Chemical vapor deposition and atomic layer deposition (ALD) are highly effective techniques for the synthesis and atomic-scale engineering of MoS_2 monolayers. In addition to growing the catalytic layer itself, these methods can be adapted for the direct deposition of functional coatings, including hydrophobic overlayers, enabling a streamlined fabrication route. Moreover, the catalytic performance of ALD-grown MoS_2 can be tuned through doping with elements such as vanadium (V), titanium (Ti), niobium (Nb), zirconium (Zr), or nitrogen (N), allowing precise modulation of the local charge density and electronic structure at the active sites. This doping strategy plays a dual role: (1) altering the local charge distribution to optimize binding energies and (2) promoting favorable mass transfer dynamics for CO_2 and key intermediates.
- As MoS_2 is a semiconductor, it also presents strong potential in photocatalytic applications. Investigating the photocatalytic and photoelectrocatalytic behavior of MoS_2 could unlock additional opportunities for solar-to-chemical conversion. Furthermore, coupling MoS_2 with co-catalysts such as CdS can lead to synergistic effects that enhance charge separation and light harvesting, ultimately boosting the rate and selectivity of CO_2 conversion under illumination.

A

Appendix to Chapter 3

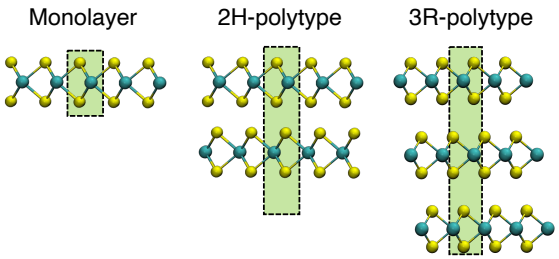

Figure A.1. Schematics of monolayer, 2H-polytype and 3R-polytype of MoS_2 showing the broken (monolayer and 3R) and the restored (2H) inversion symmetry (molybdenum atoms are represented with blue color, sulfur atoms are represented with yellow color).

Electrochemical intercalation

V vs RHE	Meas.	Z_0 (Ohm)	Z (Ohm)	$Z-Z_0$ (Ohm)	Av. (Ohm)	Error
-1.0	1	11680	12688	1007	676	427
	2	10005	10954	948		
	3	8306	8380	73		

V vs RHE	Meas.	Z_0 (Ohm)	Z (Ohm)	$Z-Z_0$ (Ohm)	Av. (Ohm)	Error
-1.1	1	12433	11881	-551	623	832
	2	9411	10685	1273		
	3	8414	9563	1149		

V vs RHE	Meas.	Z_0 (Ohm)	Z (Ohm)	$Z-Z_0$ (Ohm)	Av. (Ohm)	Error
-1.2	1	11402	11039	-363.	262	442
	2	10199	10753	553		
	3	8510	9105	595		

V vs RHE	Meas.	Z_0 (Ohm)	Z (Ohm)	$Z-Z_0$ (Ohm)	Av. (Ohm)	Error
-1.3	1	13207	9936	-3271	-1754	1073
	2	8392	7330	-1062		
	3	8655	7726	-929		

V vs RHE	Meas.	Z_0 (Ohm)	Z (Ohm)	$Z-Z_0$ (Ohm)	Av. (Ohm)	Error
-1.4	1	10267	12224	1957	1253	587
	2	7942	9226	1283		
	3	8593	9113	520		

Table A.1. EIS data of electrochemical sodium intercalation extracted from the Nyquist plots. Z_0 stands for the resistance measured before the electrochemical intercalation, while Z stands for the resistance measured after the intercalation. The difference of Z_0 and Z gives an indication about the success of the intercalation, if the value of $Z-Z_0$ is positive, then the resistance of the electrode increased, if $Z-Z_0$ is negative, then the resistance of the electrode decreased.

A

V vs RHE	Meas.	Z_0 (Ohm)	Z (Ohm)	Z-Z_0 (Ohm)	Average	Error
-1.1	1	5592	5704	111	237	88
	2	5604	5904	299		
	3	5604	5904	300		

V vs RHE	Meas.	Z_0 (Ohm)	Z (Ohm)	Z-Z_0 (Ohm)	Average	Error
-1.2	1	5451	6220	768	392	307
	2	5553	5946	393		
	3	6059	6074	14		

V vs RHE	Meas.	Z_0 (Ohm)	Z (Ohm)	Z-Z_0 (Ohm)	Average	Error
-1.3	1	5592	6198	605	915	220
	2	5833	6878	1045		
	3	5932	7028	1096		

V vs RHE	Meas.	Z_0 (Ohm)	Z (Ohm)	Z-Z_0 (Ohm)	Average	Error
-1.4	1	5430	4202	-1228	-1254	253
	2	5097	3292	-1804		
	3	5547	4817	-730		

V vs RHE	Meas.	Z_0 (Ohm)	Z (Ohm)	Z-Z_0 (Ohm)	Average	Error
-1.5	1	5928	5697	-231	1323	1101
	2	5461	7629	2168		
	3	5559	7593	2034		

Table A.2. EIS data of electrochemical potassium intercalation extracted from the Nyquist plots. Z_0 stands for the resistance measured before the electrochemical intercalation, while Z stands for the resistance measured after the intercalation. The difference of Z_0 and Z gives an indication about the success of the intercalation, if the value of Z-Z_0 is positive, then the resistance of the electrode increased, if Z-Z_0 is negative, then the resistance of the electrode decreased.

Molecular Dynamics Simulations

Simulation details and parameters

All simulations were carried out in Large-scale Atomic/Molecular Massively Parallel Simulator (LAMMPS) simulation package [1]. First, to optimize the cross-interaction parameters between the solid (MoS_2) and the water, simulations of water droplets, containing different numbers of water molecules were simulated. Afterwards, based on the WCA calculations, the optimized cross-interaction parameters were implemented to the umbrella sampling simulations to study the intercalation of different ions.

The REBOMOS potential was used for the MoS_2, developed by Jiang et al. [2]. REBO potential is already widely used for hydrocarbon systems, as it can treat single, double or even triple bonds correctly. The REBO potential describes the many-body effects together with the chemical bonding by introducing a parametrized bond-order function to a pair potential. Thus, the different possible bonding states of the system can be described with the same parameters due to the bond-order function. Despite that the REBO potential does not include any quantum effects and electrons are not explicitly considered, it has proven to be qualitatively predictive and generally quantitatively precise. The REBOMOS potential expresses the potential energy of a many-body Mo-S system in the framework of the REBO potential. Its main feature is to describe the elastic and structural properties of MoS_2 correctly, which is primarily needed in our system.

The SPC/E water model was used for the description of interactions between the H and O atoms in the water molecules. The rigid structure of the water molecules was enforced via the SHAKE algorithm. Coulomb's law was used to model the electrostatic interactions, while the LJ potential was used to describe the attraction and the repulsion between the atoms:

$$\Phi(r_{ij}) = 4\epsilon_{oo}[(\frac{\sigma_{oo}}{r_{oo}})^{12} - \frac{\sigma_{oo}}{r_{oo}})^{6}] + \frac{1}{4\pi\epsilon_0}\sum_{i=1}^{3}\sum_{j=1}^{3}\frac{q_i q_j}{r_{ij}}, \tag{A.1}$$

where the first term of the equation describes the LJ potential applied for oxygen atoms ($\sigma_{OO} = 3.166$ Å, $\epsilon_{OO} = 0.00673$ eV) and due to the presence of charged atoms, the last term gives the Coulomb force between those. Atom i possesses the charge of q_i, while the distance between atoms i and j is used to describe non-Coulombic interactions between atoms with r_{ij} and ϵ_0 is the dielectric constant for vacuum.

The Lorentz-Berthelot mixing rule was applied to calculate the cross-interaction potentials:

$$\epsilon_{ij} = \sqrt{\epsilon_i \epsilon_{ij}} \qquad and \qquad \sigma_{ij} = \frac{1}{2}(\sigma_i + \sigma_j). \tag{A.2}$$

In the case of MoS_2-water interactions, the Mo-O and the S-O interactions are scaled by keeping ϵ_O fixed and changing ϵ_{Mo} and ϵ_S and then using

equation A.2 to calculate the cross-interaction parameters. The σ in equation A.2 is unchanged during the scaling and the cutoff distance is set at 12 Å.

For the simulations optimizing the Mo-O and S-O cross-interactions, an MoS_2 cluster made up of 4 sheets and consisting of 180 000 atoms was used with different water droplet sizes (2500, 5000, 10 000, 12 500 and 15 000 water molecules) in a simulation box of 480 × 275 × 185 Å. The water molecules were deposited in a sphere in the start of the simulation, then a canonical time integration simulation was performed with the time step of 1 fs for 2 ns with the application of a Nose-Hoover thermostat and periodic boundary conditions.

Once the optimized cross-interaction parameters were calculated, in the intercalation simulations a smaller box (193 × 94 × 44 Å) was used with an MoS_2 cluster of 10 800 atoms, 18 000 water molecules and 1 salt molecule (NaCl or KCl). For all the simulations, a 1 fs time step was used. The geometry was created using the software Packmol [3], at first, the system was compressed in an anisotropic NPT ensemble keeping the MoS_2 cluster rigid. Then, the system was deformed in order for the MoS_2 cluster to gain its hydrated form [4]. Afterwards, the intercalation of the respective alkali metal ion was performed using umbrella sampling (US) in an isothermal-isobaric time integration. An external electric field (E) was imposed on the system, which is described as $f_{ie} = q_i E$ and is applied on the atoms in accordance with their charges (q_i). Finally, the Gibbs free-energy profiles with the weighted histogram analysis method (WHAM) [5] were reconstructed. In all simulations, periodic boundary conditions were applied with a cutoff distance of 12 Å.

The LJ potential was also used for the salts in the system. For the KCl and the NaCl a transferable ion force field was used, which was developed by Loche and co-workers [6]. In table A.4 the new LJ parameters are collected, the belonging σ_{I-J} values are kept the same and are based on the Lorentz-Berthelot mixing rule.

Ion	σ_i (Å)	ϵ_i (eV)	q_i (e)
Na^+	2.31	0.0046639	+1
Cl^-	4.30	0.004353	-1
K^+	2.83	0.009327	+1
Cl^-	4.30	0.004353	-1

Table A.3. LJ potential parameters for KCl and NaCl [6, 7].

Cross-interaction	ϵ_i (eV)
S - S	0.020000
Mo - Mo	0.000586
Mo - S	0.003423
Mo - O	0.002473
S - O	0.014448

Table A.4. Scaled cross-interaction ϵ_{I-J} for MoS_2 and SPC/E water model.

Scaling solid-liquid interactions

In order to obtain results that describe the mechanisms in a physically correct manner, first the cross-interaction parameters of the different atoms (Mo, S, O and H) were optimized. This was done through simulating water droplets over a large MoS_2 sheet and measuring the water contact angle (WCA). Since the contact angle is dependent on the droplet radius due to the size-dependent influence of line tension, different droplet sizes from 2 500 to 15 000 water molecules were simulated. Afterwards, the WCA was determined by fitting a tangent line to the outer water shell to each of the droplets.

As the WCA changes with the size of the water droplet, there were 5 different droplet sizes (2500; 5000; 10 000; 12 500 and 15 000) selected to extrapolate to the macroscopic contact angle. Number density contours were calculated from the equilibrated droplets on the MoS_2 surface. An average droplet profile is given from these contour plots which allows to calculate the different WCAs belonging to different droplet sizes. The contour plots were obtained by dividing the volume of the simulation box into cubical bins (size of 1 bin was 0.1 Å). In Figure A.2 (a) and (b) number density contours are shown of droplets containing 15 000 water molecules using the original cross-interaction parameters. The shape of the contour plots already show the difference in the WCAs as a consequence of the cross-interaction parameters.

In Figure **A.2** (c and d), the outer lines of the contour plots are shown for different droplet sizes, using the original cross-interaction parameters (c) and using the scaled cross-interaction parameters (d). The difference between the WCAs due to the cross-interaction parameters for the different droplet sizes is visible. In the WCA fitting and calculation, as the thickness of the hydration layer is and should be subtracted from the data before fitting. Once these outer lines were subtracted from the contour plots and the hydration layers were excluded from the data, circular curve fit was performed (for fitting see Supplementary information and Figure S2). Afterwards, a tangent line was fitted at the end of each curve, where the slope of the tangent line gives the WCA.

In both profiles, a dense region can be observed around z = 24 Å with a thickness of 3 Å, which is the hydration layer. This hydration layer thickness

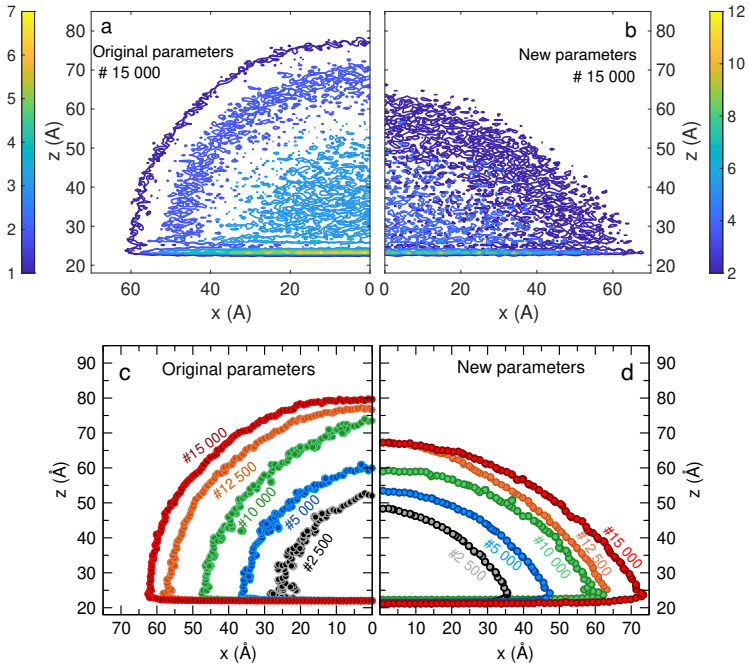

Figure A.2. (a) Number density contour plot of droplet containing 15 000 water molecules with the original cross-interaction parameters. (b) Number density contour plot of droplet containing 15 000 water molecules with the optimized cross-interaction parameters. (c) Outer lines of number density contour plots of droplets containing different number of water molecules with original cross-interaction parameters. (d) Outer lines of number density contour plots of droplets containing different number of water molecules with scaled cross-interaction parameters.

is called as the critical distance (z_c), the data below z_c has to be excluded from the curve fitting and the WCA calculation. The z_c has a crucial role in the WCA calculation, as this is the point where an extrapolation has to be drawn to the substrate and calculate the contact angle. Hence, the fitting of the functional form (polynomial, circular or elliptical) and the value of the z_c affect the WCA value heavily. In Figure A.3 the difference between the fitted curves (polynomial and circular) and the drawn tangent lines is shown. The two tangent lines give significantly different WCAs with a difference of 13.12°, as a result of two curve fits. These kinds of differences have been reported in the literature previously [8].

Using the given LJ parameters of the REBOMOS potential together with the SPC/E the MoS_2 surface shows to be more hydrophobic than in experimen-

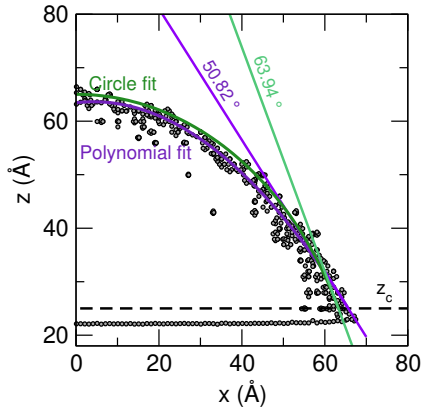

Figure A.3. Difference between polynomial and circular fit of the water droplet on the MoS_2 surface. Dashed line shows the critical distance calculated from the number density contours.

tal results [9]. Hence, we scaled parameters ϵ_{Mo} and ϵ_S until the observed water contact angle (WCA) agrees with the experimental value. The experimental water contact angle is measured in the interval between 65 ° and 75 ° for MoS_2 [10–13], However, it is important to mention that the WCA on a freshly exfoliated MoS_2 sheet was found to be 69.0 ° ± 3.8 ° by Kozbial et al. [11]. The scaling parameter β was used to obtain the new cross-interaction parameters: $\epsilon_X^{new} = \beta\epsilon_X^{old}$.

These microscopic WCAs were plotted as a function of 1/r, where r is the radius of the water droplet, and hence, the macroscopic contact angle was determined by a linear extrapolation where 1/r→0 [11]. A detailed description of the WCA optimization is shown in the Supplementary Information. Figure A.4 (c) shows the difference between the WCAs using the original cross-interaction parameters and the optimized parameters, where the macroscopic WCA was decreased 20°, achieving a good agreement with the experimentally measured 69° WCA.

A

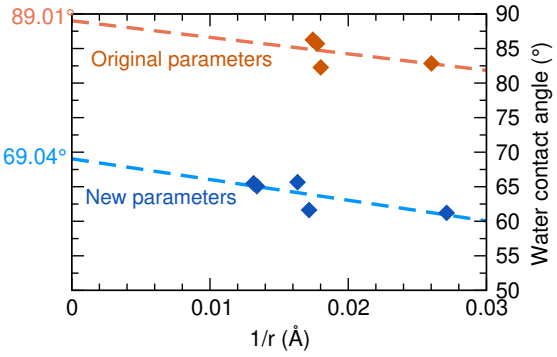

Figure A.4. Difference in macroscopic WCA with original cross-interaction parameters and optimized cross-interaction parameters.

Intercalation simulations with Umbrella Sampling

For the intercalation of alkali metal ions into the MoS_2 cluster, umbrella sampling was used. This technique is among the most frequently utilized methods for surpassing free energy barriers in the calculation of free energy [14]. In umbrella sampling a series of independent windows are used and the conformational transition is studied based on a selected collective variable. In each window, there is a simple harmonic potential applied on the reaction coordinate and time integration is performed at the same time. Once the simulations are completed, the weighted histogram analysis method (WHAM) is used to create the combined statistics based on the independent windows. The reconstructed energy profiles show the energy barrier of the system.

For the sampling itself, there is a spring force applied on the alkali metal ion:

$$\mathbf{F_{spring}} = -k\mathbf{x}, \tag{A.3}$$

where k is the spring constant, $\mathbf{x}$ is the x,y,z point to which the spring is tethered. In figure A.6, the effect of the strength of the spring constant is shown. The free energy profiles show the same tendency for the different spring constants for both with and without an external electric field. However, it can be observed that with a looser spring constant, the energy barrier is higher for the intercalation and it decreases as the strength of the spring constant increases. When the probability density is calculated during the WHAM reconstruction, however, the probability for the ion intercalation is the same for all cases. Thus, to minimize the constraint on the spring, the k=1 eV was chosen for the rest of the umbrella sampling simulations.

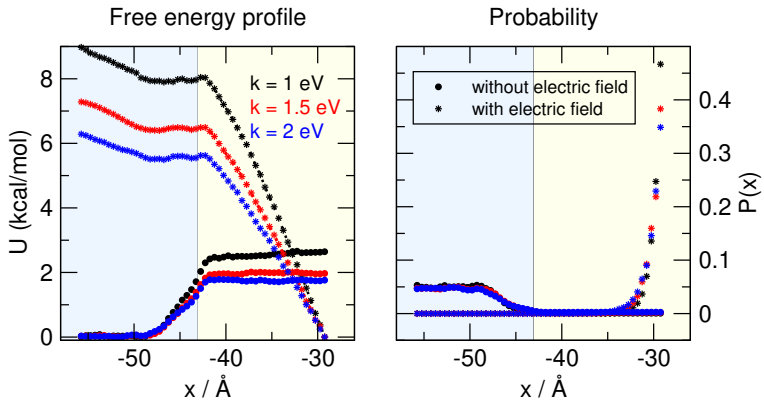

Figure A.5. Free energy profiles and belonging probability densities with different spring constants (k=1;1.5;2 eV) without and with external electric field (E=0.04 V/Å) for K^+ ion intercalation in 2L geometry.

A

Different hydration levels of MoS_2

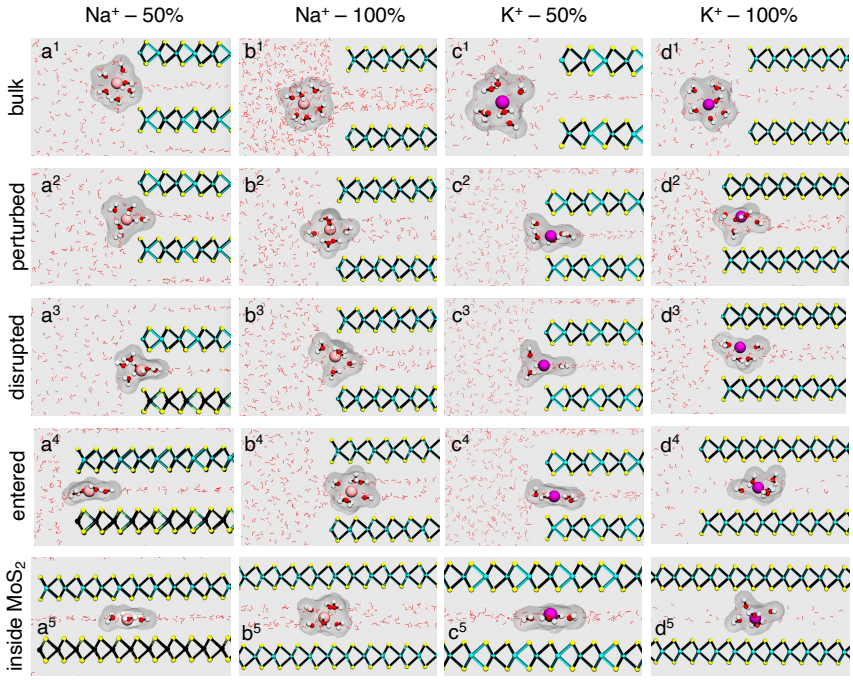

Figure A.6. (a-d) Screenshots of MD simulations at different times based on the location of the hydrated ions (molybdenum atoms are represented with blue color, sulfur atoms are represented with yellow color, sodium ions are represented with pink color, potassium ions are represented with purple color).

Characterization
MoS_2 nanopowder

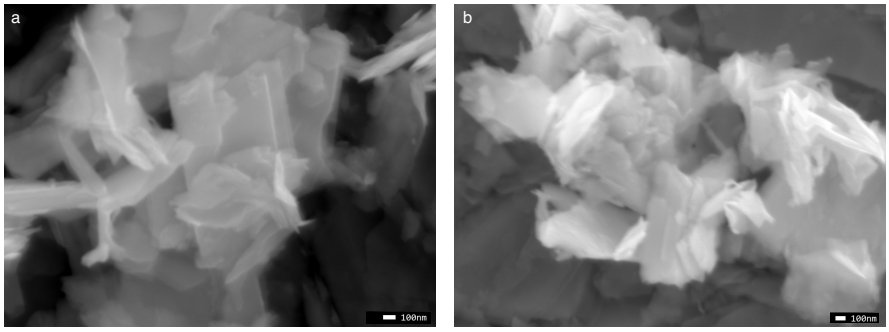

Figure A.7. SEM images taken of the MoS_2 nanopowder (Sigma-Aldrich).

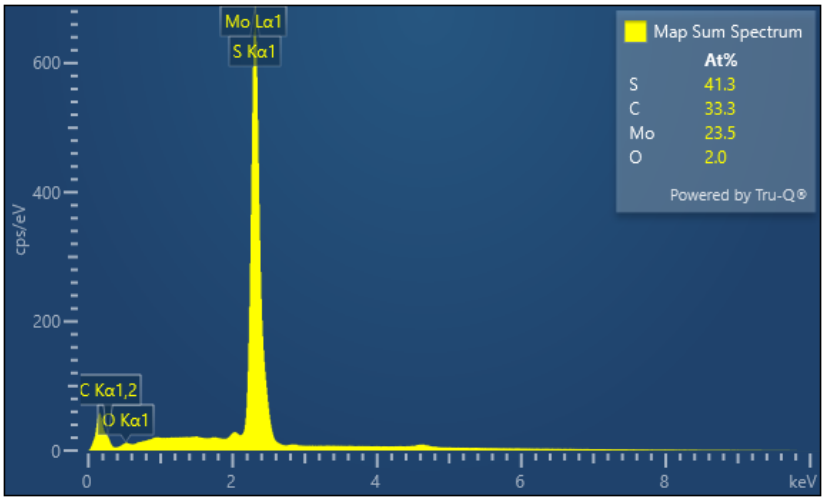

Figure A.8. EDS point analysis taken of the MoS_2 nanopowder (Sigma-Aldrich).

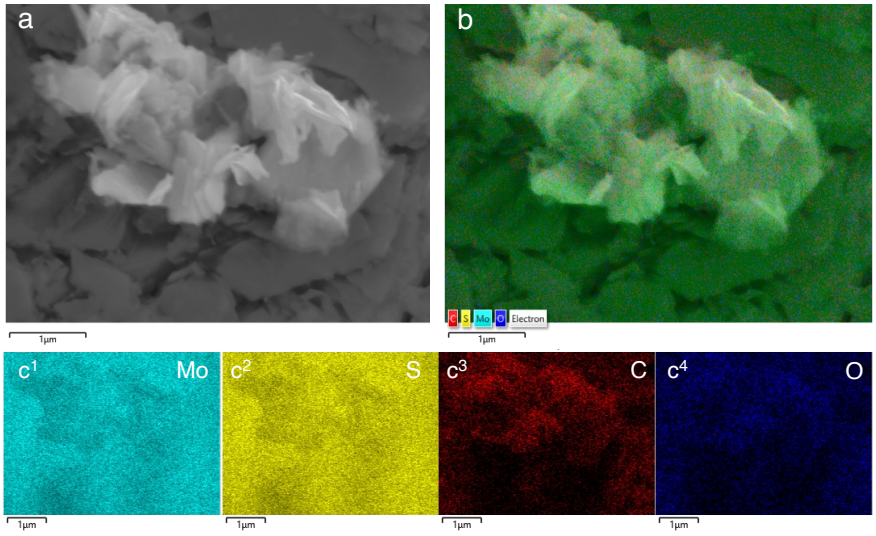

Figure A.9. EDS mapping taken of the MoS_2 nanopowder (Sigma-Aldrich).

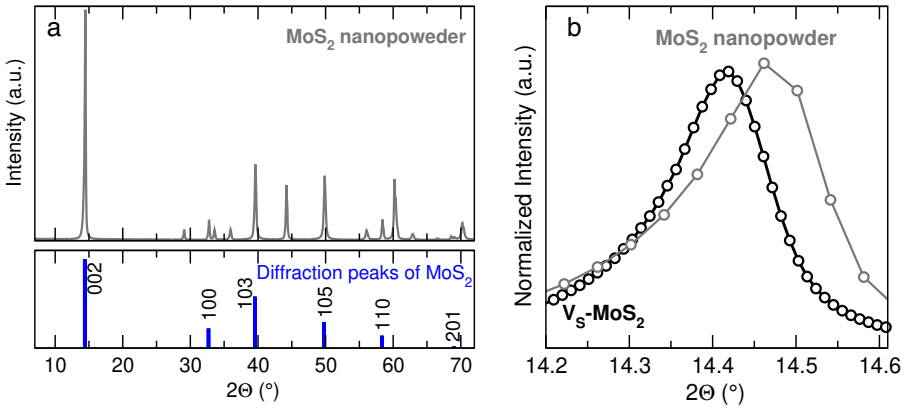

Figure A.10. XRD spectrum taken of the MoS_2 nanopowder (Sigma-Aldrich).

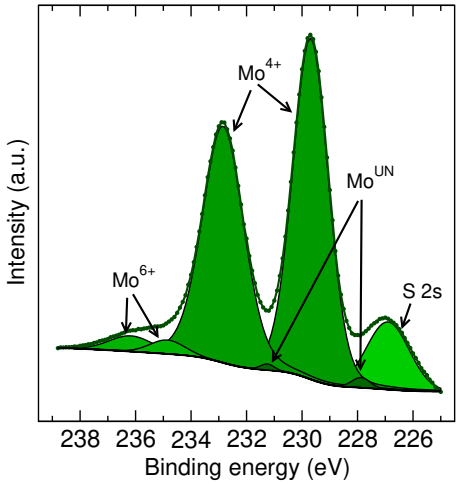

Figure A.11. Fitted Mo 3d5 spectrum of the MoS_2 nanopowder (Sigma-Aldrich). The areas of the undercoordenated Mo sites (0.65 % and 0.29 %) are lower than the ones detected for the electrode, which also supports the argument that some of the sulfur vacancies are induced during the electrode preparation.

	S 2s	$\mathbf{Mo^{UN}_{5/2}}$	$\mathbf{Mo^{4+}_{5/2}}$	$\mathbf{Mo^{UN}_{3/2}}$	$\mathbf{Mo^{4+}_{3/2}}$	$\mathbf{Mo^{6+}_{5/2}}$	$\mathbf{Mo^{6+}_{3/2}}$
Position (eV)	226.87	227.84	229.65	231.21	232.81	234.82	236.13
Area (%)	10.25	0.65	46.24	0.29	38.27	1.7	2.41

Table A.5. Positions and calculated peak areas of the Mo 3d5 spectra fitting by the MultiPak software for the MoS_2 nanopowder.

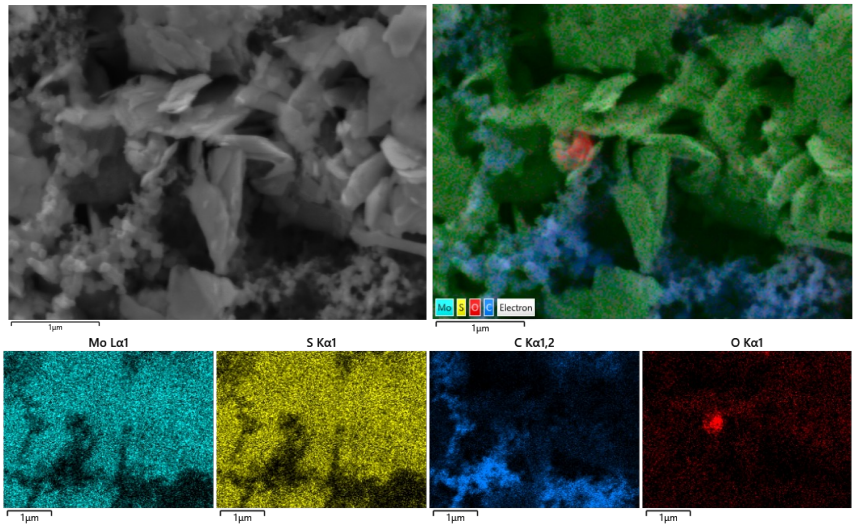

Figure A.12. EDS images of the V_S-MoS_2 electrodes. The EDS maps confirm that the V_S-MoS_2 and the carbon balck is well-dispersed and the V_S-MoS_2 is covering the majority of the electrode surface.

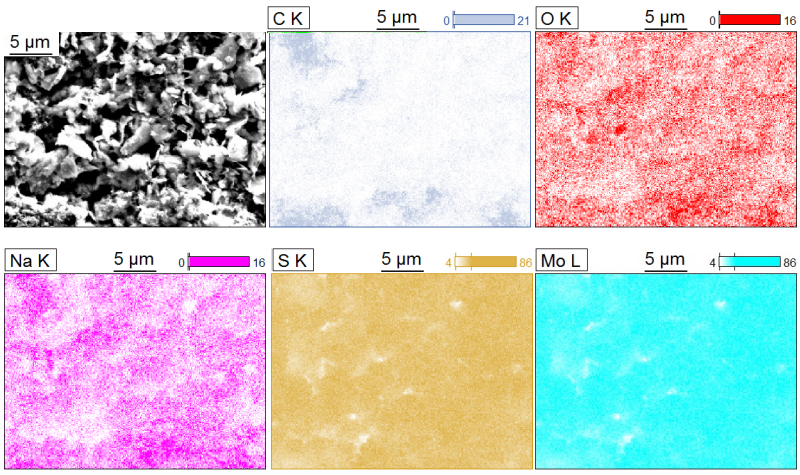

Figure A.13. EDS images of the sodium-intercalated V_S-MoS_2 electrodes.

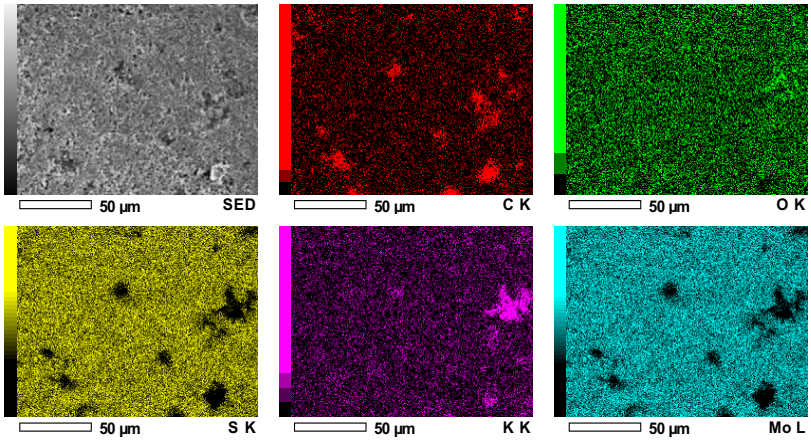

Figure A.14. EDS images of the potassium-intercalated V_S-MoS_2 electrodes.

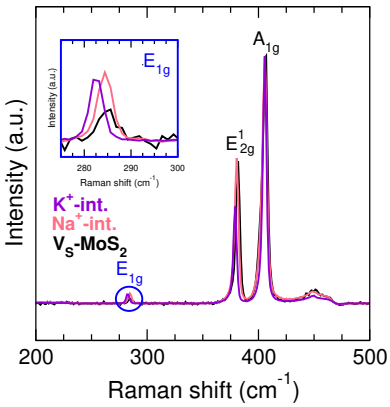

Figure A.15. Full Raman spectra of the V_S-MoS_2, Na^+-intercalated V_S-MoS_2 and K^+-intercalated V_S-MoS_2.

X-ray Photoelectron Spectroscopy

Electron dopant density calculation

The effective density of states for electrons is calculated as

$$N_C = 2 \times \left[\frac{2\pi m_n k_B T}{\hbar^2} \right]^{3/2}, \tag{A.4}$$

where T is temperature, k_B is the Boltzmann constant, $\hbar$ is Planck's constant and m_n is the effective mass for electrons. Assuming that m_n is $0.45m_0$ [15, 16] for bulk MoS_2, where m_0 is the free mass of electrons. From N_C, the electron doping concentration (N_D) was calculated using E_C-E_F obtained from the XPS spectra:

$$N_D = N_C exp\left(\frac{E_F - E_C}{k_B T} \right), \tag{A.5}$$

with the assumption of degenerate doping and using the Boltzmann approximation. This translates into different electron dopant densities and shows that the K^+-intercalated V_S-MoS_2 has a tenfold higher electron doping concentration than the non-intercalated V_S-MoS_2. This also corresponds well with the downshifts and the presence of excess electrons in the Mo 3d5 spectra shown in figure 3.5 (c).

		S 2s	$Mo^{UN}_{5/2}$	$Mo^{4+}_{5/2}$	$Mo^{UN}_{3/2}$	$Mo^{4+}_{3/2}$	$Mo^{6+}_{5/2}$	$Mo^{6+}_{3/2}$
V_S-MoS_S	Position (eV)	226.26	227.21	229.16	230.73	232.29	234.55	235.70
	Area (%)	10.29	1.60	43.28	0.86	38.16	3.37	2.43
Na-int. V_S-MoS_S	Position (eV)	225.77	226.92	228.63	230.26	231.78	233.31	235.35
	Area (%)	11.86	2.47	43.81	1.91	32.50	4.25	3.21
K-int. V_S-MoS_S	Position (eV)	225.57	226.70	228.51	229.91	231.69	234.02	235.18
	Area (%)	10.28	3.19	42.56	1.37	37.29	2.78	2.53

Table A.6. Positions and calculated peak areas of the Mo 3d5 spectra fittings by the MultiPak software.

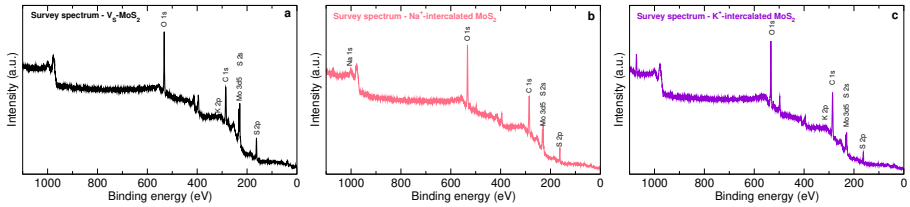

Figure A.16. XPS survey spectra of non-intercalated **(a)**, Na^+-intercalated **(b)** and K^+-intercalated **(c)** MoS_2 electrodes.

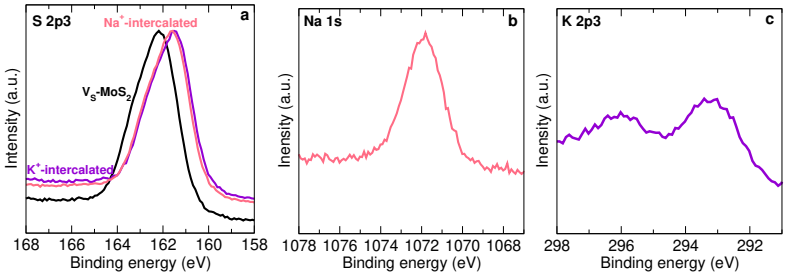

Figure A.17. **(a)** S 2p3 XPS spectra of the non-intercalated, Na^+-intercalated and K^+-intercalated MoS_2, **(b)** Na 1s spectrum of the Na^+-intercalated MoS_2 and **(c)** K 2p3 spectrum of the K^+-intercalated MoS_2.

B

Appendix to Chapter 4

Experimental methods

Electrode preparation: The as-purchased MoS_2 nanopowder underwent a series of steps to fabricate the electrodes. MoS_2 nanopowder (99% trace metal basis, Sigma Aldrich) was combined with Carbon Black (CB, Fisher Scientific) and poly(vinyl alcohol) (PVA) in a weight ratio of 90:5:5, respectively. The measured components were transferred to a 5 cm^3 vial, followed by the addition of 2 mL of deionized (DI) water. The resulting suspension was sonicated in a water bath for 10 minutes to ensure uniform dispersion. Glassy carbon substrates (1.5 × 1.5 cm, Sigma Aldrich) were pre-treated by cleaning with DI water, sonicating in isopropyl alcohol for 5 minutes, and drying with compressed air. Subsequently, 25 μL of the sonicated ink was drop-cast onto each glassy carbon substrate. The coated samples were allowed to dry in ambient air. To complete electrode preparation, a copper tape was attached to the substrate as an electrical connector, and the electrode (together with the copper tape) was partially (fully) masked with tape to expose only a circular area with a 10 mm diameter.

The **linear sweep voltammetry** measurements were conducted using a Bio-Logic VMP-3e Multichannel Potentiostat controlled by the EC-Lab software. The electrode was positioned in the cathode compartment alongside micro Ag/AgCl reference electrode (Mengel Engineering) , while a Pt mesh electrode was placed in the anode compartment. All electrodes were then connected to the potentiostat, and the entire system was enclosed within a Faraday cage.

The **Raman** spectrum were acquired using a WiTec Alpha300R Raman Imaging microscope equipped with a 532 nm laser at 1 mW power to minimize sample damage. The integration time was set to 5 seconds with 10 accumulations, and a 63X/0.9 water-dipping objective was utilized. To achieve high spectral resolution, a 1800 g/mm grating was employed, ensuring a resolution better than 1 cm^{-1}.

Scanning Electron Microscopy was conducted using a JEOL IT800SHL system equipped with a field emission gun, operated at 10.00 kV with a beam current of 42.20 nA.

X-ray photoelectron spectroscopy was performed using a Physical Electronics (PHI) 5400 instrument (Eden Prairie, USA). The XPS spectra were acquired utilizing non-
monochromatic Al Kα radiation, generated by an X-ray source with an Al anode operating at 200 W and 13.5 kV. The primary photoelectron lines of each element were recorded with a step size of 0.1 eV and a dwell time of 1.25 s, using a spherical capacitor analyzer set to a pass energy of 71.55 eV. For data analysis and processing, the MultiPak software was employed. The acquired peaks were normalized and fitted, with the iterated-Shirley background applied for peak fitting.

The **product analysis** was carried out in a two-compartment three-electrode electrochemical H-cell (Pine Research) connected to a BioLogic SP-50e Potentiostat. The anode compartment contained a Pt wire, while the cathode

compartment contained the working electrode, the reference electrode (micro Ag/AgCl reference electrode (Mengel Engineering)) and a glass tube for bubbling CO_2 continuously into the electrolyte. The working electrode consisted of MoS_2 deposited on 15 mm x 15 mm glassy carbon substrate covered with tape to establish an exposed area of 10 mm diameter and connected to the potentiostat with copper tape. Both compartments of the cell were contained the electrolyte consisting of 70 vol% water and 30 vol% [EMIM][BF_4] (Iolitec). Prior to each measurement, the electrolyte was purged with CO_2 for 1 hour at the rate of 10 mL/min, afterwards, a constant potential was applied for 1 hour on the cell. During the measurement (see Figure B.4), the bubbling of the CO_2 continued at a constant rate of 10 mL/hour in order to provide feedstock for the CO_2 reduction reaction. Throughout the measurement, gas samples were taken from the cathode compartment with a 10 mL Hamilton gas-tight sample lock syringe in 10-minute intervals and were injected into the GC (CompactGC 4.0, Interscience). The GC contained three detectors: two thermal conductivity detectors (TCD) with Carboxen101 columns and one flame ionization detector (FID). The carrier gas for the first TCD is Helium (He) gas (Linde, 99.999%), hence oxygen, nitrogen, carbon-monoxide and carbon-dioxide are detectable in the channel, while for the second channel the carrier gas is Argon (Ar) (Linde 99.999%), hence hydrogen is detectable on this channel; with the FID detector the different hydrocarbon products are detectable. The GC was baked out and calibrated for hydrogen, methane, ethane, propane, butane, pentane, pentene, hexane, hexene and heptene gases using calibration bottles supplied by Linde.

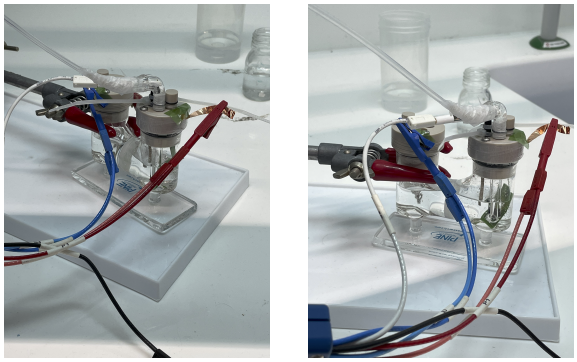

Figure B.1. Photographs taken during an experiment of the two-compartment cell connected to the potentiostaat.

For the FE calculations, the areas under the chromatograms could be extracted from the software Chromeleon and based on the calibration curves of the GC, these areas were converted to ppm values for each detected gas. Afterwards, the FEs of the different products were calculated based on

the mole fractions of the products, following the calculation method used by Asadi et al. [17–19]. The following equation was used for FE calculation:

$$FE = \frac{moles_{product} \times nF}{I \times t} \times 100, \tag{B.1}$$

where n is the number of electrons required for the reaction (depending on the product n differs), F is the Faraday number, I is the current measured by the potentiostat, t is the duration of the chronoamperometry measurement.

Surface characterization

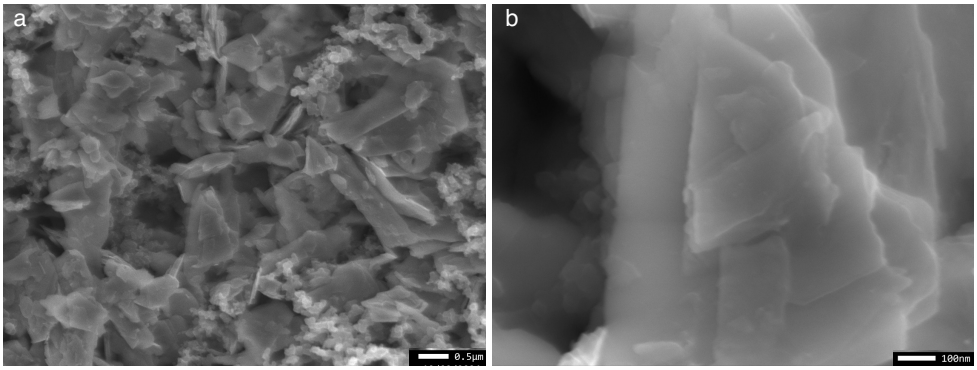

Figure B.2. SEM images taken of the unexposed electrode at different magnifications. Image **(a)** present the surface of the electrode, that the MoS_2 nanoflakes and the carbon black are well-dispersed after the deposition. **(b)** The surface is mainly covered with the MoS_2 nanoflakes, in which the particles have a wide range of sizes and both the edges of the particles.

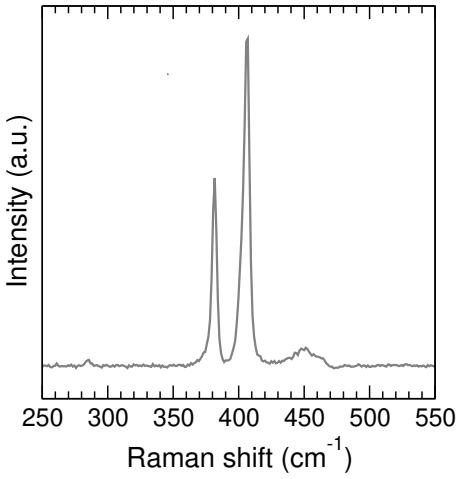

Figure B.3. Full Raman spectrum.

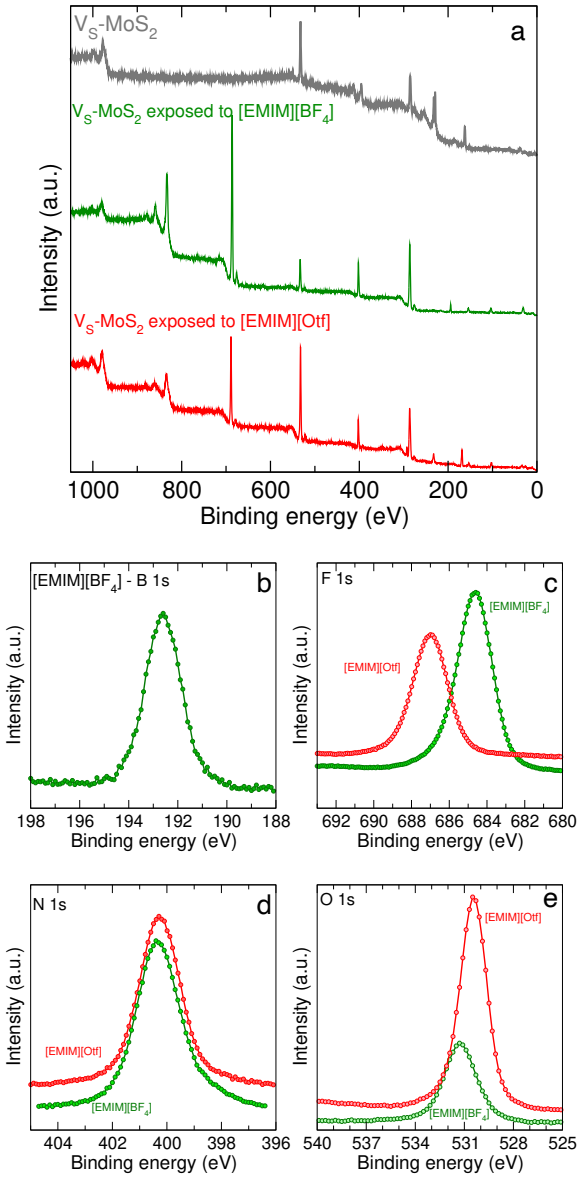

Figure B.4. **(a)** XPS surveys of V_S-MoS_2, V_S-MoS_2 electrode exposed to [EMIM][BF_4], V_S-MoS_2 electrode exposed to [EMIM][Otf], **(b)** B 1s spectrum of V_S-MoS_2 electrode exposed to [EMIM][BF_4], **(c)** F 1s spectrum of the V_S-MoS_2 electrode exposed to each IL, **(d)** N 1s spectrum of the V_S-MoS_2 electrode exposed to each IL, **(e)** O 1s spectrum of the V_S-MoS_2 electrode exposed to each IL.

C

Appendix to Chapter 5

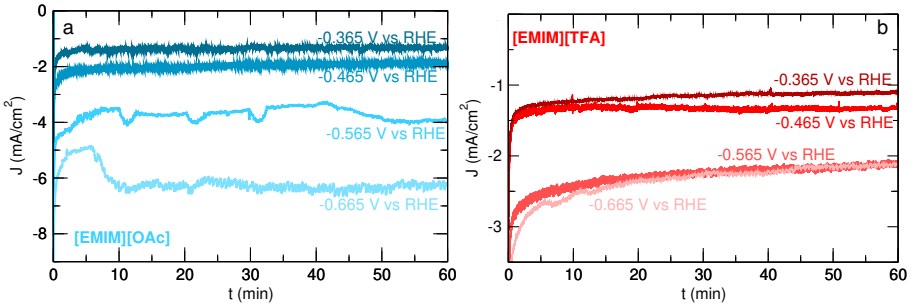

Figure C.1. Chronoamperometry curves for [EMIM][OAc] **(a)** and [EMIM][TFA] **(b)** showing the stability of the electrode through the product analysis. In the case of the [EMIM][OAc], small wells can be seen at the voltage of -0.565 V vs RHE which is due to the disturbance of the system for the gas sample extraction.

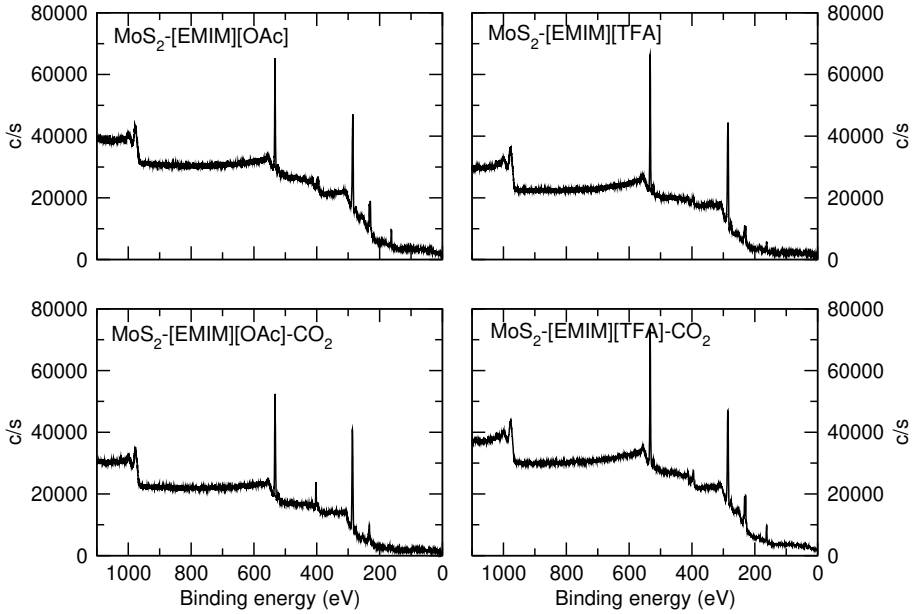

Figure C.2. Survey spectra of the electrodes based on the ionic liquid environments they were subjected to.

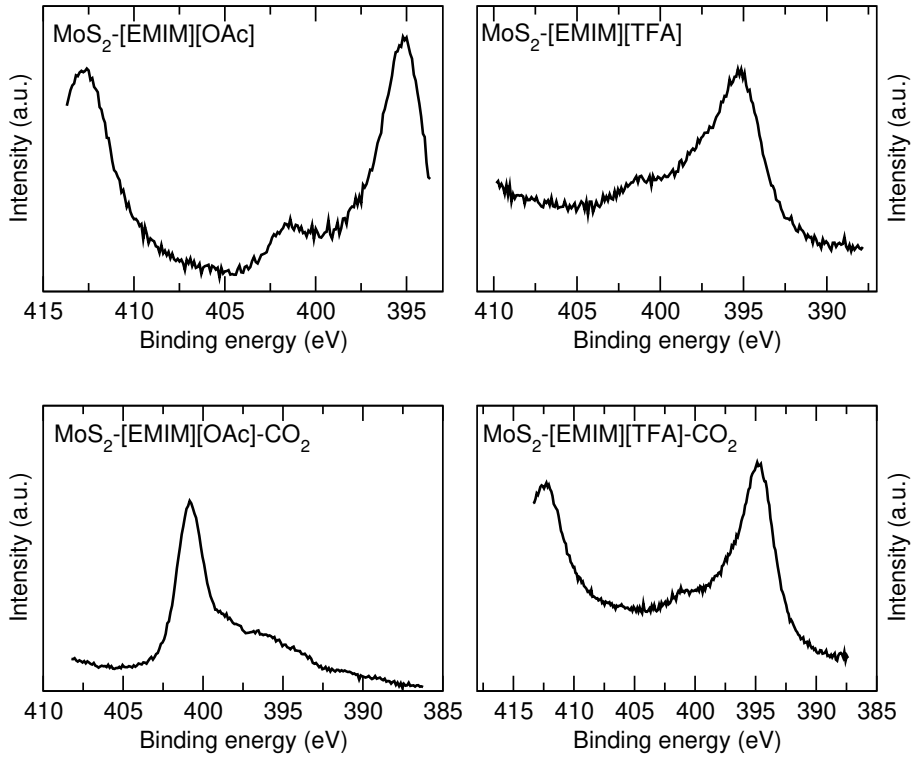

Figure C.3. N 1s spectra of the electrodes based on the ionic liquid environments they were subjected to.

Config. ID	Description	Total energy (eV)	Adsorption Energy (eV)	Average O-Mo Distance (Å)	Electron Transfer (e)	Sel.
[OAc]-1	Acetate above vacancy, imidazolium ring tilted	-818.7850784	-3.5691012	2.12	0.72	X
[OAc]-2	Imidazolium ring parallel to surface	-818.1731793	-2.9572021	2.45*	0.54	
[OAc]-3	Imidazolium ring perpendicular to surface	-817.950234	-2.7342568	2.58*	0.48	
[OAc]-4	Ion pair with anion away from vacancy	-817.429238	-2.2132608	3.12*	0.32	
[OAc]-5	Ion pair with cation near vacancy	-817.110902	-1.8949248	3.47*	0.25	

Table C.1. [EMIM][OAc] configurations on MoS_2 defect sites (System -660.880255, [EMIM][OAc] -154.3357215).

Config. ID	Description	Total energy (eV)	Adsorption Energy (eV)	Average O-Mo Distance (Å)	Electron Transfer (e)	Sel.
[TFA]-1	Trifluoroacetate above vacancy, planar imidazolium	-820.3629555	-3.8490346	2.31	0.38	X
[TFA]-2	Imidazolium ring parallel to surface	-819.7616348	-3.24771388	2.58	0.31	
[TFA]-3	Imidazolium ring perpendicular to surface	-819.4599062	-2.94598531	2.72	0.27	
[TFA]-4	Ion pair with anion away from vacancy	-818.9157833	-2.40186244	3.24	0.22	
[TFA]-5	Ion pair with cation near vacancy	-818.6345238	-2.12060294	3.52	0.18	

Table C.2. [EMIM][OAc] configurations on MoS_2 defect sites (System -660.8802557, [EMIM][TFA] -155.6336652).

C

Config. ID	Description	Total energy (eV)	Adsorption Energy (eV)	O-C-O Angle (°)	C-O Bond Lenght (Å)	Electron Transfer (e)	Sel.
CO_2-MoS_2-1	CO_2 directly above S vacancy	-684.6943715	-0.37488875	177.2	1.17	0.11	X
CO_2-MoS_2-2	CO_2 parallel to surface, away from vacancy	-684.4970528	-0.17757003	179.5	1.16	0.04	
CO_2-MoS_2-3	CO_2 perpendicular to surface	-684.5408257	-0.22134292	179.1	1.16	0.05	
CO_2-MoS_2-4	CO_2 at Mo-Mo bridge site	-684.5713953	-0.25191252	178.8	1.16	0.07	
CO_2-MoS_2-5	CO_2 at intact S site	-684.4741892	-0.15470642	179.7	1.16	0.03	

Table C.3. CO_2 adsorption on defective MoS_2 (System -660.8802557, CO_2 -23.43922708).

Config. ID	Description	Total energy (eV)	Adsorption Energy (eV)	O-C-O Angle (°)	C-O Bond Length (Å)	Electron Transfer (e)	Sel.
CO2-[OAc]-1	Chemical coordination with acetate	-730.8233543	-1.4206264	133.2	1.24	0.61	X
CO2-[OAc]-2	CO_2 near imidazolium ring	-729.7543702	-0.3516423	178.5	1.17	0.08	
CO2-[OAc]-3	CO_2 near MoS_2 vacancy, away from IL	-729.7001602	-0.2974323	179.1	1.16	0.1	
CO2-[OAc]-4	CO_2 between cation and anion	-729.8480388	-0.4453109	175.2	1.18	0.12	
CO2-[OAc]-5	CO_2 above imidazolium, perpendicular	-729.621803	-0.2190751	179.5	1.16	0.06	

Table C.4. CO_2 adsorption on [EMIM][OAc]-defective MoS_2 system (System -554.2051534, CO_2+[EMIM][OAc] -175.1975745).

Config. ID	Description	Total energy (eV)	Adsorption Energy (eV)	O-C-O Angle (°)	C-O Bond Length (Å)	Electron Transfer (e)	Sel.
CO2-[TFA]-1	Chemical coordination with acetate	-731.1917944	-0.58031963	178.3	1.17	0.14	X
CO2-[TFA]-2	CO_2 near imidazolium ring	-730.9219608	-0.31048602	179.2	1.16	0.05	
CO2-[TFA]-3	CO_2 near MoS_2 vacancy, away from IL	-730.9458782	-0.33440336	179	1.16	0.09	
CO2-[TFA]-4	CO_2 between cation and anion	-731.0492051	-0.4377303	178.8	1.16	0.11	
CO2-[TFA]-5	CO_2 above imidazolium, perpendicular	-730.8618293	-0.25035454	179.6	1.16	0.04	

Table C.5. CO_2 adsorption on [EMIM][TFA]-defective MoS_2 system (System -554.2051534, CO_2+[EMIM][TFA] -176.4063214).

Acknowledgements

First, I would like to thank my supervisors, Dr. Remco Hartkamp and Dr. Peyman Taheri, and my promotor, Prof. Dr. Arjan Mol, for their guidance and support throughout the research presented in this thesis. Remco, I especially want to thank you for all the time you dedicated to helping me develop and troubleshoot simulations, and for making time for meetings whenever I needed them. I am truly grateful for the encouragement and effort you invested in me over the years. Poulumi and Nabil, thank you for your collaboration and support with the DFT work. I would also like to thank Hans Brouwer for help with the XPS measurements, Ruud Hendrix for assistance with XRD, and Kees Kwakernaak for SEM imaging. Agnieszka Kooijman, you are without a doubt the best technician ever. Always kind and endlessly capable, there is nothing in the lab that could ever challenge you. Thank you for being there for us, especially in the middle of experiments that didn't work or failed repeatedly. Your support and kind words made all the difference. Yashan, you inspired a large part of this thesis, I will always be grateful for your guidance, support, and cheerful presence during the early months of this PhD. To my CTE group members, Ziyu, Keer, Reina, Ursa, Khatereh, Arash, Ehsan, Yaiza, Yeli and Gaojie, thank you for your help and companionship throughout this journey. Neslihan, thank you for supporting me at the end of this thesis by allowing me to lecture the amazing course, Transport Phenomena. It was an invaluable experience.

Dear Prasad and Prasaanth, you are the true heroes of this thesis! Prasad, your energy, practical knowledge, and perseverance, whether installing the GC or tackling the challenges of the ALD, have been a gift to the lab. Your support during the CO_2 reduction experiments, the endless gas injections, and our conversations during measurements made those days some of the most memorable. Prasaanth, I cannot thank you enough for your guidance over the past two years. Your involvement gave new meaning to my research, and your enthusiasm rekindled my own. Your optimism is a shining example to everyone. I wish you the very best in achieving your goals and dreams, as you have helped me achieve mine.

On a more personal note, I want to thank the two people who set me on this path: Móni and Dezső. You were my first supervisors and introduced me to the love of science. You taught me how to conduct research, craft beautiful figures, and present my work. You gave me the courage and momentum that carried me forward, and for that, I am forever grateful.

Though not the most social person, one thing I will truly miss is lunchtime at MSE. Whether the topic was space debris, food, death, or top three whatevers, these conversations lightened my heart and mind. And yes, the cake schedule helped too! Konstantina, Gesa, Jasper, Can, Luis, Philipp, Fabian, Julia, Jithin, Matthias, Mohamed, Arjun, Camila, and Alice, thank you for making those lunchtimes so memorable. Jhon, your kind jokes and positivity always lifted the mood. Daniel, your *veeery* funny jokes made even rainy days brighter. Joep, your endless dad jokes and unwavering optimism were lifesavers during gloomy Dutch weeks. Gautham, your kindness and excitement (especially about shoes and cooking!) were always a joy. José, thank you for your enthusiasm that often lifted my spirits. Tim, your calm presence and wise advice were invaluable. Through Soroush, I met more wonderful people. Hossein, Shima, Paniz, Gijs, Nima, Delaram, Kaveh, Sara, Mahdi, Yasaman, Ahmad, Parvin, Amir, Reihaneh, Sana and Hesam, I'm so happy to have you in my life. To my dear friends outside the Netherlands, Peti, Isabel, Hanna, and Alex, thank you for your unwavering support during these years.

Marco and Vitória, who would have thought we'd become such good friends! All the BBQs, parties, and trips have brought you both very close to my heart. Marco, I greatly value your stoic stability and sense of humor at any circumstance, most of all, when we have to separate Soroush and Vitória from fighting. Vitória, your generous heart and warm presence have brightened many moments. I hope our friendship continues forever for many years even if you are on the other side of the world right now!

My darling Elsa, I'm so happy we met during the final two years of my PhD! With you, I found a friend to share passions with, be it jewelry hunting at antique markets or binge-watching *Bridgerton and Emily in Paris*. Thank you for all the cozy tea-fueled gossip sessions and for simply being there.

In these years I also became a part of another family, the Aghaeians. I was welcomed with such love that I will always be grateful for! Shahla, Davood, Saeid, Setareh, Sara and Parsa I am deeply grateful for your warmth, generosity, and open hearts. Thank you for making me feel at home, for your kindness, your support, and for always treating me as one of your own.

Szeretném megköszönni a családomnak is, hogy velem tartottak ezen az úton. Gabi, Zoli†, Julcsi és Zsuzsika, Peti, Orsi és Petike, köszönök nektek minden bátorítást, amit ezen az úton kaptam tőletek! Nagyon hálás vagyok nagyszüleimnek, hogy töretlenül támogatnak a céljaim megvalósításában. Mama, Papa, Manyika és Papi, köszönök mindent, amit értem tettetek! Édesanyám és Édesapám, nagyon sok áldozatot hoztatok azért, hogy segítsetek az utamon, mégis mindig a legszélesebb mosollyal vártok, amikor hívlak titeket vagy hazamegyek látogatóba. Nem lennék az, aki ma vagyok a ti út- és példamutatásotok nélkül. Nem tudok mást mondani, minthogy köszönöm

szépen és nagyon szeretlek Titeket! Édes húgom, már csak a tudat, hogy itt vagy tőlem egy karnyújtásnyira boldoggá tesz! Zita, a pozitivitásod es a humorod mindig bearanyozza a napjaimat, nem tudom, hogy mihez kezdenek nélküled! Te mindig ott vagy nekem és a legkisebb kérdésbe teljes erőbedobással veted bele magadat, hogy segíts. Egyszerűen imádlak, úgy, ahogy vagy!

Last but not least, I want to thank You, my Love. Soroush, you were there for me in these last few years for better or worse, you encouraged me, you listened calmly to all my hopeless frustrations and you celebrated all my small achievements with the greatest of joy. I couldn't wish for a better, kinder, smarter or funnier boyfriend/fiancé/partner/husband in life than You! You fill my heart with hope and joy every morning and evening. The best thing that happened to me in this PhD is that I met you and the best decision I made was to ask you to take me to IKEA. The only thing I could wish now for us is to have many more trips there (and wherever) and enjoy life together to the fullest. I love you!

Eszter

Zoetermeer, July 2025

Curriculum Vitæ

Eszter Mádai was born in Miskolc, Hungary in 1995. She received her BSc in Chemical Engineering from the University of Pannonia, Hungary in 2018. Afterwards, she was accepted to the AMIS (Advanced Materials for Innovation and Sustainability) International Double Degree master program labelled by the European Institute of Innovation and Technology (EIT). Within the master program between 2019 and 2020, she completed her MSc in Materials Science at the Technical University of Darmstadt, Germany and her MSc in Chemistry at the University of Liège, Belgium. From late 2020, she worked towards her PhD in the field of materials science at Delft University of Technology.

List of Publications

Related to this thesis:

3. **E. Mádai**, N. Khossosi, P. Dey, P. Gonugunta, P. R. Anusuyadevi, A. Mol, P. Taheri, and R. Hartkamp. "Effect of imidazolium-based acetates as co-catalysts on the product selectivity of the electrochemical CO_2 reduction reaction with MoS_2". In: *in preparation* (2025)

2. **E. Mádai**, P. R. Anusuyadevi, R. Hartkamp, P. Gonogunta, A. Mol, and P. Taheri. "Production of Higher Hydrocarbons via Electrochemical CO_2 Reduction on Sulfur-Vacant Molybdenum Disulfide Catalyst". In: *under review at the Journal of Applied Catalysis O: Open* (2025)

1. E. Mádai, P. R. Anusuyadevi, P. Gonugunta, A. M. Armaki, A. Mol, P. Taheri, and R. Hartkamp. "Effects of alkali metal intercalation on structural and electronic properties of molybdenum disulfide". In: *Applied Surface Science* (2025), p. 164284

Other articles and book chapter published during the PhD:

5. R. N. Shaw, S. Pranavi, **E. Mádai**, J. P. K. D, L. Nafisa, H. F. Irshad, H. J. Gazi, P. Gonugunta, P. Taheri, R. Hendrixx, K. Kwakernaak, T. Hughes, A. Mol, and P. R. Anusuyadevi. "Floating Photocatalytic Coconut Fibres Coated with Graphitic Carbon Nitride (g-C_3N_4) For Wastewater Refinement". In: *in preparation* (2025)

4. R. S. Babu, E. Madai, D. S. Nair, P. Gonugunta, S. M. Armaki, R. Hendrikx, T. Panneerselvam, R. Murugan, V. R. K. Kumar, P. Taheri, *et al.* "Effect of synthesis conditions on morphology, surface chemistry and electrochemical performance of nickel ferrite nanoparticles for lithium-ion battery applications". In: *Journal of Materials Science: Materials in Electronics* 36.14 (2025), p. 865

3. B. I. Eijkel, K. Modaresifar, **E. Mádai**, M. Ganjian, P. Taheri, I. Apachitei, and L. E. Fratila-Apachitei. "High-aspect ratio titanium nanopillars modulate macrophage responses". In: *Biomaterials Advances* (2025), p. 214321

2. P. R. Anusuyadevi, S. Pranavi, R. N. R. Shaw, **E. Mádai**, D. J. P. Kumar, P. Gonugunta, P. Taheri, and A. Mol. "An Overview of Emerging 2D Nanomaterials: General Synthesis Methods and Properties". In: *Next-generation 2D Nanomaterials for Sustainable Energy and Environment-oriented Applications: Electrocatalysis, Photoelectrocatalysis and Photocatalysis*. Royal Society of Chemistry, 2025. ISBN: 978-1-83767-381-0

1. K. K. Bedala, P. Gonugunta, M. Soleimani, **E. Mádai**, P. Taheri, S. K. Padamati, P. Nagaraju, G. Upender, and B. V. Kumar. "Facile synthesis of $ZnIn_2S_4/Cu_2O$ hierarchical heterostructures for enhanced selectivity and sensitivity of NH_3 gas at room temperature". In: *Applied Surface Science* 640 (2023), p. 158315

Published before the PhD:

6. B. Hohl, **E. Mádai**, D. Boda, and M. Valiskó. "Modeling of a pH–tunable dual–response nanopore sensor". In: *Journal of Molecular Liquids* 310 (2020), p. 112946

5. **E. Mádai**, M. Valiskó, and D. Boda. "Application of a bipolar nanopore as a sensor: rectification as an additional device function". In: *Physical Chemistry Chemical Physics* 21.36 (2019), pp. 19772–19784

4. **E. Mádai**, M. Valiskó, and D. Boda. "The effect of the charge pattern on the applicability of a nanopore as a sensor". In: *Journal of Molecular Liquids* 283 (2019), pp. 391–398

3. M. Valiskó, B. Matejczyk, Z. Ható, T. Kristóf, **E. Mádai**, D. Fertig, D. Gillespie, and D. Boda. "Multiscale analysis of the effect of surface charge pattern on a nanopore's rectification and selectivity properties: From all-atom model to Poisson-Nernst-Planck". In: *The Journal of chemical physics* 150.14 (2019)

2. **E. Mádai**, B. Matejczyk, A. Dallos, M. Valiskó, and D. Boda. "Controlling ion transport through nanopores: modeling transistor behavior". In: *Physical Chemistry Chemical Physics* 20.37 (2018), pp. 24156–24167

1. **E. Mádai**, M. Valiskó, A. Dallos, and D. Boda. "Simulation of a model nanopore sensor: Ion competition underlies device behavior". In: *The Journal of Chemical Physics* 147.24 (2017)

No such deceptive dream allureth me:
I know a hundred times I'll baffled be.
I do not care. What, after all's the end?
The end - when glory's o'er - I apprehend.
The end, is death, and life is a constant strife:
The aim of man, to struggle throughout life.

The Tragedy of Man - Imre Madách